Design and Experimental Results for the S805 Airfoil

Dan M. Somers
Airfoils, Incorporated
State College, Pennsylvania

NREL technical monitor: James Tangler

◆NREL

January 1997

NOTICE

This report was prepared as an account of work sponsored by an agency of the United States government. Neither the United States government nor any agency thereof, nor any of their employees, makes any warranty, express or implied, or assumes any legal liability or responsibility for the accuracy, completeness, or usefulness of any information, apparatus, product, or process disclosed, or represents that its use would not infringe privately owned rights. Reference herein to any specific commercial product, process, or service by trade name, trademark, manufacturer, or otherwise does not necessarily constitute or imply its endorsement, recommendation, or favoring by the United States government or any agency thereof. The views and opinions of authors expressed herein do not necessarily state or reflect those of the United States government or any agency thereof.

Available to DOE and DOE contractors from:
        Office of Scientific and Technical Information (OSTI)
        P.O. Box 62
        Oak Ridge, TN 37831
Prices available by calling (423) 576-8401

Available to the public from:
        National Technical Information Service (NTIS)
        U.S. Department of Commerce
        5285 Port Royal Road
   Springfield, VA 22161
        (703) 487-4650

Printed on paper containing at least 50% wastepaper, including 20% postconsumer waste

DISCLAIMER

Portions of this document may be illegible
in electronic image products. Images are
produced from the best available original
document.

Foreword

Validation of the Eppler Airfoil Design and Analysis Code has been a major goal of several NREL-sponsored, two-dimensional investigations in the low-turbulence wind tunnel of the Delft University of Technology Low Speed Laboratory, The Netherlands. Initial validation of the code with respect to wind-turbine airfoils was based on data acquired for a low maximum-lift-coefficient airfoil of a thin-airfoil family. This test was conducted in 1985 upon completion of the design effort for a thin-airfoil family for stall-regulated rotors. The primary airfoil of this family, the 13.5-percent-thick S805, was tested and the results showed that the Eppler Code predicted all the section characteristics well except the profile-drag coefficient. The drag coefficient was underpredicted as a result of underestimating the significance of the laminar separation bubbles, through which the laminar flow transitioned to turbulent flow. As a result of this test, an adjustment to the design methodology that accounted for this bias error was used to modify the S805 airfoil to alleviate the strength of the laminar separation bubbles. The resulting airfoil, the S805A, replaces the S805 airfoil.

The use of the Delft University of Technology low-turbulence wind tunnel was essential to quantify the effect of the laminar separation bubbles on the section characteristics. In most wind tunnels, intense small-scale turbulence generated by the fan suppresses the laminar separation bubbles. This results in optimistic performance measurements relative to those obtained in the free atmosphere. Intense, small-scale turbulence that interacts with the boundary layer on the airfoil is not present in the free atmosphere. Atmospheric turbulence scales are orders of magnitude larger than the turbulence that exists in a wind tunnel. The Delft University of Technology low-turbulence wind tunnel is recognized worldwide as having the lowest (small-scale) turbulence level (less than 0.05 percent) of any commercially available wind tunnel and is thus better able to simulate free-atmosphere conditions.
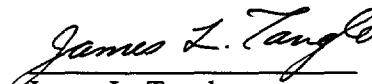
James L. Tangler
Wind Technology Division
National Renewable Energy Laboratory
1617 Cole Blvd.
Golden, Colorado 80401 USA
Internet Address: tanglerj@tcplink.nrel.gov
Phone 303-384-6934
FAX   303-384-6901

Contents

List of Figures

Design and Experimental Results for the S805 Airfoil

Dan M. Somers †

October 1988

Abstract

An airfoil for horizontal-axis wind-turbine applications, the S805, has been designed and analyzed theoretically and verified experimentally in the low-turbulence wind tunnel of the Delft University of Technology Low Speed Laboratory, The Netherlands. The two primary objectives of restrained maximum lift, insensitive to roughness, and low profile drag have been achieved. The airfoil also exhibits a docile stall. Comparisons of the theoretical and experimental results show good agreement. Comparisons with other airfoils illustrate the restrained maximum lift coefficient as well as the lower profile-drag coefficients, thus confirming the achievement of the primary objectives.

Introduction

The majority of the airfoils in use on horizontal-axis wind turbines today were originally developed for airplanes. The design requirements for these airfoils, primarily National Advisory Committee for Aeronautics (NACA) and National Aeronautics and Space Administration (NASA) airfoils (refs. 1–6), are significantly different from those for wind-turbine airfoils. Accordingly, two sets of airfoils were designed, using the method of references 7 and 8, specifically for horizontal-axis wind-turbine applications. (See ref. 9.) The most prominent difference between the two sets is the relatively low ("restrained") maximum lift coefficients specified for the primary and tip airfoils (0.75 and 0.95 blade radial stations, respectively) of the second set.

In conjunction with this effort, the primary airfoil of the second set was selected for experimental verification. In 1985, an investigation was conducted in the low-turbulence wind tunnel of the Delft University of Technology Low Speed Laboratory (ref. 10), The Netherlands, to obtain the basic, low-speed, two-dimensional aerodynamic characteristics of this airfoil. The results have been compared with the predictions from the method of references 7 and 8 and also with data from another low-turbulence wind tunnel for other airfoils.

† President, Airfoils, Incorporated, State College, Pennsylvania

1

Symbols and Abbreviations

Values are given in both SI and U.S. Customary Units. Measurements and calculations were made in SI Units.

C_p pressure coefficient

c airfoil chord, mm

c_d section profile-drag coefficient

c_l section lift coefficient

c_m section pitching-moment coefficient about quarter-chord point

d streamwise distance from model trailing edge to tips of wake-rake total-pressure tubes, mm

DFVLR   Deutsche Forschungs- und Versuchsanstalt für Luft- und Raumfahrt

max   maximum (subscript)

NACA   National Advisory Committee for Aeronautics

R Reynolds number based on free-stream conditions and airfoil chord

T transition (subscript)

V free-stream velocity, m/s

wakerake   wake rake (subscript)

x airfoil abscissa, mm

y span station, mm

z airfoil ordinate, mm

α angle of attack relative to chord line, deg

Airfoil Design

Objectives and Constraints

Two primary objectives are evident from the design specifications for this airfoil (table 1). The first objective was to achieve a maximum lift coefficient that is relatively low (restrained). A requirement related to this objective was that the maximum lift coefficient not decrease with transition fixed near the leading edge on both surfaces. The second objective was to obtain low profile-drag coefficients over the range of lift coefficients from 0.5 to 0.9 for a Reynolds number of 1.0×10^6.

Two major constraints were placed on the design of this airfoil. First, the zero-lift pitching-moment coefficient must be no more negative than −0.05. Second, the airfoil thickness should fall within the specified range.

Philosophy

Given the above objectives and constraints, certain characteristics of the design are evident. The following sketch illustrates the desired polar that meets the goals for this design.
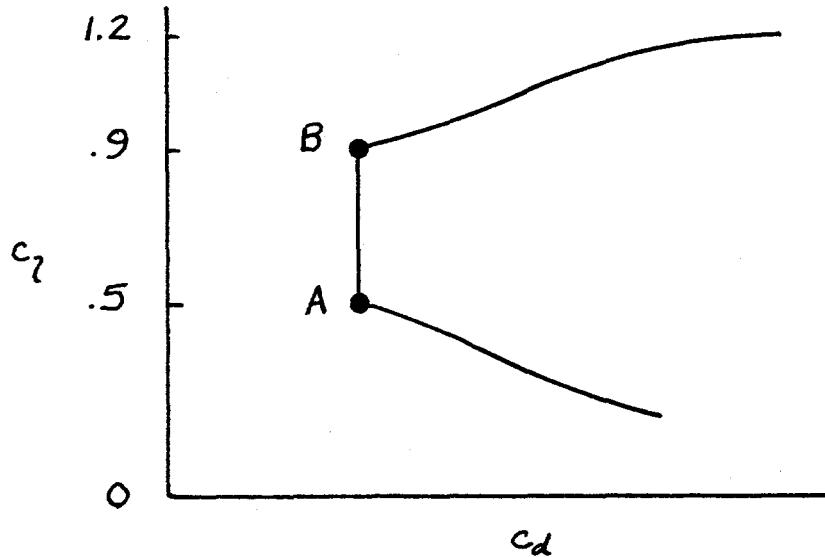

Sketch 1

The desired airfoil shape can be related to the pressure distributions that occur at the various points in the sketch. Point A is the lower limit of the laminar bucket; point B, the upper limit. The values of the drag coefficients at both points are nearly equal and are determined by the extents of laminar flow on the upper and lower surfaces. The drag increases very rapidly outside the laminar bucket because the transition point moves quickly toward the leading edge. This feature results in a rather sharp leading edge that produces a suction peak at the higher lift coefficients. This peak limits the maximum lift coefficient and assures that transition will occur very near the leading edge. Thus, the maximum lift coefficient occurs with turbulent flow along the entire upper surface, and, therefore, the addition of roughness at the leading edge should

have little influence on the boundary-layer development along the upper surface and, accordingly, the maximum lift coefficient.

This outline of the desired section characteristics is not sufficient to design the airfoil, however, primarily because of the inexactly specified airfoil thickness. Accordingly, the thickness was selected to be equal to that of the S801 airfoil (ref. 9), 13.5-percent chord. Because the selected airfoil thickness allows a wider laminar bucket to be achieved than that specified, point A, which occurs at a lift coefficient of 0.5, should not correspond to the lower limit of the bucket but, instead, to a point near the middle of the bucket.

From the preceding discussion, the pressure distributions at points A and B can be deduced. The pressure distribution at point A should look something like this:
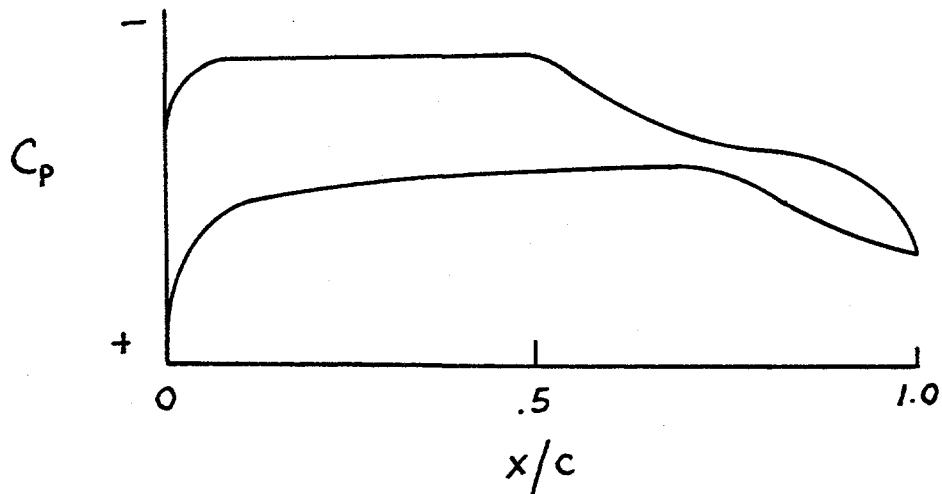

Sketch 2

To achieve low drag, a favorable pressure gradient is desirable along the upper surface to about 0.5c. Aft of this point, a short region of slightly adverse pressure gradient ("transition ramp") is desirable to promote the efficient transition from laminar to turbulent flow. Thus, the initial slope of the pressure recovery is relatively shallow. This short region is followed by a steeper concave pressure recovery that produces lower drag and has less tendency to separate than the corresponding linear or convex pressure recovery (ref. 11).

A slightly favorable pressure gradient is desirable along the lower surface to about 0.65c to achieve low drag. The initial slope of the pressure recovery is very shallow in order to inhibit the formation of significant laminar separation bubbles.

The amounts of pressure recovery on the two surfaces are determined by the pitching-moment constraint and the airfoil thickness.

4

At point B, the pressure distribution should look like this:
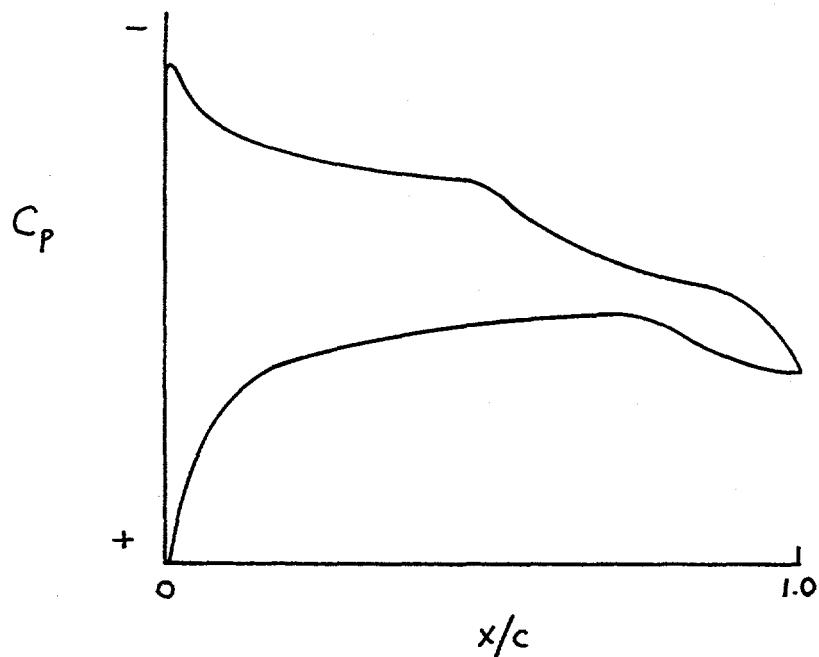
Sketch 3

No suction spike exists at the leading edge. Instead, a rounded peak occurs just aft of the leading edge. This feature is the result of incorporating increasingly favorable pressure gradients toward the leading edge. It is quite important because it allows a wider laminar bucket to be achieved.

Execution

Given the pressure distributions for lift coefficients of 0.5 and 0.9, the design of the airfoil is reduced to the inverse problem of transforming the pressure distributions into an airfoil shape. The Eppler Airfoil Design and Analysis Program (refs. 7 and 8) was used because of confidence gained during the design, analysis, and experimental verification of several other airfoils.

The airfoil is designated the S805. The inviscid pressure distributions computed by the method of references 7 and 8 for lift coefficients of 0.5 and 0.9 are shown in figures 1(a) and 1(b), respectively. The airfoil shape is shown in figure 2 and the coordinates are contained in table 2.

Experimental Procedure

Wind Tunnel

The low-turbulence wind tunnel (ref. 10) of the Delft University of Technology Low Speed Laboratory, The Netherlands, is a closed-throat, single-return, atmospheric tunnel (fig. 3). The turbulence level in the test section varies from 0.02 percent at 10 m/s (33 ft/s) to 0.04 percent at 60 m/s (200 ft/s).

5

The octagonal test section is 180.0 cm (70.87 in.) wide by 125.0 cm (49.21 in.) high. Electrically actuated turntables provide positioning and attachment for the two-dimensional model. The turntables are flush with the top and bottom tunnel walls and rotate with the model. The axis of rotation coincided with the quarter chord of the model which was mounted vertically between the turntables. (See fig. 4.) The gaps between the model and the turntables were sealed.

Model

The aluminum, wind-tunnel model was constructed by the Deutsche Forschungs- und Versuchsanstalt für Luft- und Raumfahrt e.V. (DFVLR), Braunschweig, Federal Republic of Germany. The model had a chord of 500.00 mm (19.685 in.) and a span of 1248 mm (49.13 in.). Chordwise orifices were located in the upper and lower surfaces to one side of the midspan at the staggered positions listed in table 3. Spanwise orifices were located in the upper surface only in order to monitor the two-dimensionality of the flow at high angles of attack. All the orifices were 0.40 mm (0.016 in.) in diameter with their axes perpendicular to the surface. The measured model contour was generally within 0.2 mm (0.008 in.) of the prescribed shape.

Wake Rake

A total-pressure, a static-pressure, and an integrating wake rake were mounted on a strut between the tunnel sidewalls (figs. 4 and 5). The strut could be positioned spanwise and streamwise in the test section. Movement of the strut provided positioning of the wake rakes normal to the sidewalls. The tips of the total-pressure tubes were located 0.632c downstream of the trailing edge of the model for all test runs except those at a Reynolds number of 0.5×10^6 when they were located 0.430c downstream of the trailing edge. The details of the wake rakes are shown in figures 6 and 7. The integrating wake rake was not used in this investigation.

Instrumentation

Measurements of the basic tunnel pressures, the static pressures on the model surfaces, and the wake-rake pressures were made by a multitube manometer which was read automatically using photoelectric cells. Data were obtained and recorded by an electronic data-acquisition system.

Methods

The static-pressure measurements on the model surface were reduced to standard pressure coefficients and numerically integrated to obtain section normal-force coefficients and section pitching-moment coefficients about the quarter-chord point. Section profile-drag coefficients were computed from the wake-rake total and static pressures by the method of reference 12. Standard, low-speed, wind-tunnel boundary corrections (ref. 13) have been applied to the data. The following procedure was used. The uncorrected force, moment, and pressure coefficients were referred to the apparent dynamic pressure as measured tunnel empty at the model position. The lift, profile-drag, pitching-moment, and airfoil pressure coefficients and the angle of attack were then corrected by the method of reference 13. The corrected values were plotted. Finally, as a check, the corrected airfoil pressure distribution was numerically integrated to obtain the corrected normal-force (and pitching-moment) coefficient which, together with the corrected profile-drag coefficient and angle of attack, yields the corrected lift coefficient (and chord-force coefficient).

At high angles of attack, the wake becomes wider than the wake rake. When this occurs, the drag is obtained from a parabolic extrapolation of the measured wake pressures. At even higher angles of attack, the total-pressure coefficients measured in the wake become negative, making calculation of the drag impossible. In these cases, an uncorrected profile-drag coefficient of 0.3 (estimated from ref. 14) is assumed.

An angle-of-attack misalignment of $-0.046°$ has been neglected.

Tests

The model was tested at Reynolds numbers based on airfoil chord from 0.5×10^6 to 2.0×10^6. The model was tested smooth (transition free) and with transition fixed by roughness at 0.02c on the upper surface and 0.05c on the lower surface. The grit roughness was sized by the method of reference 15 and sparsely distributed along 3-mm (0.1-in.) wide strips applied to the model with lacquer. (See table 4.)

Starting from 0°, the angle of attack was increased until the entire upper surface was separated and then decreased to determine hysteresis. The same procedure was followed for the negative angles of attack. For a Reynolds number of 2.0×10^6, the static pressures on the upper surface could not be measured by the manometer at high angles of attack because the differences between those pressures and the free-stream static pressure were too great.

For several test runs, the model surfaces were coated with oil to determine the location, as well as the nature, of the boundary-layer transition from laminar to turbulent flow (ref. 16). Transition was also located using a probe containing a microphone, which was positioned near the leading edge at midspan and then moved slowly downstream along the model surface. The beginning of the turbulent boundary layer was detected as an increase in noise level over that for the laminar boundary layer which was essentially silent. (See ref. 17.) Tufts were used to check the two-dimensionality of the flow, as well as the turbulent-separation pattern, at high angles of attack.

Two turbulators, zigzag tape (ref. 18), were placed on the model, one between 0.48c and 0.50c on the upper surface and the other between 0.65c and 0.67c on the lower surface, to determine their effect on laminar separation bubbles and section characteristics. The details of the 0.25-mm (0.010-in.) thick tape are shown in the following sketch.

Sketch 4

7
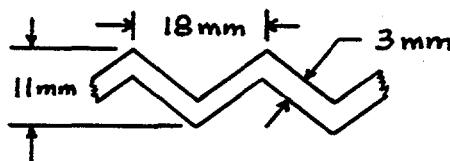
Discussion of Results

Experimental Results

Pressure Distributions

The pressure distributions at various angles of attack for a Reynolds number of 1.0×10^6 are shown in figure 8. The irregularities in the pressure distributions near the leading edge on both the upper and lower surfaces are due to irregularities in the surface curvature of the model at those locations.

At an angle of attack of 1.03° (fig. 8(a)), a laminar separation bubble is evident on the upper surface around midchord and on the lower surface around 0.8c. As the angle of attack is increased, the bubble on the upper surface decreases in length whereas the one on the lower surface increases. At an angle of attack of 5.11° (fig. 8(b)), the bubble on the upper surface is barely discernible. The lift coefficient at this angle of attack corresponds approximately to the upper limit of the laminar bucket. As the angle of attack is increased further, turbulent, trailing-edge separation occurs on the upper surface. The amount of separation increases with increasing angle of attack. At an angle of attack of 13.19° (fig. 8(d)), the laminar separation bubble on the lower surface disappears and laminar flow extends to the trailing edge. At an angle of attack of 14.19° (fig. 8(e)), the maximum lift coefficient occurs. At an angle of attack of 20.06° (fig. 8(d)), the leading-edge pressure peak collapses and the entire upper surface is separated.

As the angle of attack is decreased from 20.06°, the entire upper surface remains separated until the leading-edge pressure peak reforms at an angle of attack of 17.13° (fig. 8(e)). The pressure distribution at this angle of attack is almost identical to the one that occurs with increasing angle of attack (fig. 8(d)). Thus, only a small amount of hysteresis occurs with respect to separation on the upper surface.

As the angle of attack is decreased from 0°, the laminar separation bubble on the lower surface decreases in length until it disappears at an angle of attack of –1.77° (fig. 8(f)). The lift coefficient at this angle of attack corresponds approximately to the lower limit of the laminar bucket. As the angle of attack is decreased further, the pressure coefficients in the concave region of the lower surface decrease because the transition point on the lower surface moves rapidly forward resulting in a thicker turbulent boundary layer downstream (fig. 8(g)). As the angle of attack is decreased even further, the laminar separation bubble on the upper surface increases in length. At an angle of attack of –7.12° (fig. 8(h)), a long laminar separation bubble forms on the lower surface. As the angle of attack is decreased still further, the long bubble on the lower surface increases in length. At an angle of attack of –9.11° (fig. 8(i)), the minimum lift coefficient occurs. At an angle of attack of –13.04° (fig. 8(j)), the long bubble extends over the entire lower surface.

As the angle of attack is increased from –13.04°, the long bubble on the lower surface decreases in length until it disappears at an angle of attack greater than –7.12° (fig. 8(k)). The pressure distributions are identical to those that occur with decreasing angle of attack. Thus, no hysteresis occurs with respect to separation on the lower surface.

Transition Location

Oil-flow photographs of the upper and lower surfaces at various angles of attack for Reynolds numbers of 1.0×10^6 and 2.0×10^6 are shown in figures 9 through 12. Because the model was mounted vertically, the oil flowed under the influence of gravity as well as the airstream. Thus, the oil is seen flowing spanwise in several photographs, particularly at chord locations where the boundary layer is thick, near

separation, or separated. Note also that frequently oil-flow patterns at a number of angles of attack were photographed in succession without redistributing the oil to save time. Thus, patterns from the preceding angles of attack can be seen in the succeeding photographs. These patterns range from essentially undisturbed to significantly altered, depending on the flow at the angle of attack in the subsequent photograph.

For a Reynolds number of 1.0×10^6, the mechanism of the boundary-layer transition from laminar to turbulent flow on the upper surface, at an angle of attack of 0.0°, was a laminar separation bubble (fig. 9(a)). As the angle of attack is increased, the bubble decreases in length (fig. 9(b)). At an angle of attack of 5.1° (fig. 9(c)), the bubble is barely distinguishable. As the angle of attack is increased further, no bubble is evident and the transition location moves forward (figs. 9(d) and 9(e)). At an angle of attack of 12.2° (fig. 9(f)), a very short laminar separation bubble appears at the leading edge. The line of oil near two-thirds chord is a remnant of the previous angle of attack (not shown).

For a Reynolds number of 2.0×10^6, the mechanism of transition on the upper surface, at an angle of attack of 0.0°, was again a laminar separation bubble (fig. 10(a)). The bubble for this Reynolds number is, however, shorter in length than the corresponding bubble for a Reynolds number of 1.0×10^6 (fig. 9(a)). As the angle of attack is increased, the bubble decreases in length and has disappeared at an angle of attack of 4.1° (fig. 10(b)). As the angle of attack is increased further, the transition location moves forward (figs. 10(c) and 10(d)). At any given angle of attack, transition occurs further forward for the higher Reynolds number.

For a Reynolds number of 1.0×10^6, the mechanism of transition on the lower surface, at an angle of attack of 0.0°, was a laminar separation bubble (fig. 11(a)). The bubble on the lower surface is generally longer than the one on the upper surface. As the angle of attack is increased, the bubble increases in length (fig. 11(b)). As the angle of attack is decreased from 0°, the bubble decreases in length (fig. 11(c)). At an angle of attack of –3.0° (fig. 11(d)), no bubble is evident and transition occurs near the leading edge.

For a Reynolds number of 2.0×10^6, the mechanism of transition on the lower surface, at an angle of attack of 0.0°, was again a laminar separation bubble (fig. 12). The bubble for this Reynolds number is, however, shorter in length than the corresponding bubble for a Reynolds number of 1.0×10^6 (fig. 11(a)).

The variation of transition location with angle of attack, as determined by microphone measurements, is shown in figure 13. It should be remembered that only attached turbulent flow can be detected using this technique. Thus, for an angle of attack at which a laminar separation bubble is present, the transition location measured corresponds to the turbulent-reattachment point. The symbols represent conditions where the onset of turbulence was sudden. These conditions occur at the turbulent-reattachment point or where natural transition occurs rapidly. The bars represent conditions where natural transition occurs over some length. The bars extend from the beginning of transition (defined here as the point where turbulent bursts are first detected) to the end of transition (defined here as the point where individual bursts can no longer be distinguished). It should be noted that wind-tunnel boundary corrections have not been applied to the angle of attack shown in figure 13 only.

Section Characteristics

Spanwise drag measurements.- The variation of profile-drag coefficient with span station at four angles of attack is shown for a Reynolds number of 1.0×10^6 in figure 14. The four angles of attack, –1.5°, 0.0°, 2.1°, and 5.1°, correspond approximately to the lower limit, the lower middle, the upper middle, and the upper limit of the laminar bucket, respectively, for this Reynolds number. The greatest drag variation

occurs in the vicinity of the station that corresponds to the chordwise pressure orifices in the model. A total-pressure wake-rake position of 31.2 cm, which coincides with the tunnel centerline, was selected for all succeeding drag measurements because it resulted in a drag coefficient representative of the mean value at each of the four angles of attack.

Reynolds number effects.- The section characteristics are shown in figure 15. The effects of Reynolds number on the section characteristics are summarized in figure 16.

For the design Reynolds number ($R = 1.0 \times 10^6$) (fig. 15(c)), the maximum lift coefficient was approximately 1.18, which is essentially equal to the design objective of 1.2. The trailing-edge stall was very docile. A small amount of hysteresis occurred at angles of attack greater than that for maximum lift; none occurred at angles of attack less than that for minimum lift. Low drag coefficients were obtained over the range of lift coefficients from about 0.06 to 0.84. Thus, the lower limit of the laminar bucket is well below that specified (0.5) and the upper limit is slightly below that specified (0.9). The curved shape of the polar (higher drag between the limits than at them) indicates that the laminar separation bubbles, shown in figures 8, 9, and 11, adversely affected the drag. The zero-lift pitching-moment coefficient was approximately –0.048, which satisfies the design constraint ($\geq$ –0.05).

Effect of roughness.- The effect of roughness on the section characteristics for various Reynolds numbers is shown in figure 17. The angle of attack for zero lift coefficient as well as the pitching-moment coefficients generally increased with transition fixed, whereas the lift-curve slope decreased. All these results are partly a consequence of the boundary-layer-displacement effect that decambers the airfoil slightly, the displacement thickness being greater for the transition-fixed condition than for the transition-free condition. Increasing Reynolds number decreases the displacement thickness and, therefore, the displacement effect. In addition, the lift-curve slopes and magnitude of the pitching-moment coefficients are probably too low with transition fixed. For most conditions, the Reynolds number, based on local conditions and boundary-layer momentum thickness, at the roughness location is too low to support turbulent flow. Accordingly, in order to force transition, the roughness must increase the momentum thickness, which increases the extent of the turbulent, trailing-edge separation on the upper surface and, therefore, reduces the magnitudes of the lift and pitching-moment coefficients.

The angle of attack for zero lift coefficient did not increase with transition fixed for the Reynolds numbers of 0.5×10^6 and 1.0×10^6 (figs. 17(a) and 17(c)). For these Reynolds numbers, the roughness was too small to force transition on the upper surface at low lift coefficients. Thus, the laminar separation bubble on the upper surface was not eliminated, whereas the one on the lower surface was, resulting in an increase in lift coefficient compared to the transition-free condition.

Of more importance, however, is the effect of roughness on the maximum lift coefficient and on the drag coefficients. The addition of roughness had no major effect on the maximum lift coefficient for any of the Reynolds numbers. The minor reductions in maximum lift coefficient with transition fixed are probably due to the abnormal roughness effect noted previously. Thus, one of the most important design requirements has been achieved. The drag coefficients were, of course, adversely affected by the roughness. It should be noted, however, that the drag coefficients with transition fixed are probably too high because the height of the roughness was greater than the boundary-layer thickness for most conditions and, therefore, the drag coefficients contain an additional (pressure-drag) contribution due to the roughness itself.

Effect of turbulators.- The effect of turbulators on the section characteristics for a Reynolds number of 1.0×10^6 is shown in figure 18. The turbulators, which eliminated the laminar separation bubbles on the upper and lower surfaces, had no major effect on any of the characteristics except the drag coefficients.

The elimination of the upper-surface bubble altered the pressure distribution in such a way that the lift was decreased and the pitching moment, increased. These effects were counterbalanced by the elimination of the lower-surface bubble, which increased the lift and decreased the pitching moment. Thus, the elimination of the bubbles changed the lift and pitching-moment coefficients little but modified the boundary-layer developments substantially. The influence on the lower-surface drag was larger than on the upper-surface drag. Thus, a significant drag reduction over the entire width of the laminar bucket was produced by the lower-surface turbulator, whereas a smaller drag reduction was produced by the upper-surface turbulator.

Comparison of Theoretical and Experimental Results

Pressure Distributions

The comparison of theoretical and experimental pressure distributions is shown in figure 19. The pressure distributions predicted by the method of references 7 and 8 are inviscid and incompressible. The experimental pressure distributions were obtained for a Reynolds number of 1.0×10^6 and, thus, contain the same data presented in figures 8(a), 8(b), and 8(e). At an angle of attack of 1.03° (fig. 19(a)), the theoretical predictions and the experimental data are in close agreement except in those regions where laminar separation bubbles are present. These bubbles are not modeled in the method of references 7 and 8. Outside these regions, the pressure gradients agree well, although the values of the pressure coefficients do not match exactly. At an angle of attack of 5.11° (fig. 19(b)), the decambering viscous effects have become more apparent and the disparities include small differences in the pressure gradients as well as larger differences in the values of the pressure coefficients. At an angle of attack of 14.19° (fig. 19(c)), which corresponds to the experimental maximum lift coefficient, the agreement is poor primarily because of the upper-surface, trailing-edge separation which is not modeled in the pressure distributions predicted by the method of references 7 and 8.

Section Characteristics

The comparison of theoretical and experimental section characteristics with transition free is shown in figure 20. The drag coefficients are underpredicted by the method of references 7 and 8 for the lower Reynolds numbers. It should be noted, however, that significant laminar separation bubbles are predicted by the method for the Reynolds numbers of 0.5×10^6 and 0.7×10^6 (figs. 20(a) and 20(b)). The abnormal growth of the boundary layer that occurs within the laminar separation bubble is not accurately predicted by the method and, therefore, the drag coefficient is underpredicted. The affected drag coefficients are identified in figure 20 by triangles. As the Reynolds number is increased, the laminar separation bubbles decrease in length and the agreement between the theoretical and experimental drag coefficients improves. The width of the laminar bucket is overpredicted, at least partially because of the irregularities in the surface curvature of the model near the leading edge on both the upper and lower surfaces as evidenced in the pressure distributions. (See fig. 8.) The magnitudes of the angle of attack for zero lift coefficient and the zero-lift pitching-moment coefficient are overpredicted for the Reynolds numbers of 0.5×10^6 and 0.7×10^6 (figs. 20(a) and 20(b)). For these Reynolds numbers, the laminar separation bubble on the upper surface greatly distorts the pressure distribution and, therefore, the lift and pitching-moment coefficients. Again, as the Reynolds number is increased and the laminar separation bubble decreases in length, the agreement between theory and experiment becomes very good (figs. 20(c)–20(e)). The agreement between the theoretical and experimental lift-curve slopes is excellent. The maximum lift coefficients are slightly overpredicted. The magnitude of the pitching-moment

coefficients is generally overpredicted because the boundary-layer-displacement-iteration option of the theoretical method was not used.

The comparison of theoretical and experimental section characteristics with transition fixed is shown in figure 21. The agreement between the theoretical and experimental drag coefficients at low lift coefficients for the Reynolds numbers of 0.5×10^6 and 1.0×10^6 (figs. 21(a) and 21(c)) is poor because the roughness was too small to force transition on the upper surface. The excellent agreement at low lift coefficients for the Reynolds numbers of 0.7×10^6, 1.5×10^6, and 2.0×10^6 (figs. 21(b), 21(d), and 21(e)) is fortuitous because the experimental drag coefficients are probably too high, as previously discussed. The magnitudes of the angle of attack for zero lift coefficient and the zero-lift pitching-moment coefficient are overpredicted for the Reynolds numbers of 0.7×10^6, 1.5×10^6, and 2.0×10^6 (figs. 21(b), 21(d), and 21(e)) because the boundary-layer-displacement-iteration option of the theoretical method was not used. These values are not overpredicted for the Reynolds numbers of 0.5×10^6 and 1.0×10^6 (figs. 21(a) and 21(c)) because transition was not forced on the upper surface at low lift coefficients for these Reynolds numbers and, therefore, the major decambering displacement effect did not occur. Also, the upper-surface laminar separation bubble was not eliminated and, accordingly, the magnitudes of the experimental lift and pitching-moment coefficients are too high. The drag coefficients appear to be underpredicted at higher lift coefficients for all the Reynolds numbers because the experimental lift coefficients are probably too low due to the abnormal roughness effect noted previously. It should also be remembered that the experimental drag coefficients probably contain an additional (pressure-drag) contribution due to the roughness itself. The experimental lift-curve slopes, maximum lift coefficients, and magnitude of the pitching-moment coefficients are probably similarly too low. The magnitude of the pitching-moment coefficients is also overpredicted because the displacement-iteration option was not used.

Comparisons with Other Airfoils

The comparison of the section characteristics of the S805 airfoil and the NACA 4412 and 4415 airfoils (ref. 19) with transition free for the design Reynolds number ($R = 1.0 \times 10^6$) is shown in figure 22. The S805 airfoil generally exhibits a lower maximum lift coefficient (restrained), wider laminar bucket, lower drag coefficients, and less negative pitching-moment coefficients than do the NACA 44-series airfoils. The comparison of the section characteristics of the S805 airfoil and the NACA 23012 and 23015 airfoils (ref. 19) with transition free for the design Reynolds number is shown in figure 23. The S805 airfoil generally exhibits a lower maximum lift coefficient (restrained), softer stall, wider laminar bucket, lower drag coefficients, and more negative pitching-moment coefficients than do the NACA 230-series airfoils.

The comparison of the maximum lift coefficients of all five airfoils for various Reynolds numbers is shown in figure 24. The drag coefficients of these airfoils at a lift coefficient of 0.7 are compared in figure 25. The drag coefficients of the NACA 44-series airfoils are lower than that of the S805 airfoil for $R = 0.7 \times 10^6$. For $R = 1.0 \times 10^6$, the drag coefficients are equal and, as the Reynolds number increases, the drag coefficient of the S805 airfoil becomes increasingly lower than those of the NACA 44-series airfoils. This result is obtained because of the previously-mentioned, adverse effect of the laminar separation bubbles on the drag coefficients of the S805 airfoil, which decreases with increasing Reynolds number. All these comparisons confirm the achievement of the design objectives.

Concluding Remarks

An airfoil for horizontal-axis wind-turbine applications, the S805, has been designed and analyzed theoretically and verified experimentally in the low-turbulence wind tunnel of the Delft University of

Technology Low Speed Laboratory, The Netherlands. The two primary objectives of restrained maximum lift, insensitive to roughness, and low profile drag have been achieved. In addition, the airfoil exhibits a docile stall. Comparisons of the theoretical and experimental results show good agreement. Comparisons with other airfoils clearly illustrate the restrained maximum lift coefficient as well as the lower profile-drag coefficients, thus confirming the achievement of the primary objectives.

Acknowledgments

References

1. Jacobs, Eastman N.; Ward, Kenneth E.; and Pinkerton, Robert M.: The Characteristics of 78 Related Airfoil Sections from Tests in the Variable-Density Wind Tunnel. NACA Rep. 460, 1933.

2. Jacobs, Eastman N.; and Pinkerton, Robert M.: Tests in the Variable-Density Wind Tunnel of Related Airfoils Having the Maximum Camber Unusually far Forward. NACA Rep. 537, 1935.

3. Jacobs, Eastman N.; Pinkerton, Robert M.; and Greenberg, Harry: Tests of Related Forward-Camber Airfoils in the Variable-Density Wind Tunnel. NACA Rep. 610, 1937.

4. Abbott, Ira H.; Von Doenhoff, Albert E.; and Stivers, Louis S., Jr.: Summary of Airfoil Data. NACA Rep. 824, 1945. (Supersedes NACA WR L-560.)

5. Abbott, Ira H.; and Von Doenhoff, Albert E.: Theory of Wing Sections. Dover Publ., Inc., c.1959.

6. McGhee, Robert J.; Beasley, William D.; and Whitcomb, Richard T.: NASA Low- and Medium-Speed Airfoil Development. NASA TM-78709, 1979.

7. Eppler, Richard; and Somers, Dan M.: A Computer Program for the Design and Analysis of Low-Speed Airfoils. NASA TM-80210, 1980.

8. Eppler, Richard; and Somers, Dan M.: Supplement To: A Computer Program for the Design and Analysis of Low-Speed Airfoils. NASA TM-81862, 1980.

9. Somers, Dan M.: The S801 through S808 Airfoils. Airfoils, Inc., 1987. [Proprietary to NREL]

10. van Ingen, J. L.; Boermans, L. M. M.; and Blom, J. J. H.: Low-Speed Airfoil Section Research at Delft University of Technology. ICAS-80-10.1, Munich, Oct. 1980.

11. Wortmann, F. X.: Experimental Investigations on New Laminar Profiles for Gliders and Helicopters. TIL/T.4906, British Minist. Aviat., Mar. 1960. (Translated from Z. Flugwissenschaften, Bd. 5, Heft 8, Aug. 1957, S. 228-243.)

12. The Cambridge University Aeronautics Laboratory: The Measurement of Profile Drag by the Pitot-Traverse Method. R. & M. No. 1688, British A.R.C., 1937.

13. Allen, H. Julian; and Vincenti, Walter G.: Wall Interference in a Two-Dimensional-Flow Wind Tunnel, With Consideration of the Effect of Compressibility. NACA Rep. 782, 1944. (Supersedes NACA WR A-63.)

14. Hoerner, Sighard F.: Fluid-Dynamic Drag. Published by the author (Midland Park, New Jersey), 1965.

15. Braslow, Albert L.; and Knox, Eugene C.: Simplified Method for Determination of Critical Height of Distributed Roughness Particles for Boundary-Layer Transition at Mach Numbers From 0 to 5. NACA TN 4363, 1958.

16. Loving, Donald L.; and Katzoff, S.: The Fluorescent-Oil Film Method and Other Techniques for Boundary-Layer Flow Visualization. NASA MEMO 3-17-59L, 1959.

17. Pfenninger, Werner: Investigations on Reductions of Friction on Wings, in Particular by Means of Boundary Layer Suction. NACA TM 1181, 1947.

18. van Ingen, J. L.; and Boermans, L. M. M.: Research on Laminar Separation Bubbles at Delft University of Technology in Relation to Low Reynolds Number Airfoil Aerodynamics. Proceedings of the Conference on Low Reynolds Number Airfoil Aerodynamics, UNDAS-CP-77B123, Univ. of Notre Dame, June 1985, pp. 89–124.

19. Loftin, Laurence K., Jr.; and Smith, Hamilton A.: Aerodynamic Characteristics of 15 NACA Airfoil Sections at Seven Reynolds Numbers from 0.7×10^6 to 9.0×10^6. NACA TN 1945, 1949.

Table 1. Airfoil Design Specifications

Minimum lift coefficient	—
Maximum lift coefficient	1.2–1.4
"Design" lift coefficient	0.7
Lower limit of laminar bucket	0.5
Upper limit of laminar bucket	0.9
Zero-lift pitching-moment coefficient	≥ -0.05
Reynolds number	1.0×10^6
Thickness	0.12–0.15c

Table 2. S805 Airfoil Coordinates

Upper Surface		Lower Surface	
x/c	z/c	x/c	z/c
0.00270	0.00733	0.00000	−0.00017
.00990	.01572	.00297	−.00614
.02171	.02442	.01222	−.01126
.03807	.03324	.02709	−.01610
.05881	.04194	.04741	−.02056
.08375	.05034	.07289	−.02472
.11264	.05830	.10317	−.02859
.14520	.06567	.13783	−.03215
.18106	.07233	.17642	−.03537
.21985	.07814	.21848	−.03821
.26114	.08298	.26348	−.04061
.30449	.08671	.31089	−.04251
.34943	.08921	.36019	−.04387
.39546	.09034	.41082	−.04464
.44206	.08993	.46221	−.04478
.48868	.08752	.51378	−.04427
.53555	.08243	.56495	−.04305
.58348	.07514	.61515	−.04109
.63223	.06698	.66379	−.03823
.68075	.05869	.71050	−.03427
.72813	.05057	.75510	−.02913
.77354	.04283	.79762	−.02282
.81621	.03557	.83830	−.01599
.85544	.02882	.87666	−.00978
.89061	.02253	.91159	−.00492
.92134	.01649	.94199	−.00164
.94764	.01078	.96683	.00005
.96934	.00590	.98516	.00046
.98588	.00240	.99629	.00020
.99638	.00053	1.00000	.00000
1.00000	.00000		

c = 500.00 mm (19.685 in.)

15

Table 3. Model Orifice Locations

Upper Surface			Lower Surface		
x/c	x, mm	y, mm	x/c	x, mm	y, mm
0.000	0.0	200.0	0.002	1.0	170.0
.002	1.0	195.0	.004	2.0	165.0
.004	2.0	190.0	.008	4.0	160.0
.008	4.0	185.0	.012	6.0	155.0
.012	6.0	180.0	.016	8.0	200.0
.016	8.0	175.0	.020	10.0	195.0
.020	10.0	170.0	.024	12.0	190.0
.024	12.0	165.0	.028	14.0	185.0
.028	14.0	160.0	.032	16.0	180.0
.032	16.0	155.0	.040	20.0	175.0
.040	20.0	200.0	.048	24.0	170.0
.048	24.0	195.0	.064	32.0	165.0
.064	32.0	190.0	.100	50.0	160.0
.100	50.0	185.0	.150	75.0	155.0
.150	75.0	180.0	.200	100.0	200.0
.200	100.0	175.0	.250	125.0	195.0
.250	125.0	170.0	.300	150.0	190.0
.300	150.0	165.0	.350	175.0	185.0
.350	175.0	160.0	.400	200.0	180.0
.400	200.0	155.0	.450	225.0	175.0
.450	225.0	200.0	.500	250.0	200.0
.460	230.0	195.0	.550	275.0	175.0
.470	235.0	190.0	.600	300.0	200.0
.480	240.0	185.0	.650	325.0	195.0
.490	245.0	180.0	.700	350.0	190.0
.500	250.0	175.0	.710	355.0	185.0
.510	255.0	170.0	.720	360.0	180.0
.520	260.0	165.0	.730	365.0	175.0
.530	265.0	160.0	.740	370.0	170.0
.540	270.0	155.0	.750	375.0	165.0
.550	275.0	200.0	.760	380.0	160.0

Table 3. Model Orifice Locations (Concluded)

Upper Surface			Lower Surface		
x/c	x, mm	y, mm	x/c	x, mm	y, mm
.560	280.0	195.0	.770	385.0	155.0
.570	285.0	190.0	.780	390.0	200.0
.580	290.0	185.0	.790	395.0	195.0
.590	295.0	180.0	.800	400.0	190.0
.600	300.0	175.0	.810	405.0	185.0
.650	325.0	170.0	.820	410.0	180.0
.700	350.0	165.0	.830	415.0	175.0
.750	375.0	190.0	.840	420.0	170.0
.800	400.0	165.0	.850	425.0	165.0
.850	425.0	190.0	.860	430.0	160.0
.880	440.0	175.0	.870	435.0	155.0
.900	450.0	165.0	.880	440.0	200.0
.920	460.0	160.0	.890	445.0	195.0
.940	470.0	155.0	.900	450.0	190.0
.960	480.0	200.0	.920	460.0	185.0
.980	490.0	195.0	.940	470.0	180.0
1.000	500.0	190.0	.960	480.0	175.0
			.980	490.0	170.0

c = 500.00 mm (19.685 in.)

Table 4. Roughness Size and Location

Reynolds	Upper Surface			Lower Surface		
	Grit Number	Nominal Size, mm/in.	x/c	Grit Number	Nominal Size, mm/in.	x/c
0.5×10^6	36	0.589/0.0232	0.02	36	0.589/0.0232	0.05
0.7×10^6	36	.589/.0232	.02	36	.589/.0232	.05
1.0×10^6	80/90	.194/.0077	.02	46/54	.385/.0152	.05
1.5×10^6	60	.297/.0117	.02	46/54	.385/.0152	.05
2.0×10^6	60	.297/.0117	.02	46/54	.385/.0152	.05
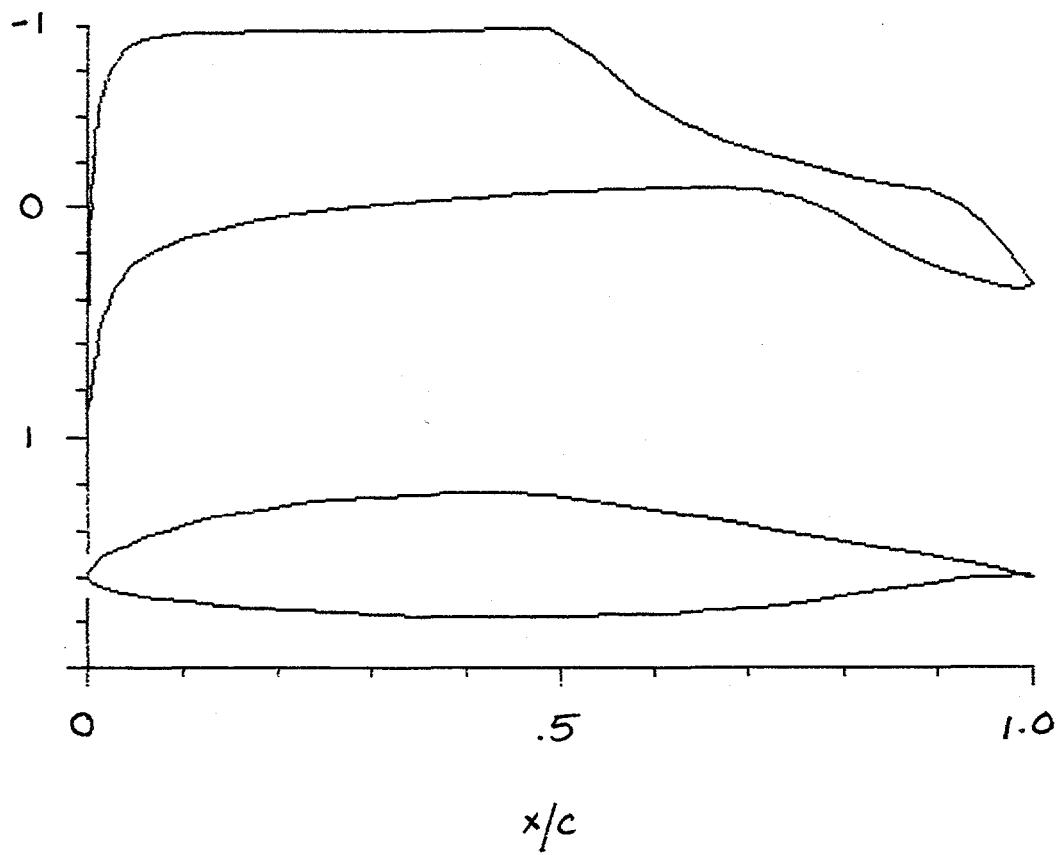
(a) $c_{\ell} = 0.5$.

Figure 1.- Inviscid pressure distributions.
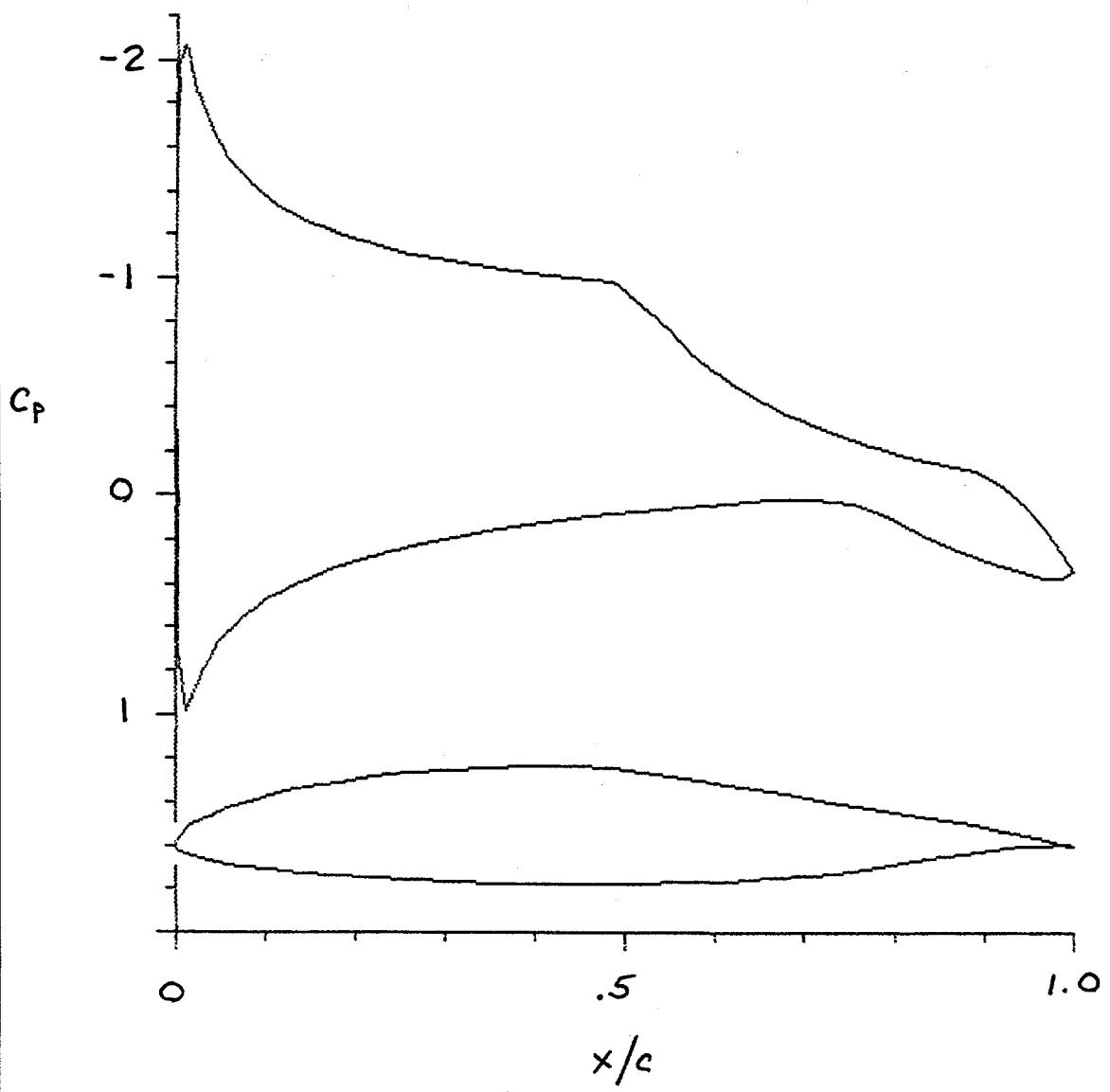
(b) $c_l = 0.9$.

Figure 1.- Concluded.
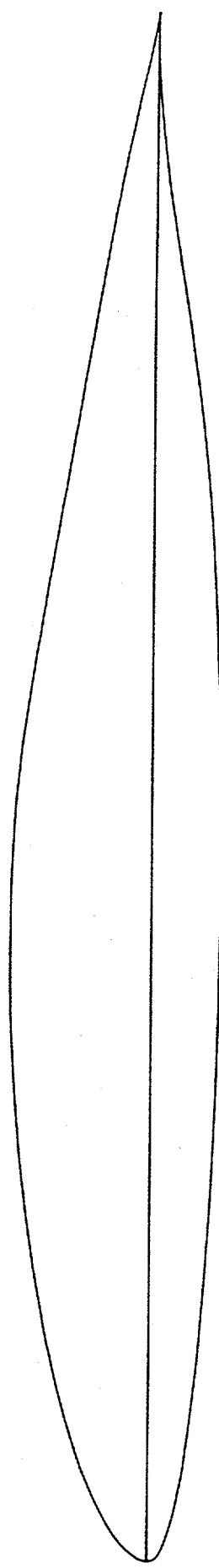
Figure 2.- S805 airfoil shape.

21

1 Schroefaggregaat — Fan and straighteners
2 Aandrijfmotor — Motor
3 Hoekschoepen — Corner vanes
4 Suskamer — Settling chamber
5 Expansiegaas — Diffusing screen
6 Anti_turbulentiegazen — Turbulence screens
7 Gazenbergplaats — Screen storeroom
8 Instroomtuit — Contraction
9 Verwisselbare meetplaats — Exchangeable test section
10 Diffusor — Diffuser
11 Vanggaas — Security screen
12 Spinneweb — Spider web
13 Gaas — Screen
14 Krachtenmeetsysteem — 6 comp. balance

Figure 3.- Delft University of Technology 1.80- x 1.25-m low-speed wind tunnel.

22
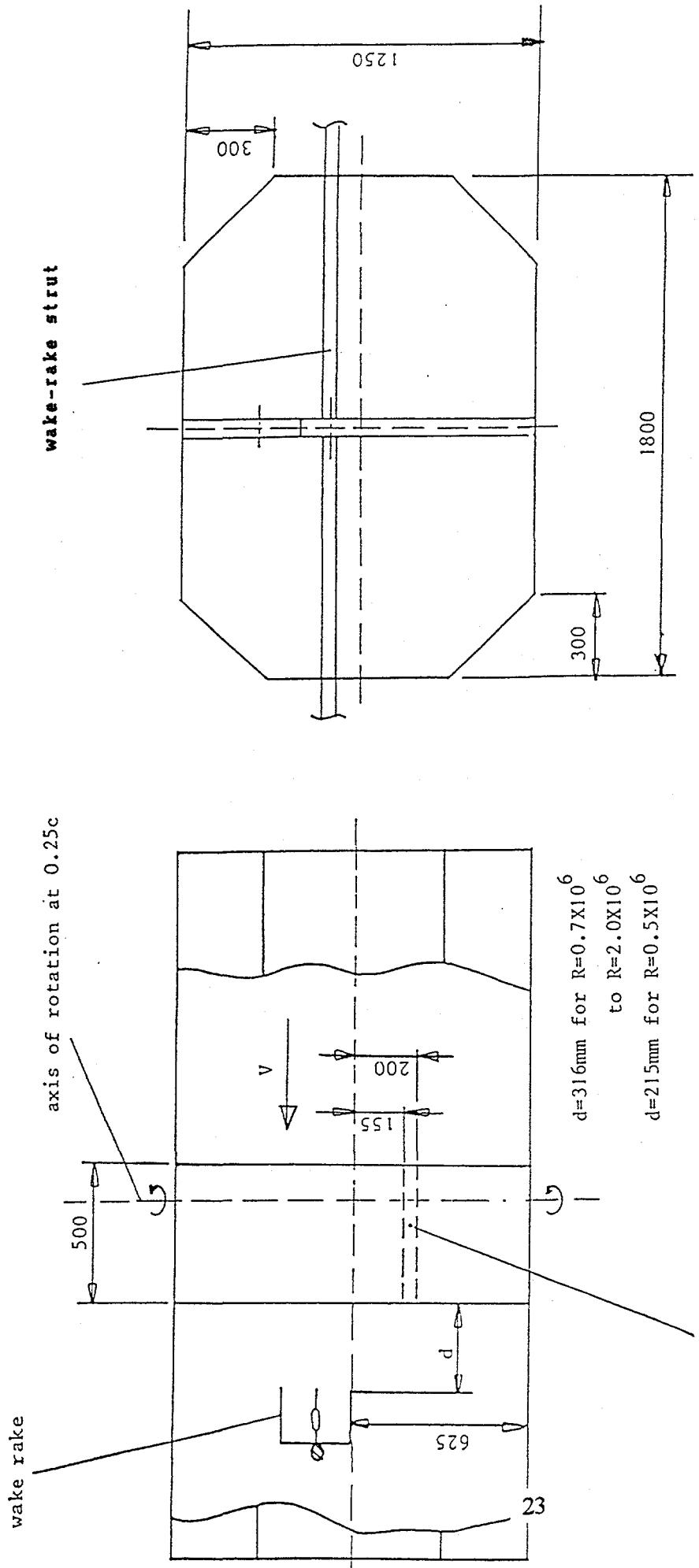
Figure 4.- Model and wake rakes mounted in test section. All dimensions are in mm.
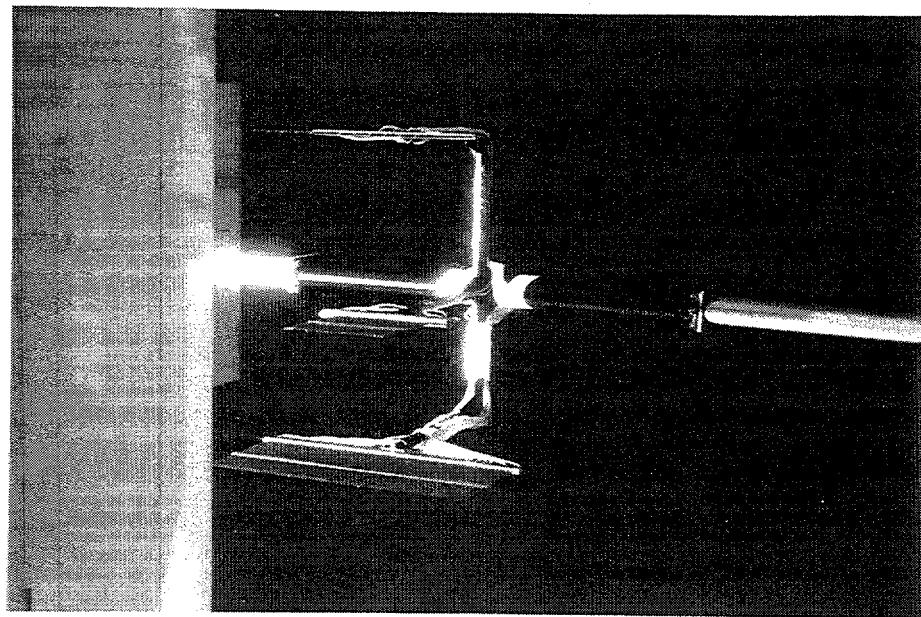
Figure 5.- Photograph of wake rakes mounted on strut.

51 mm

12 tubes spacing 12 mm

Static-pressure wakerake

142 mm

Integrating
wakerake

79.5 mm

24 tubes spacing 3 mm

A. Spacing 6 mm

B. Spacing 12 mm

112 mm

219 mm

B   A   36 tubes spacing 3 mm   A   B

Not connected
pressure tubes

Total-pressure wakerake
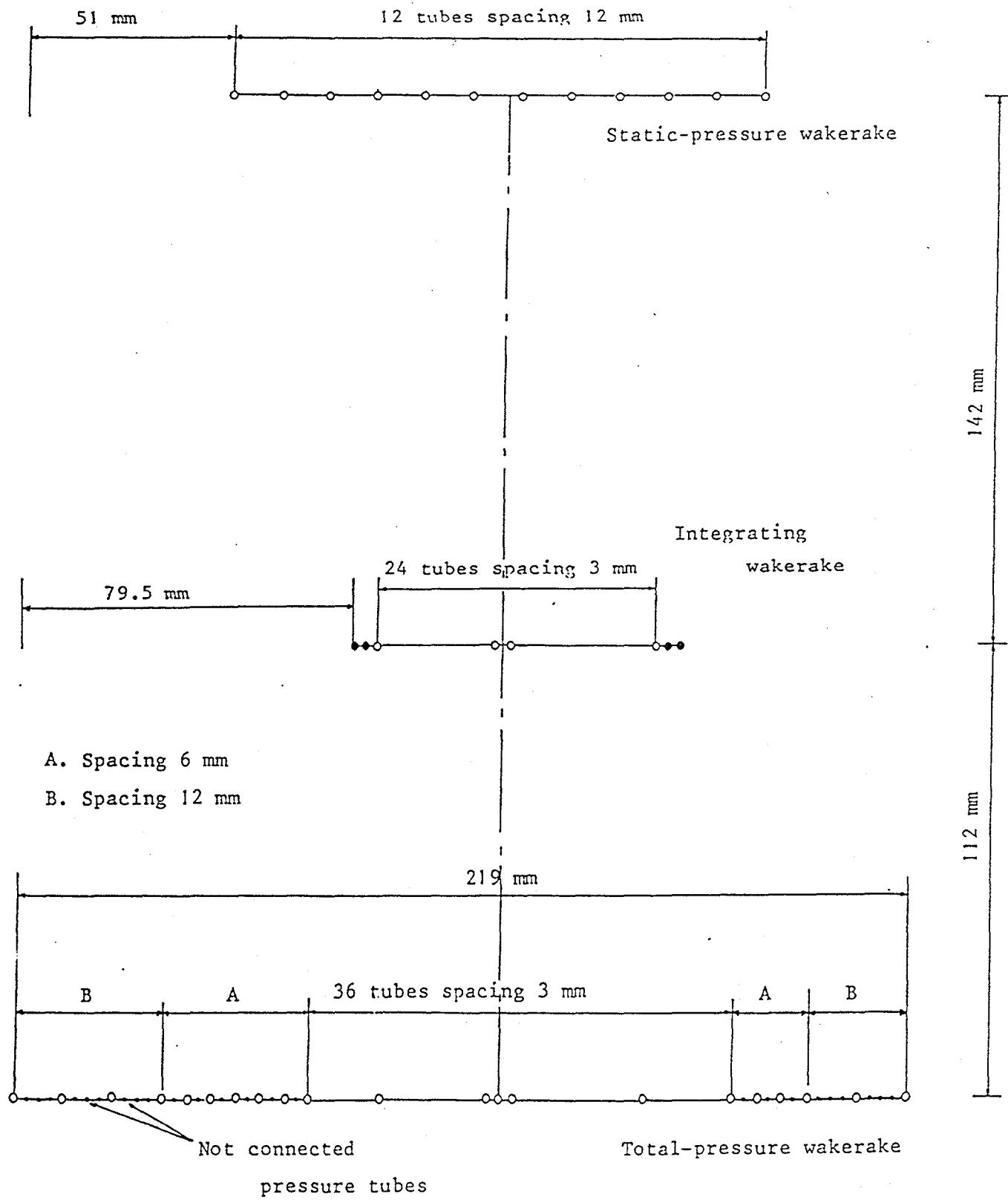
Figure 6.- Wake rakes.

25
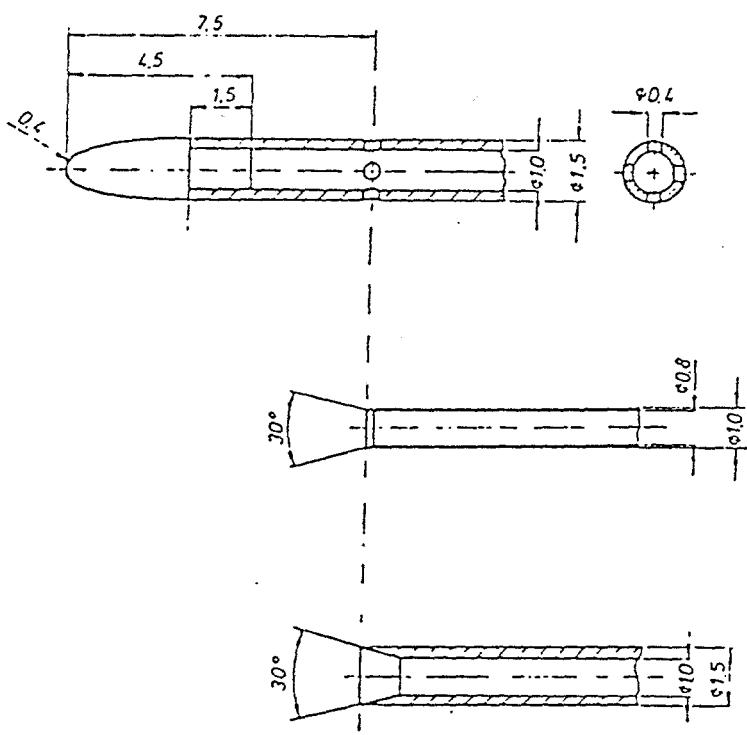
Figure 7.- Static-pressure, integrating, and total-pressure wake-rake tubes. All dimensions are in mm.
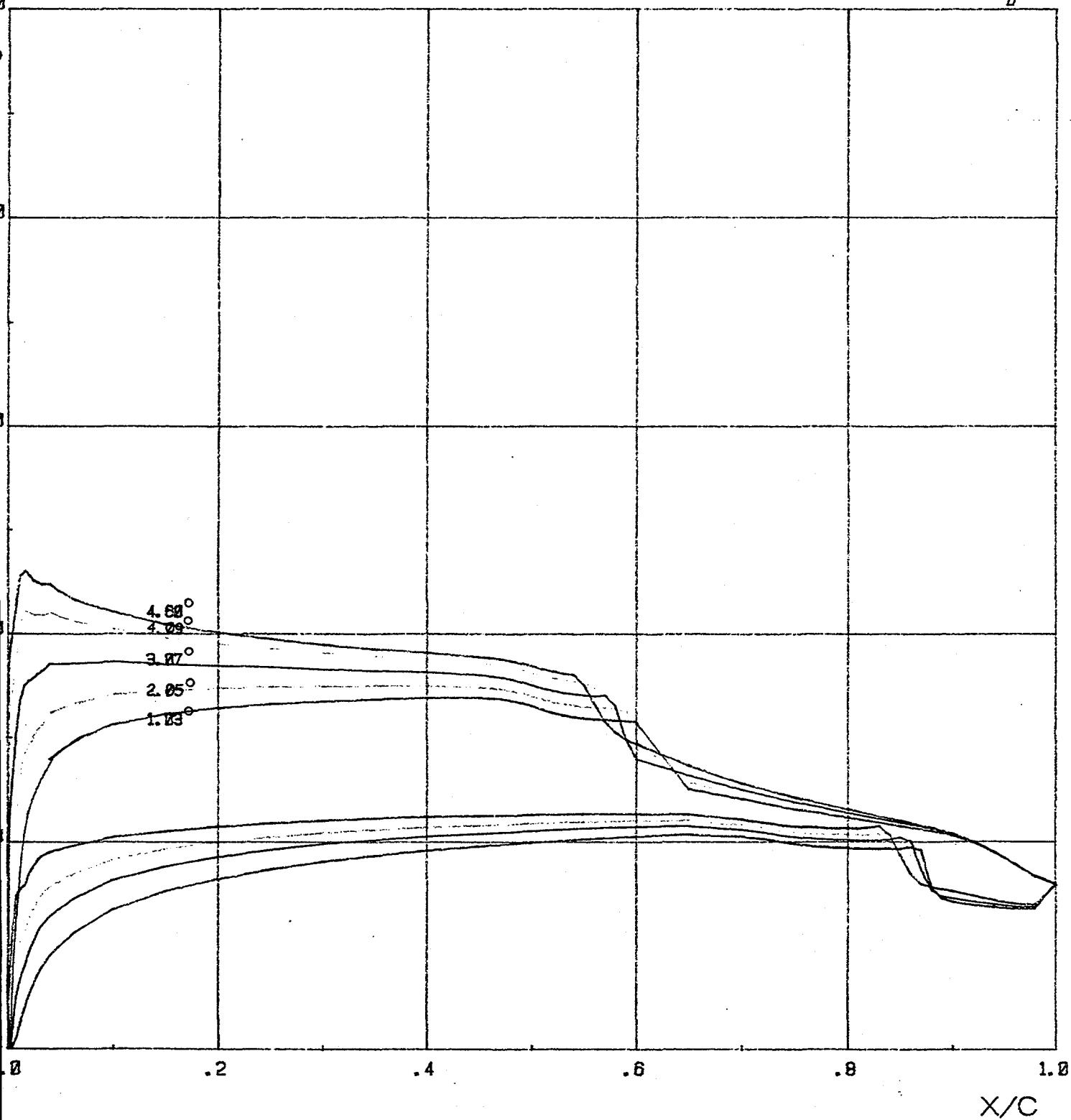
(a) α = 1.03, 2.05, 3.07, 4.09, and 4.60 degrees.

Figure 8.- Pressure distributions for R = 1,000,000. Arrows indicate direction   27
         of angle-of-attack change (for determination of hysteresis).
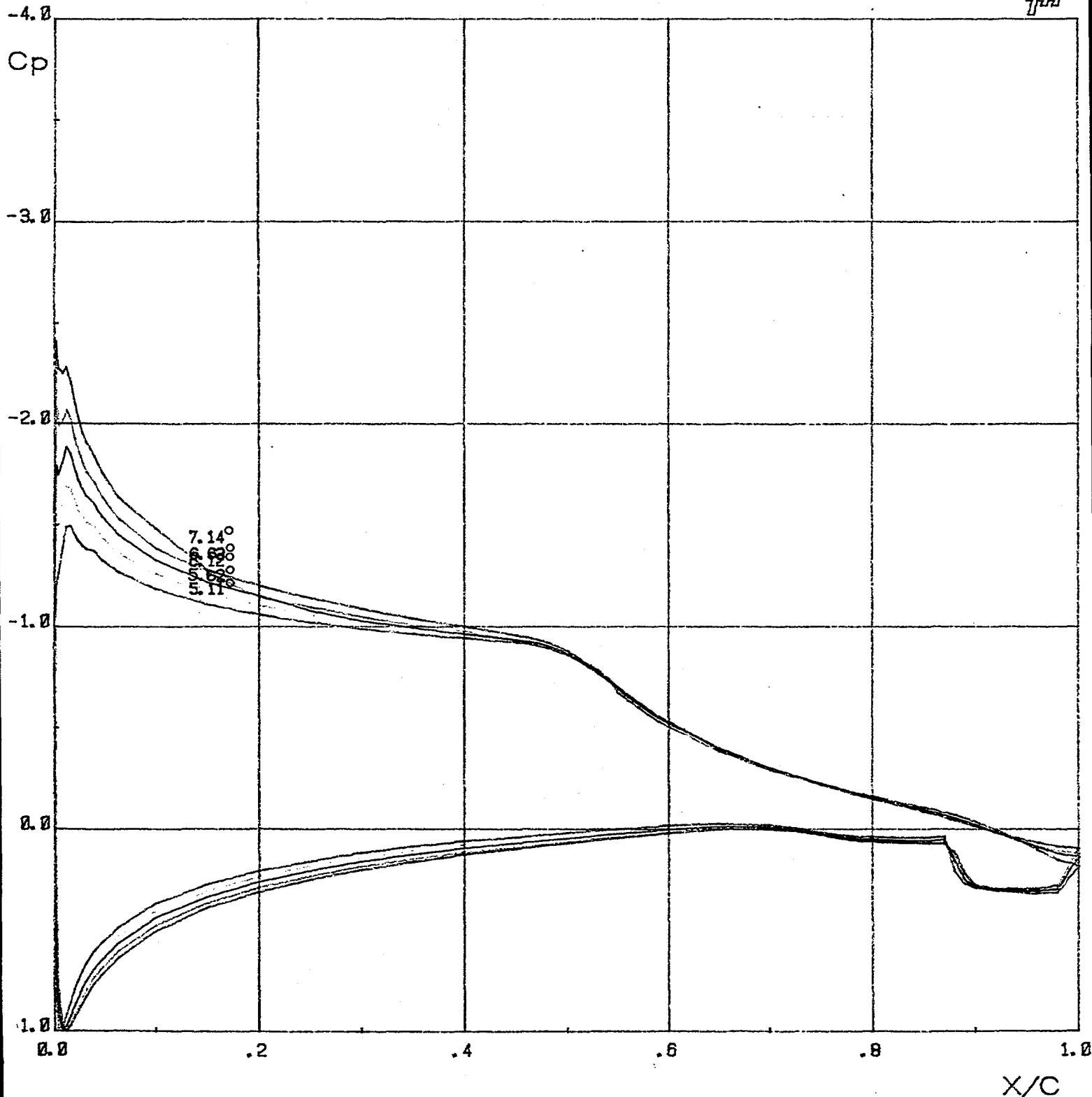
(b) α = 5.11, 5.62, 6.12, 6.63, and 7.14 degrees.

Figure 8.- Continued.

12.2°
11.20
10.2°
9.17°
8.18

X/C
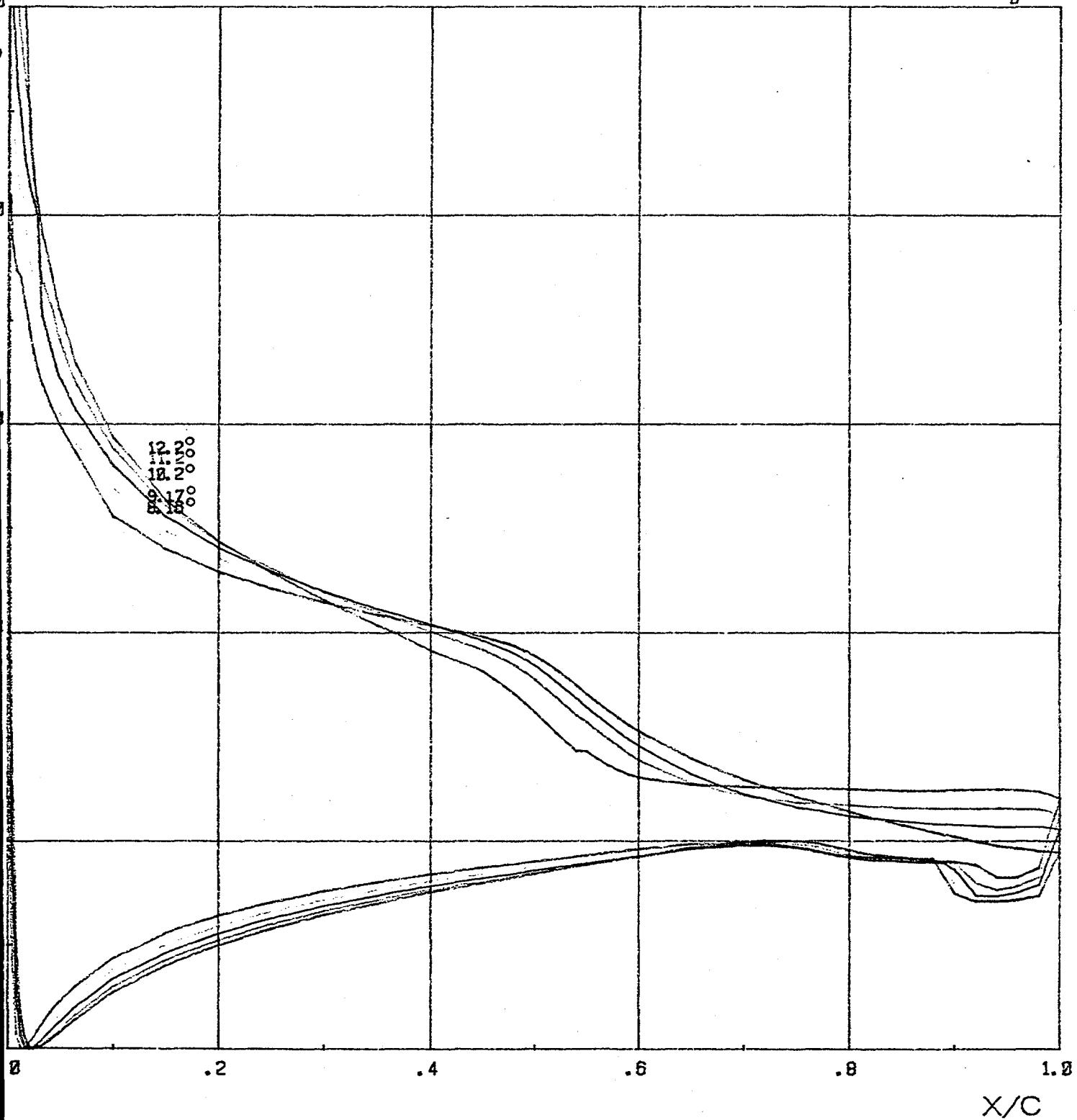
(c) α = 8.16, 9.17, 10.18, 11.19, and 12.19 degrees.

Figure 8.- Continued.
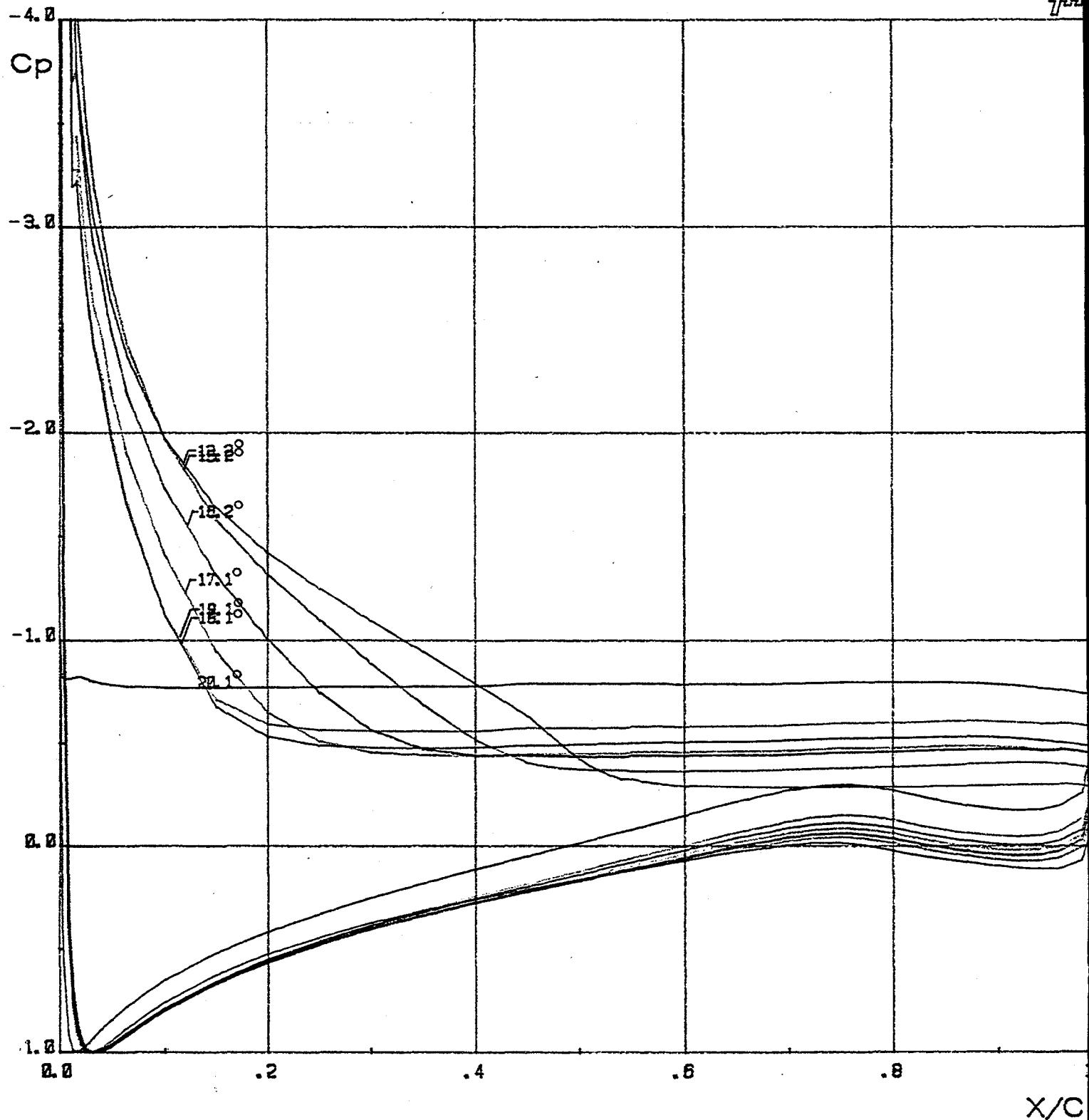
(d) α = 13.19, 15.20, 16.16, 17.14, 18.12, 19.13, and 20.06 degrees.

Figure 8.- Continued.
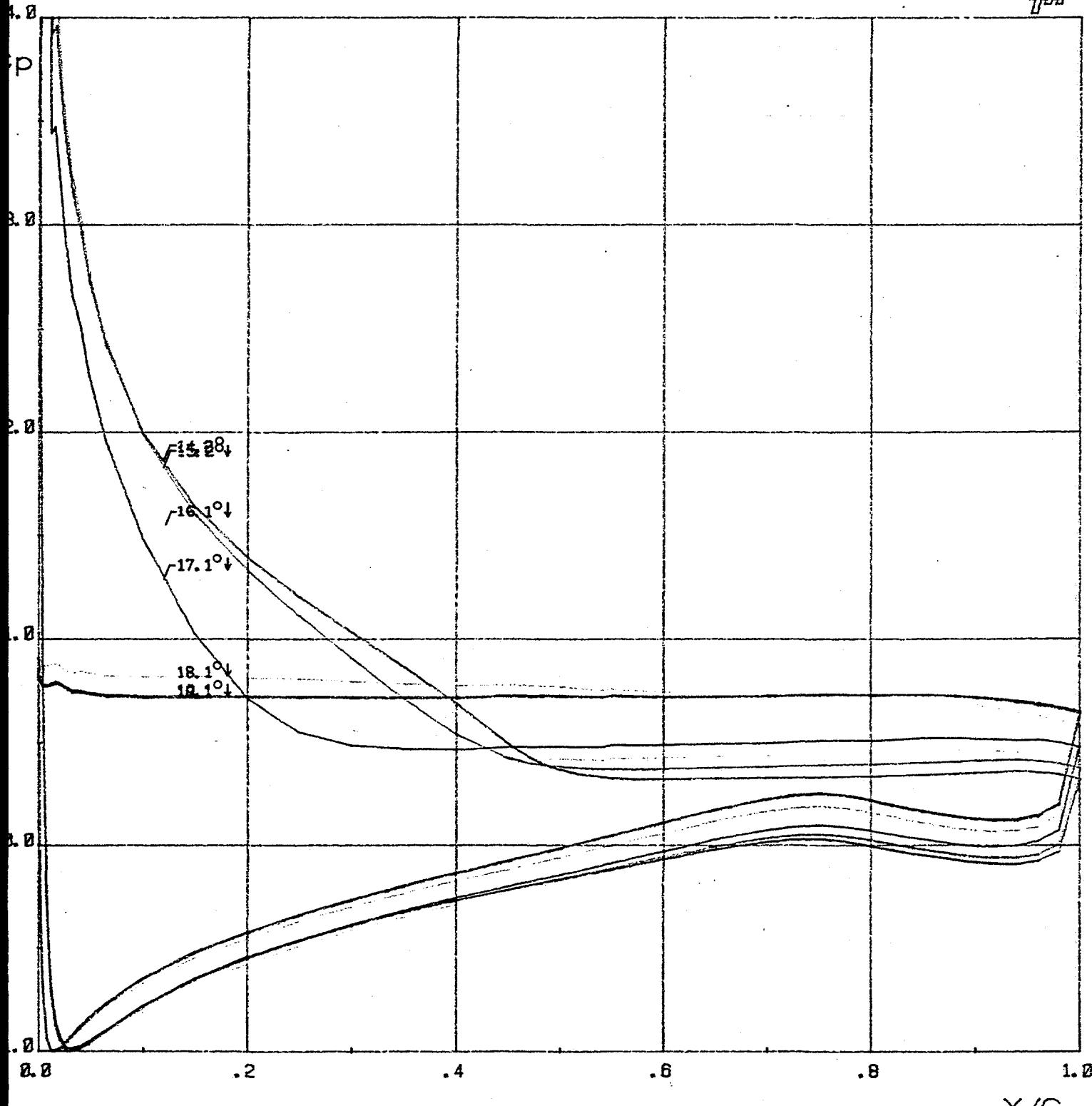
(e) $\alpha = 19.06\downarrow$, $18.07\downarrow$, $17.13\downarrow$, $16.15\downarrow$, $15.19\downarrow$, and 14.19 degrees.

Figure 8.- Continued.

31

R = 1.0 *10E6
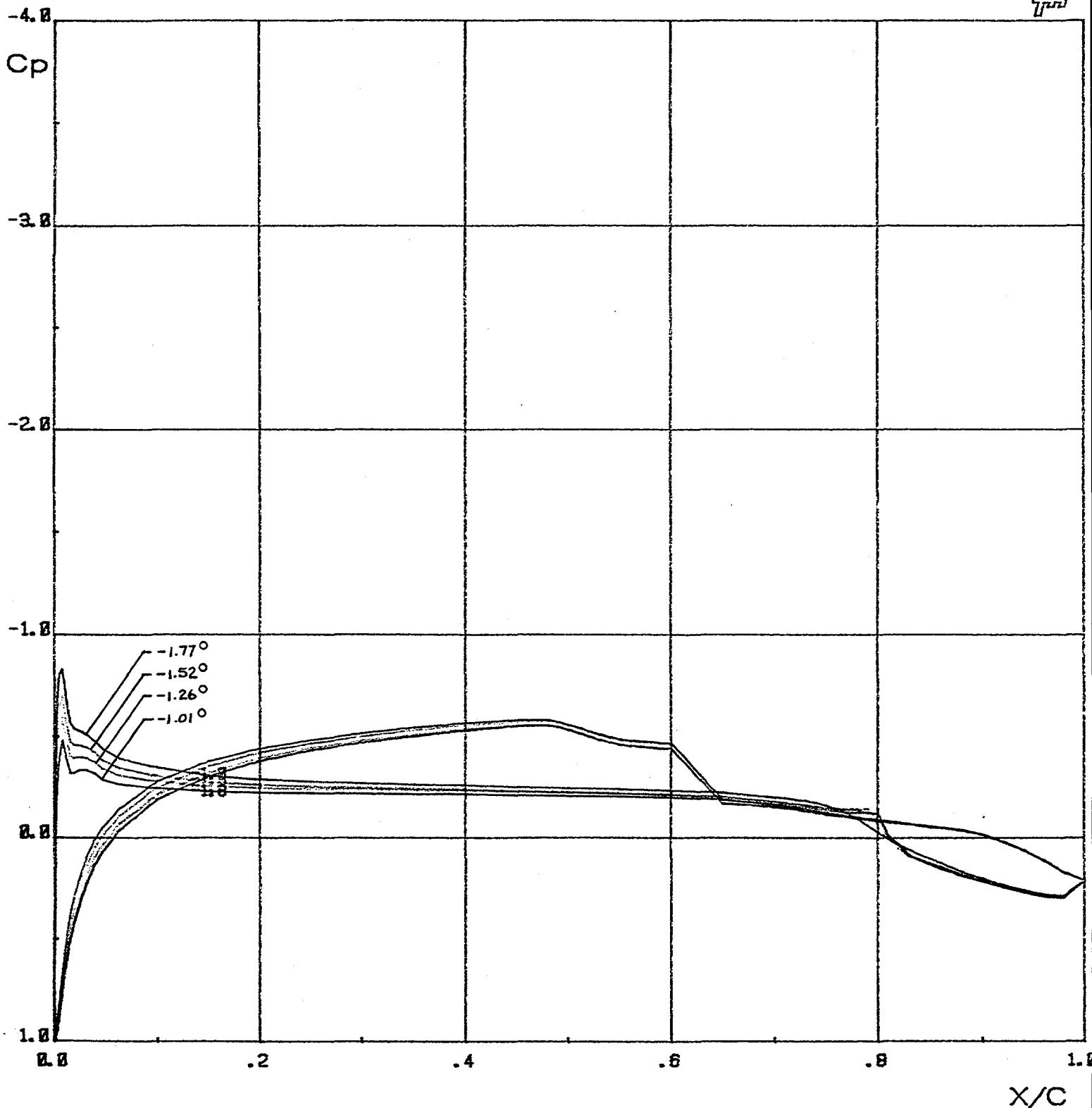
(f) α = -1.01, -1.26, -1.52, and -1.77 degrees.

Figure 8.- Continued.

32

R = 1.0 *10E6

-3.04°
-2.54°
-2.03°

X/C
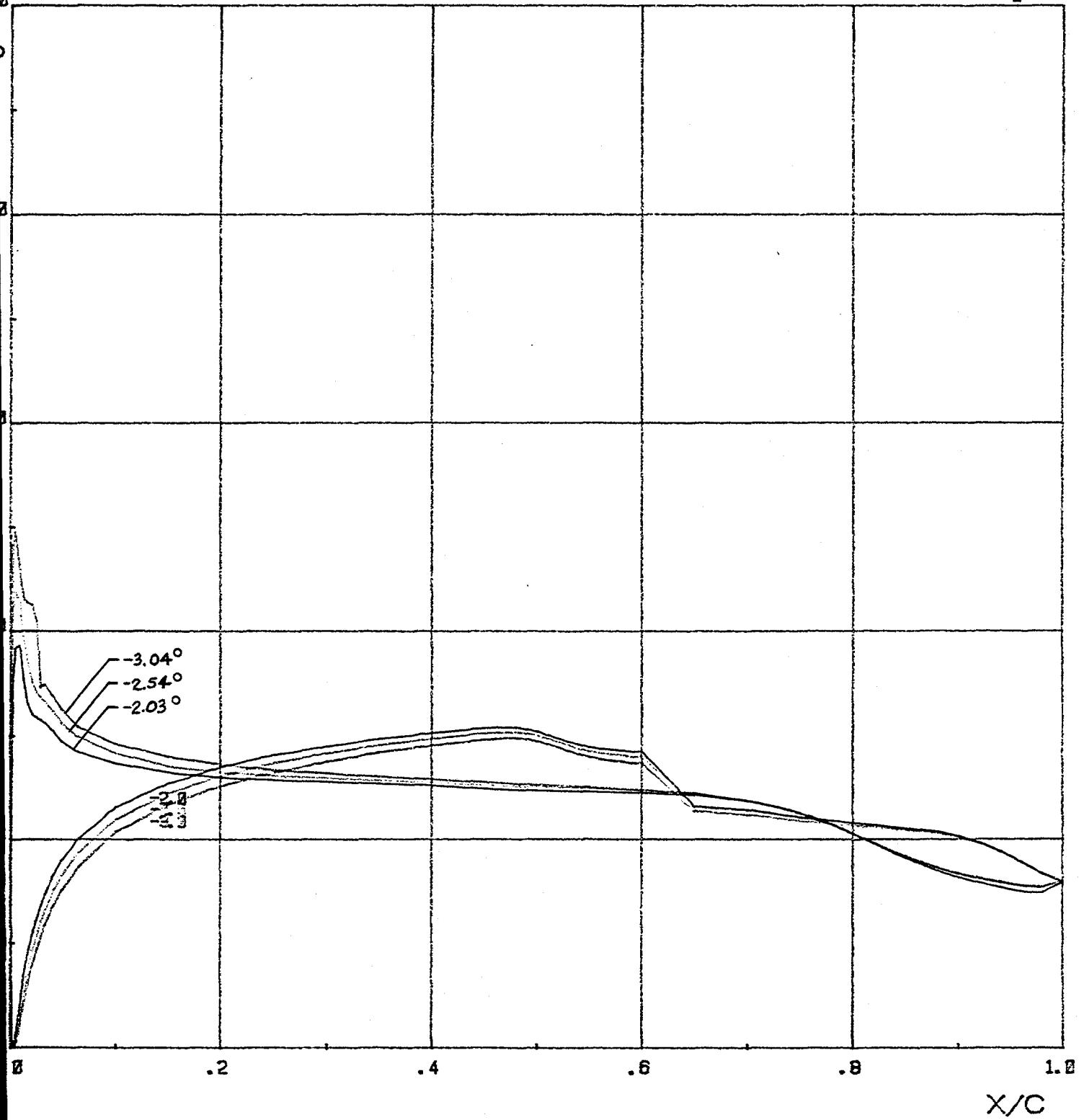
(g) α = -2.03, -2.54, and -3.04 degrees.

Figure 8.- Continued.

33
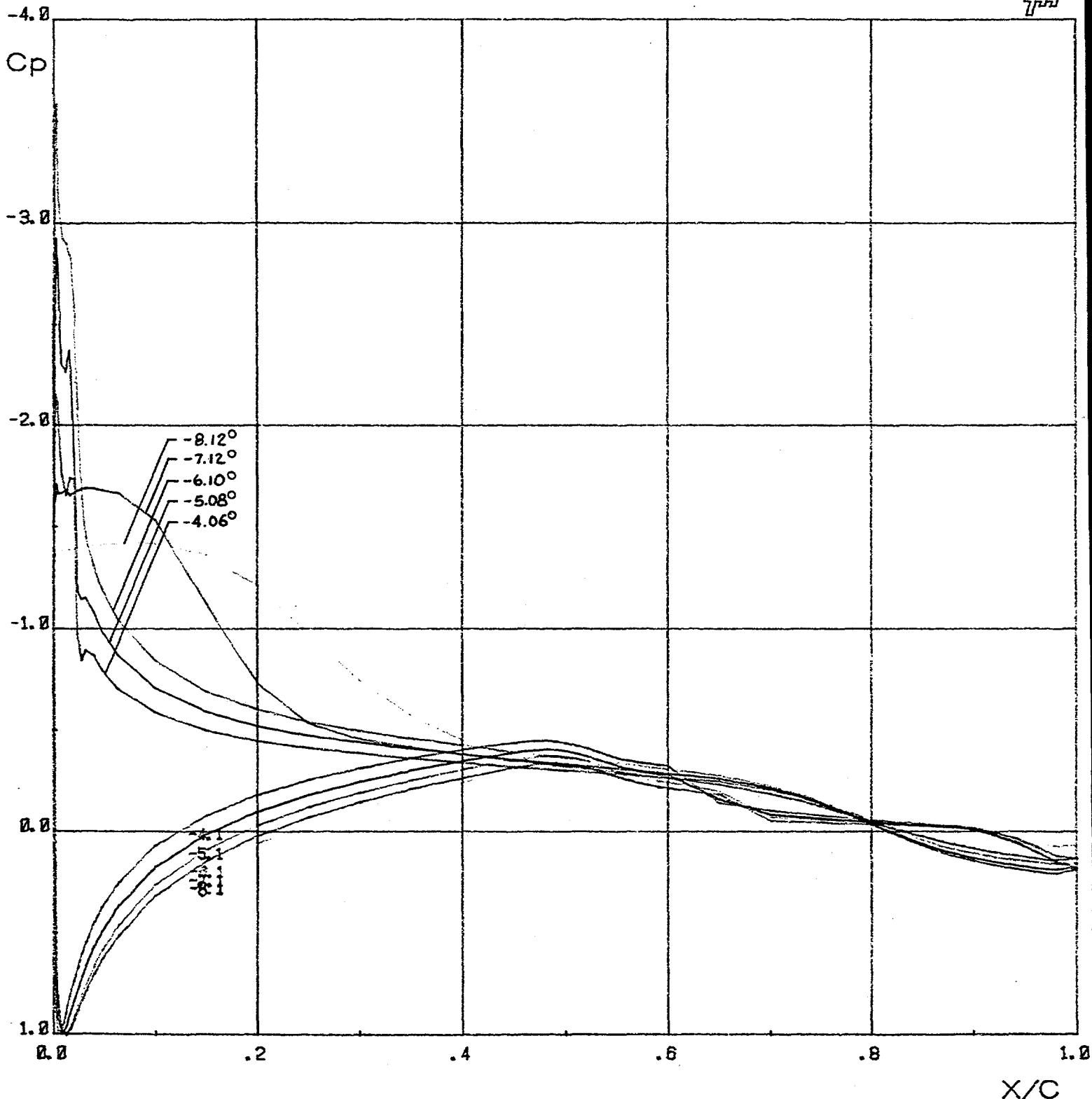
(h) $\alpha = -4.06, -5.08, -6.10, -7.12,$ and -8.12 degrees.

Figure 8.- Continued.
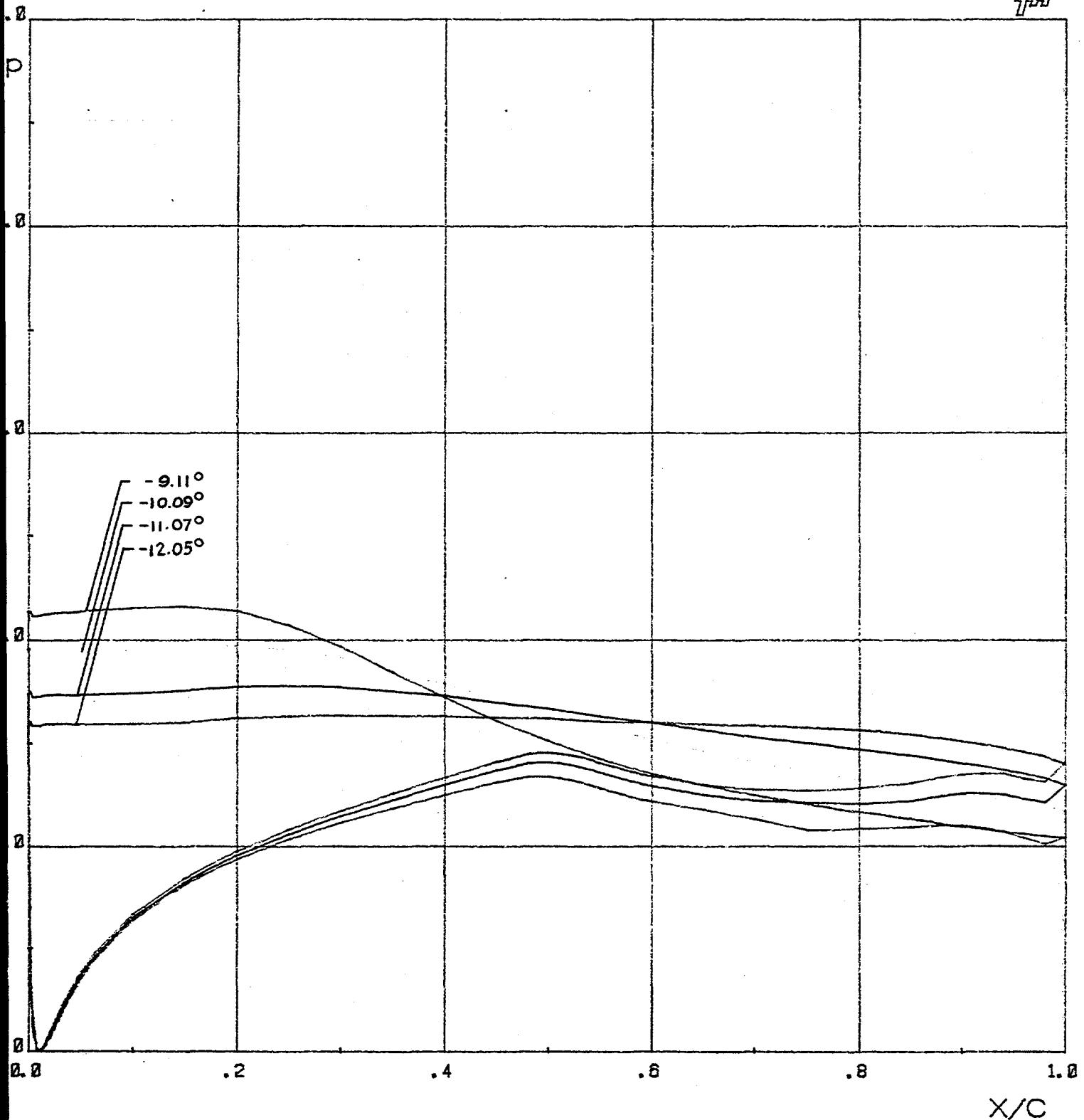
(i) α = -9.11, -10.09, -11.07, and -12.05 degrees.

Figure 8.- Continued.

35

R = 1.0 *10E6
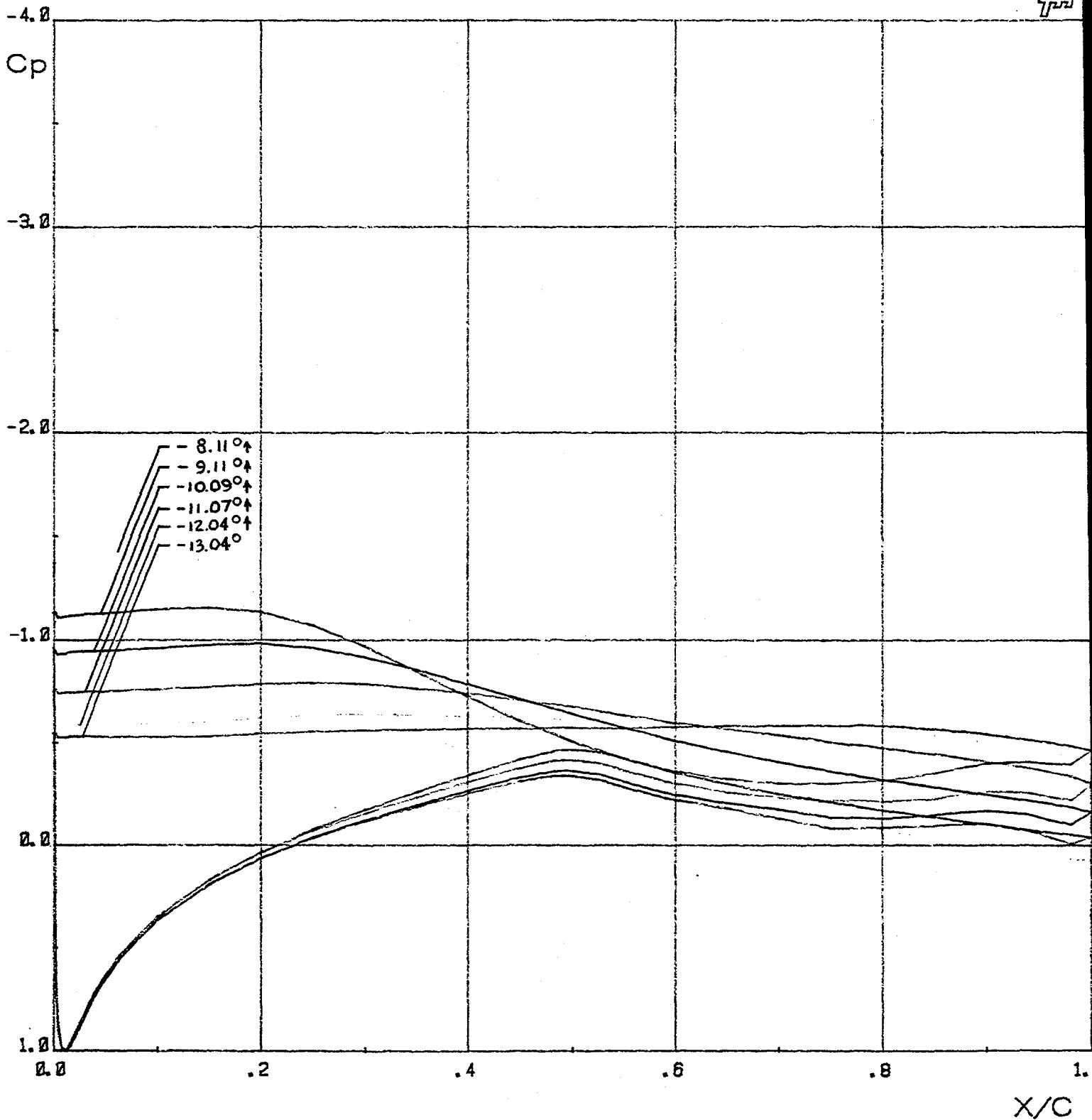
(j) α = -13.04, -12.04↑, -11.07↑, -10.09↑, -9.11↑, and -8.11↑ degrees.

Figure 8.- Continued.

36

R = 1.0   *10E6
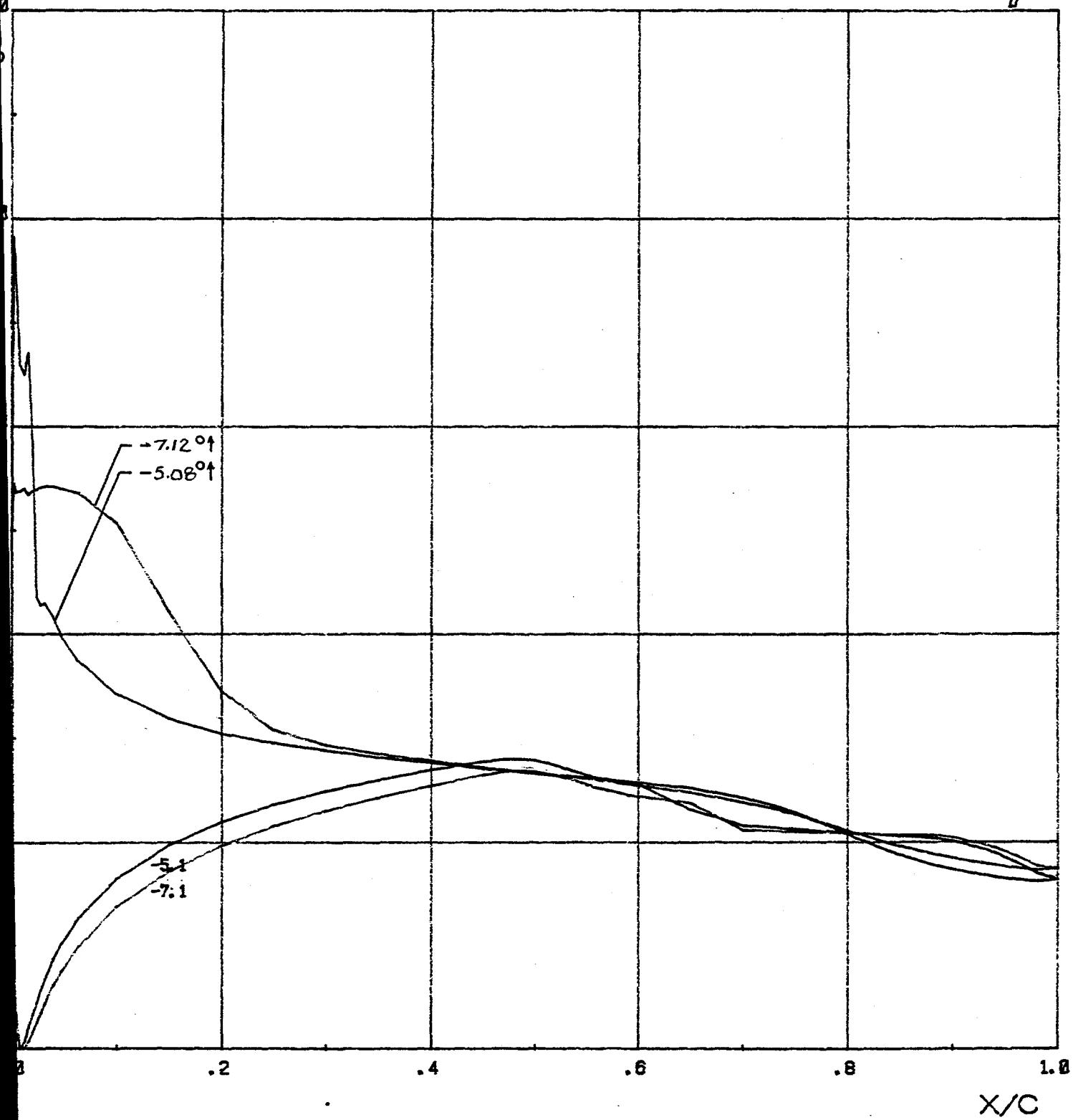
(k) α = -7.12↑ and -5.08↑ degrees.

Figure 8.- Concluded.
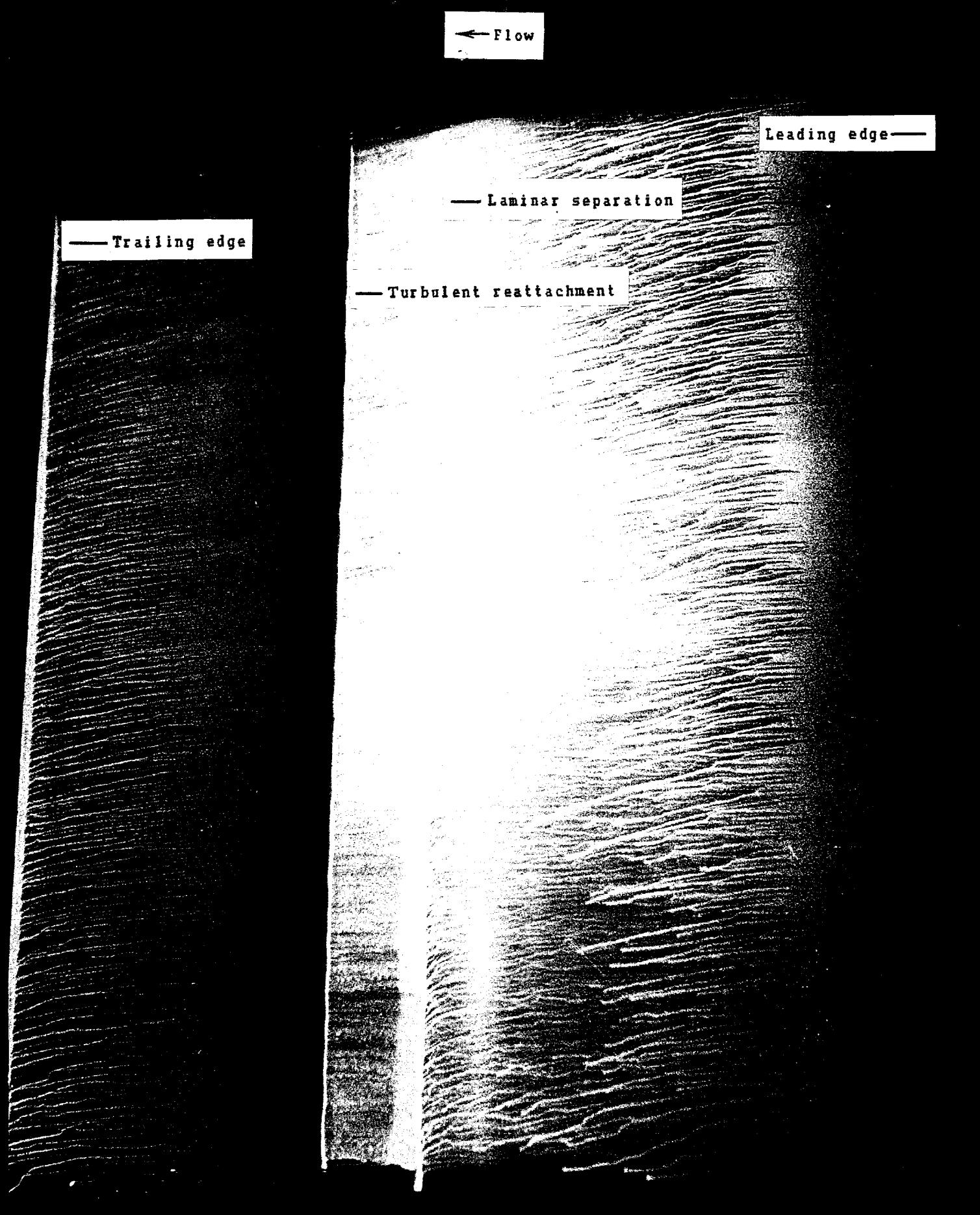
(a) α = 0.0 degrees.

Figure 9.– Oil-flow photographs of upper surface for R = 1,000,000.

38
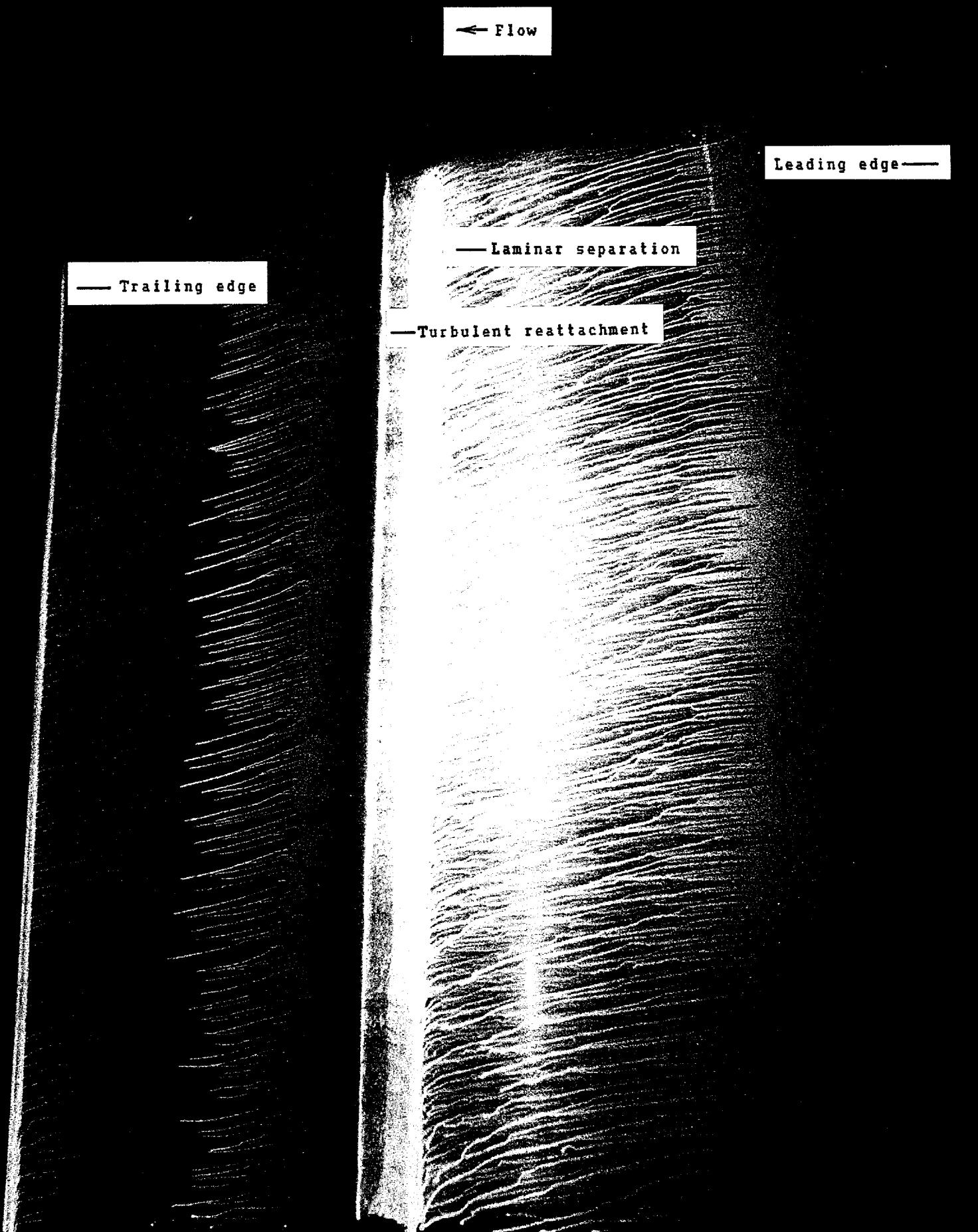
(b) α = 4.1 degrees.

Figure 9.- Continued.
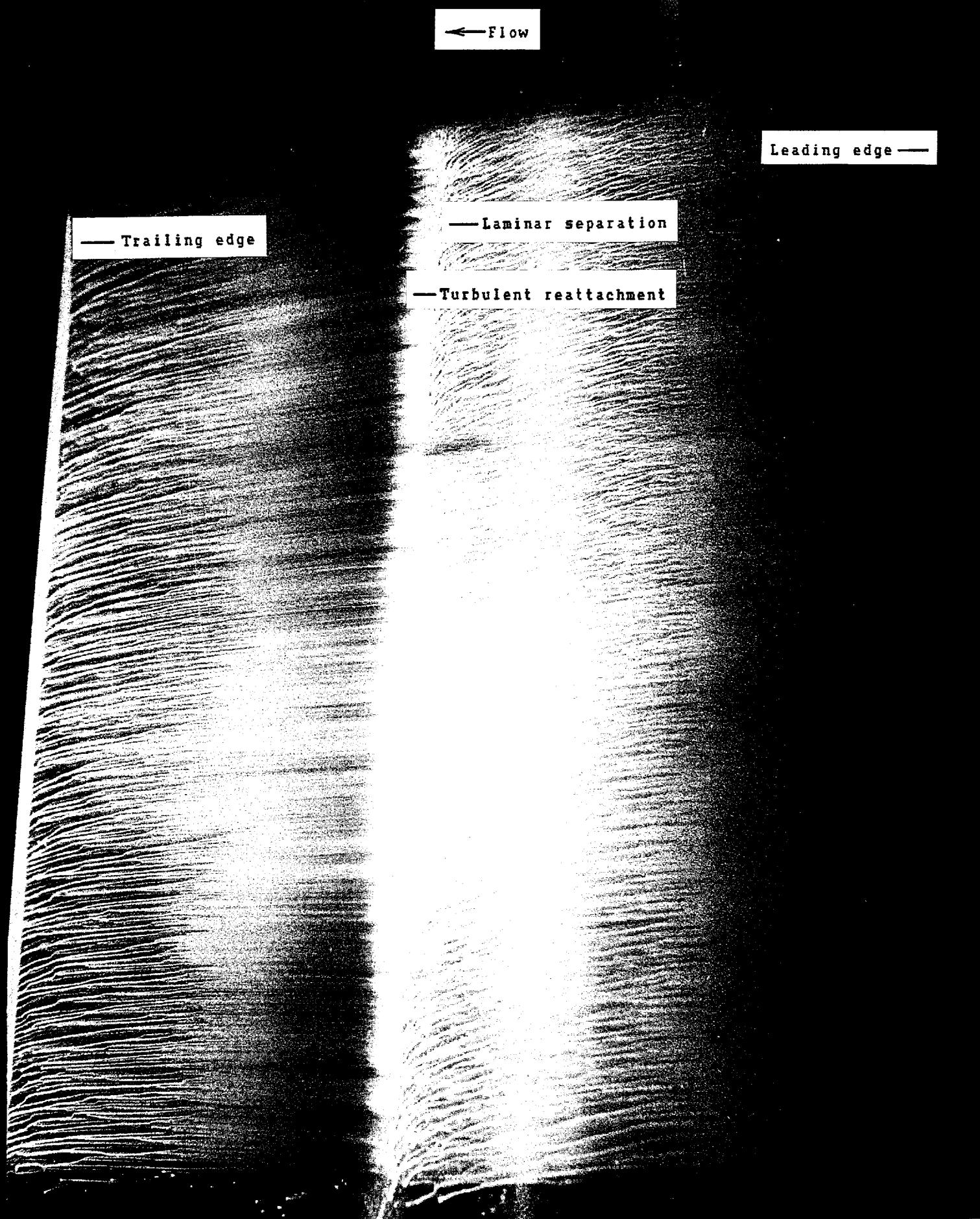
(c) α = 5.1 degrees.

Figure 9.- Continued.

(d) α = 8.2 degrees.

Figure 9.- Continued.

41

← Flow

Leading edge ——

Transition ——

—— Trailing edge

(e) α = 10.2 degrees.

Figure 9.- Continued.
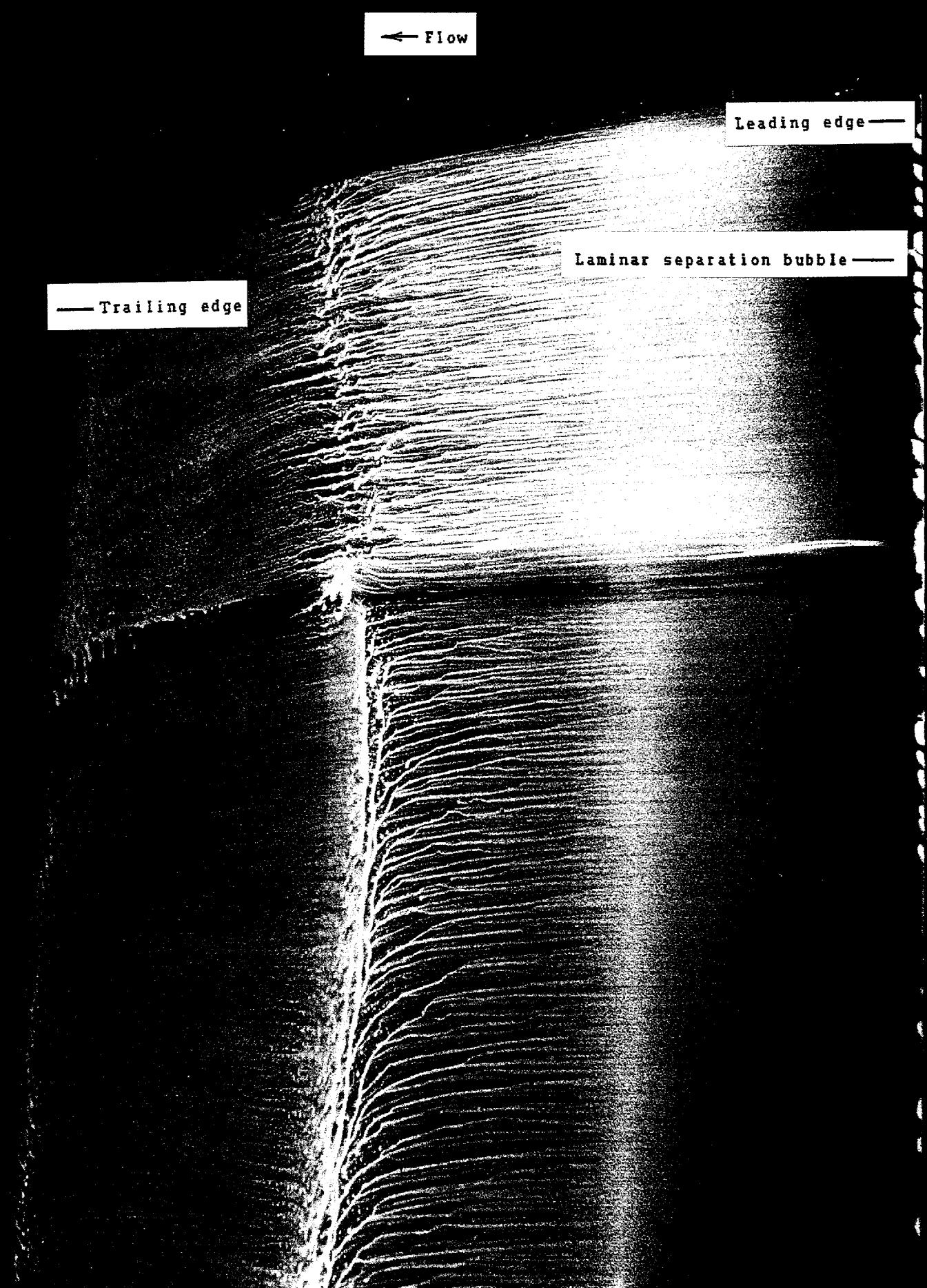
42

(f) α = 12.2 degrees.

Figure 9.- Concluded.

43

(a) α = 0.0 degrees.

Figure 10.– Oil-flow photographs of upper surface for R = 2,000,000.

44
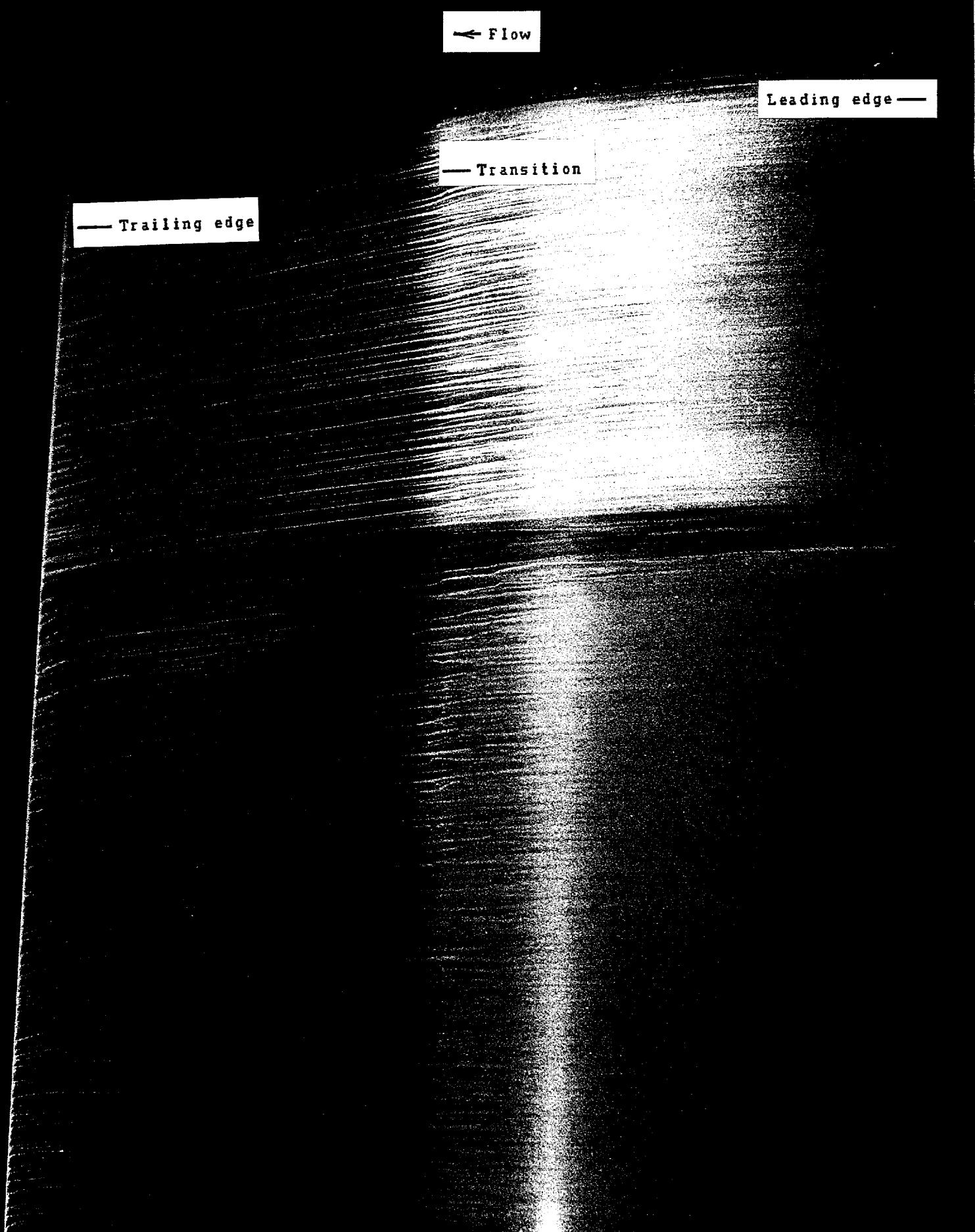
(b) α = 4.1 degrees.

Figure 10.- Continued.

45

(c) α = 5.1 degrees.

Figure 10.- Continued.

(d) $\alpha = 8.2$ degrees.

Figure 10.- Concluded.

Flow →

Leading edge

Trailing edge

Laminar separation

Turbulent reattachment
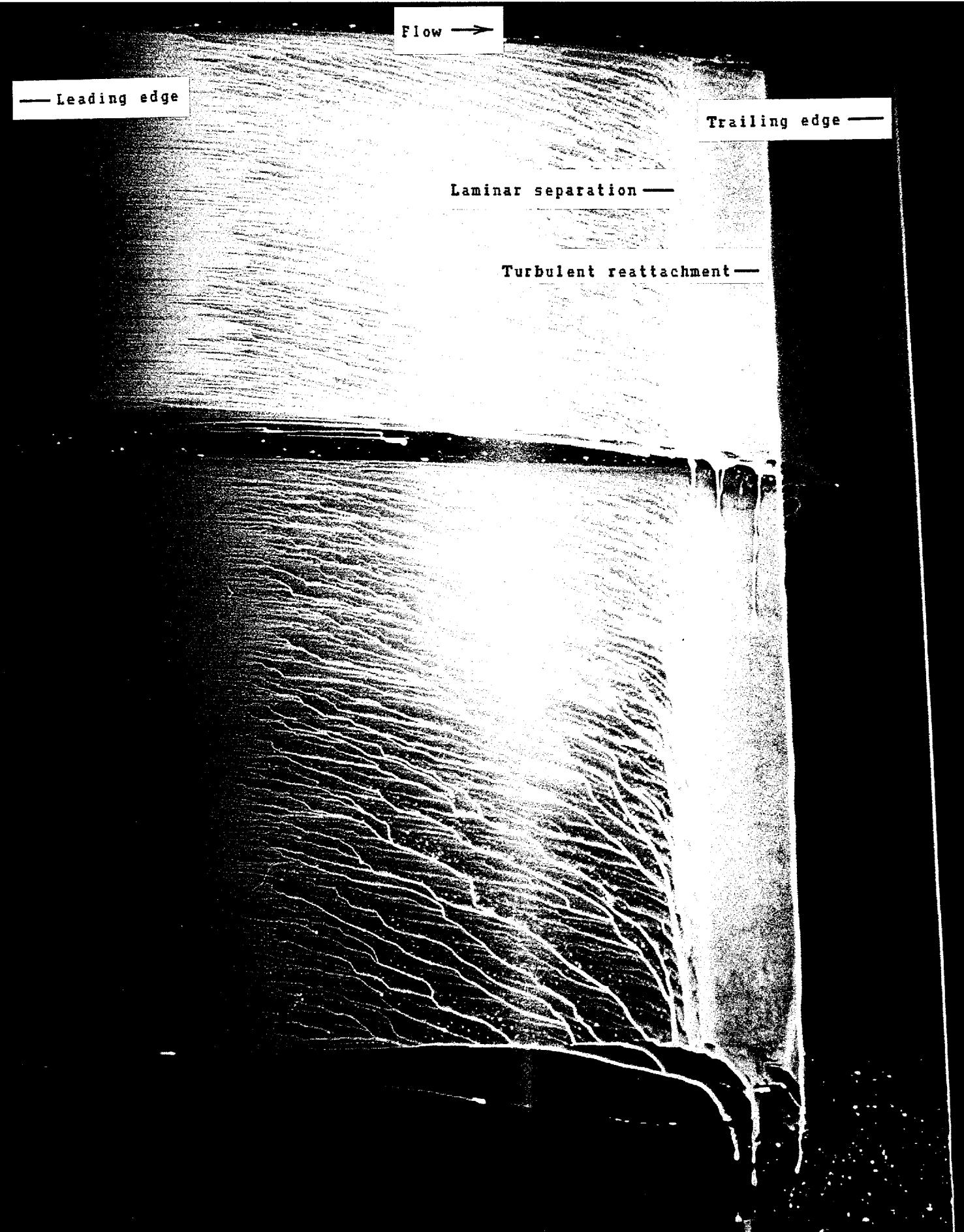
(a) α = 0.0 degrees.

Figure 11.- Oil-flow photographs of lower surface for R = 1,000,000.

48

Flow →

Leading edge

Trailing edge

Laminar separation

Turbulent reattachment

(b) α = 5.1 degrees.

Figure 11.- Continued.

49

Flow →

Leading edge

Trailing edge ——

Laminar separation——

Turbulent reattachment——

(c) $\alpha = -1.8$ degrees.

50

Figure 11.- Continued.

Flow →

Leading edge

Transition

Trailing edge →
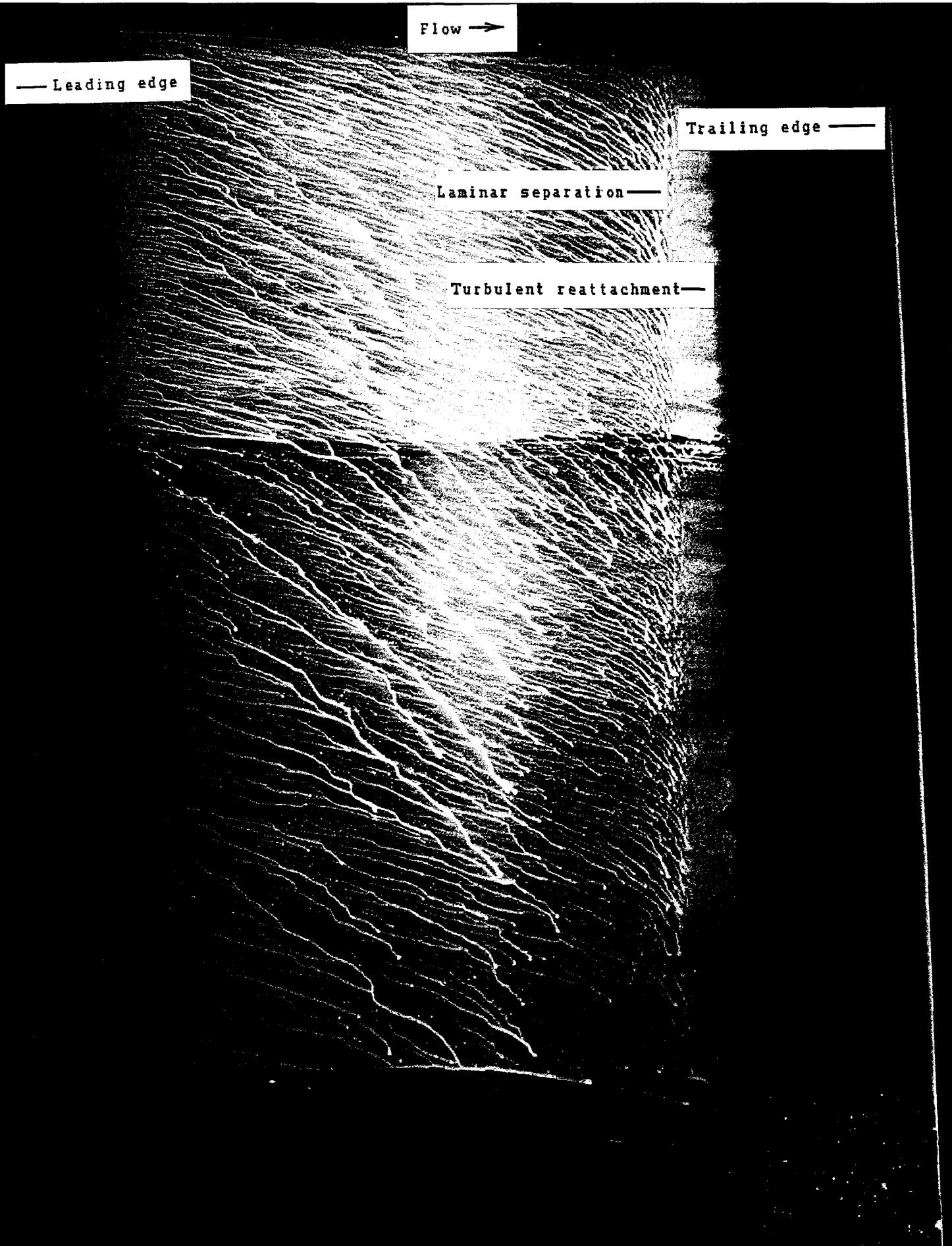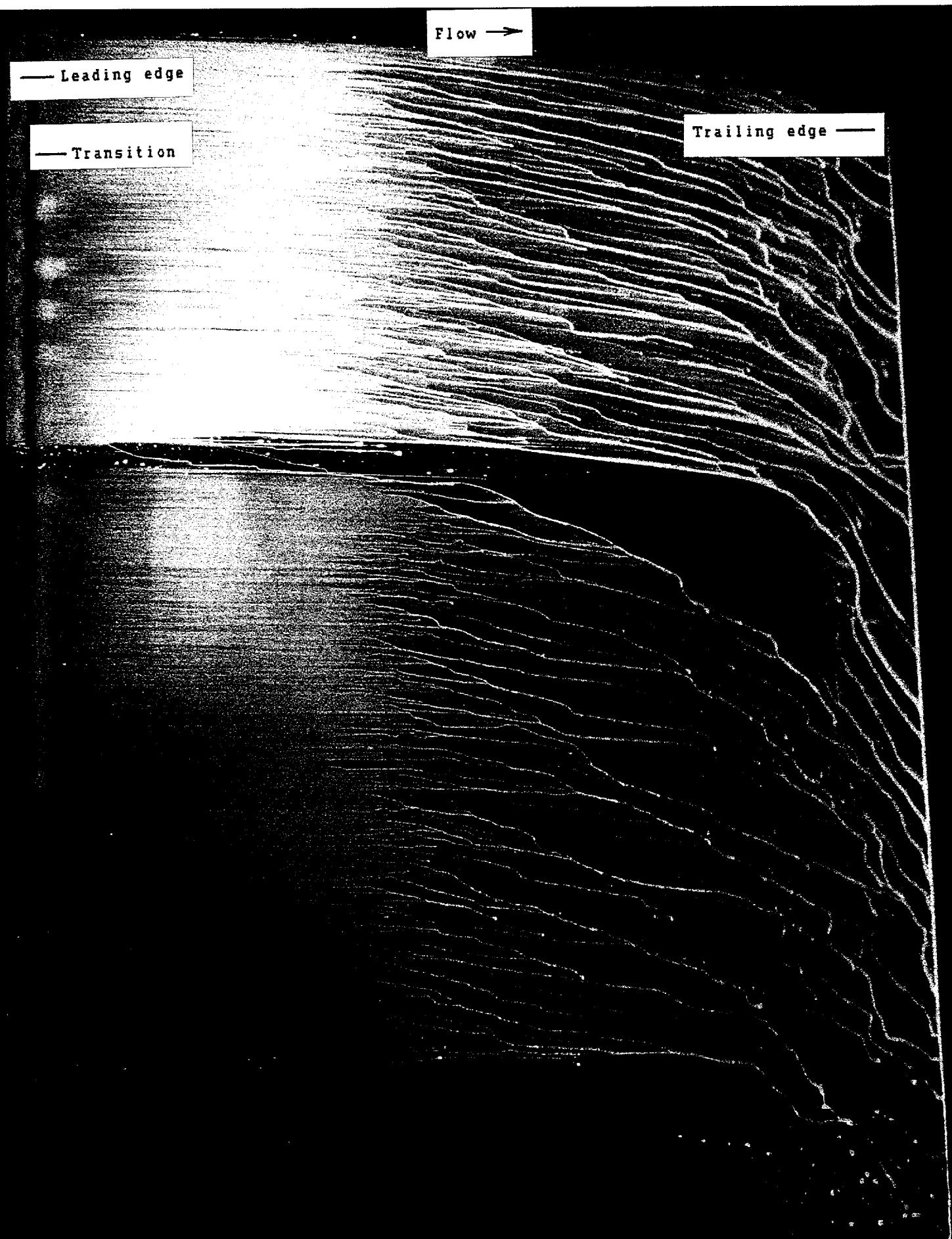
(d) $\alpha = -3.0$ degrees.

Figure 11.- Concluded.

Flow →

Leading edge

Trailing edge

Laminar separation

Turbulent reattachment

Figure 12.- Oil-flow photograph of lower surface at $\alpha = 0.0$ degrees for $R = 2,000,000$.

52
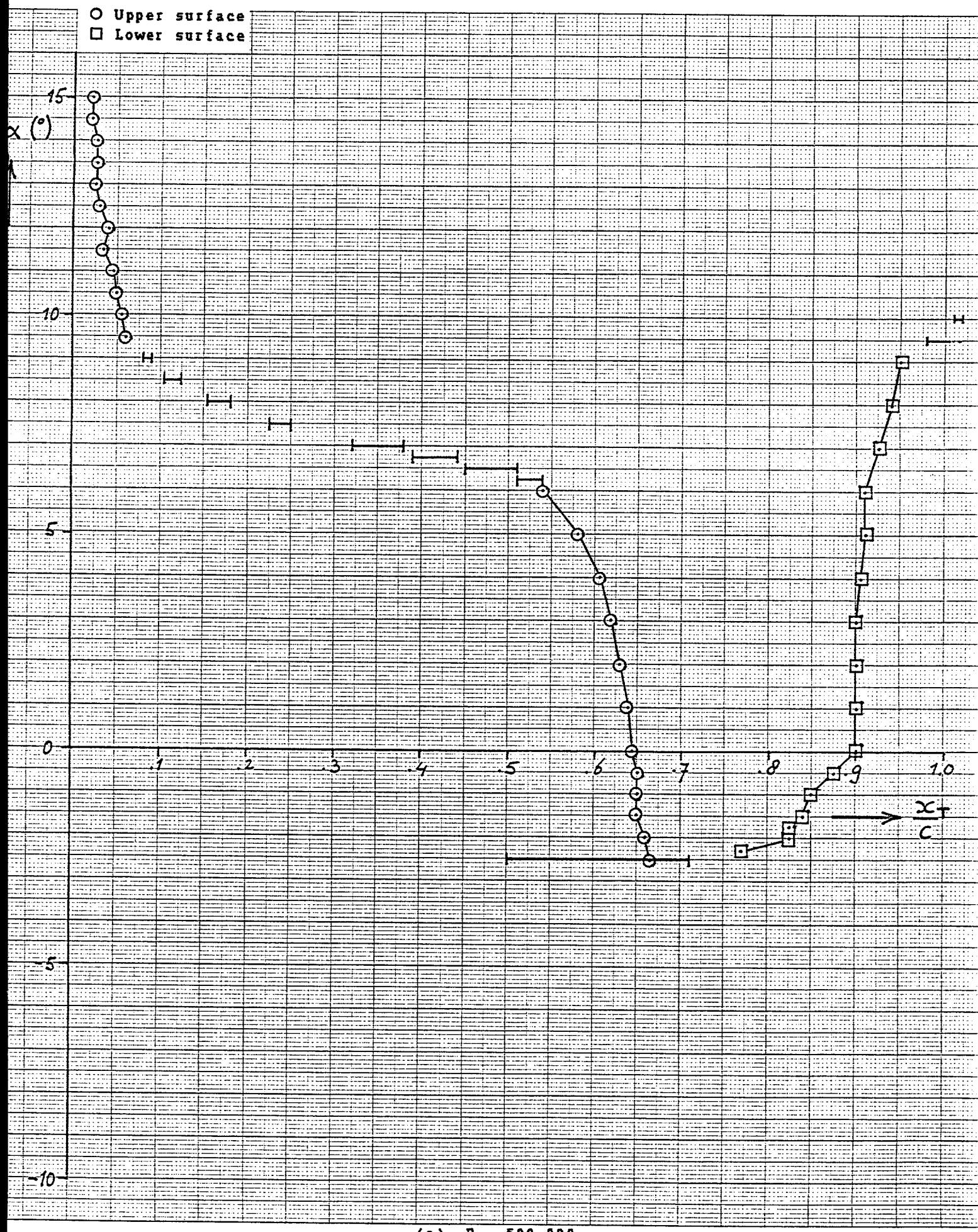
(a) R = 500,000.

Figure 13.- Transition location. Bars extend from beginning to end of
transition.

(b) R = 700,000.

Figure 13.- Continued.

54
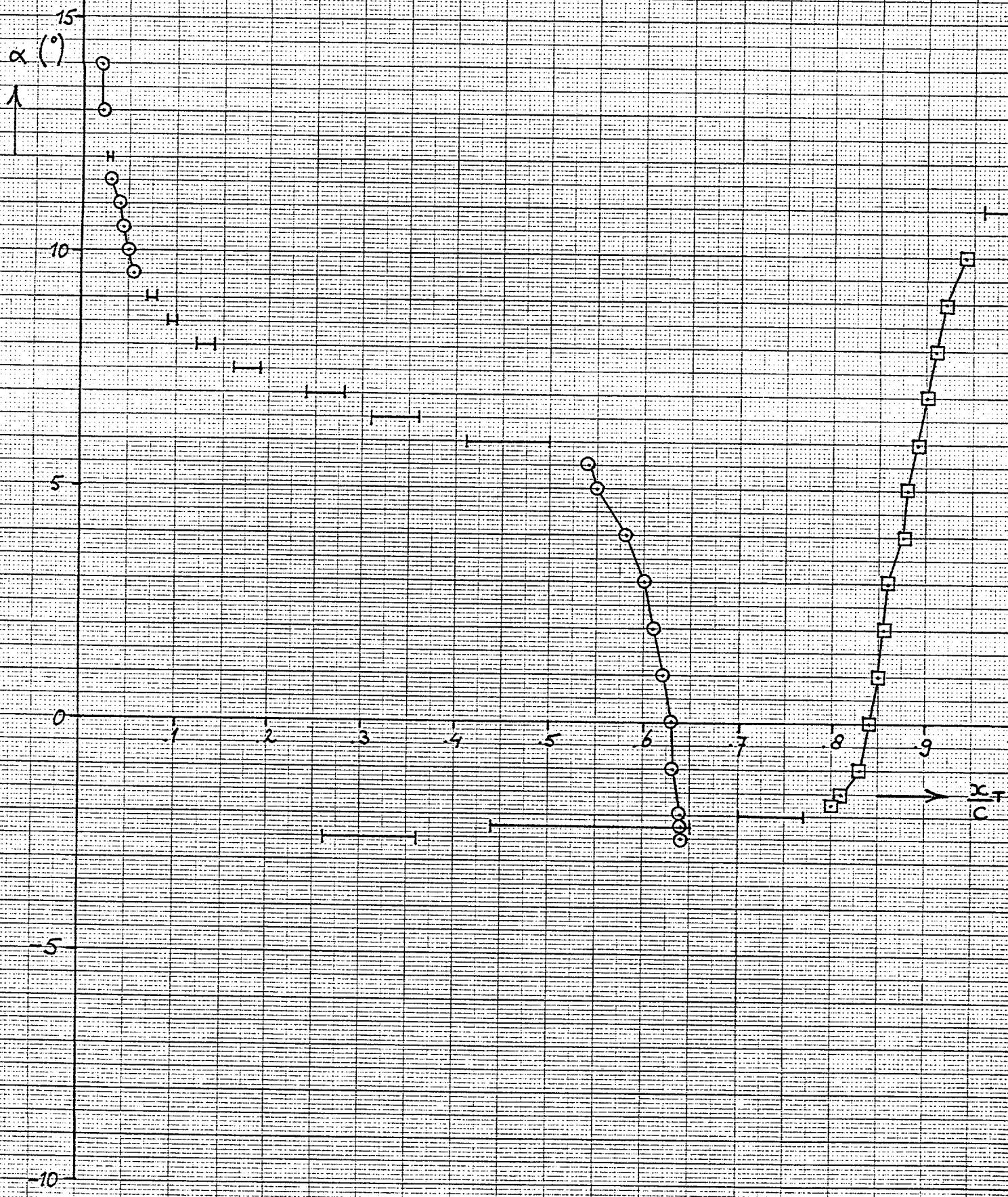
(c)   R = 1,000,000.

Figure 13.- Continued.
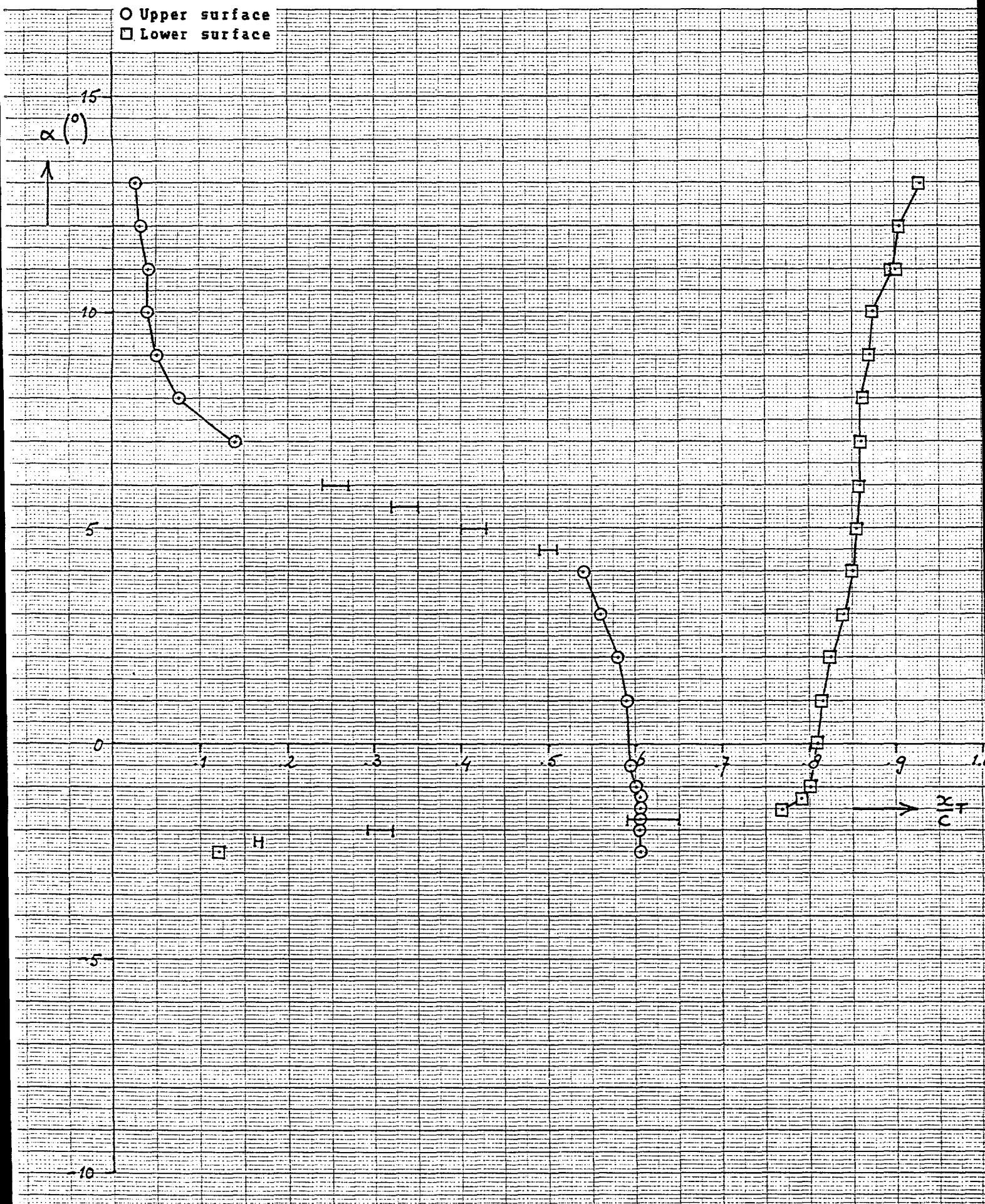
55

(d) R = 1,500,000.

Figure 13.- Continued.

(e) R = 2,000,000.

Figure 13.- Concluded.

57
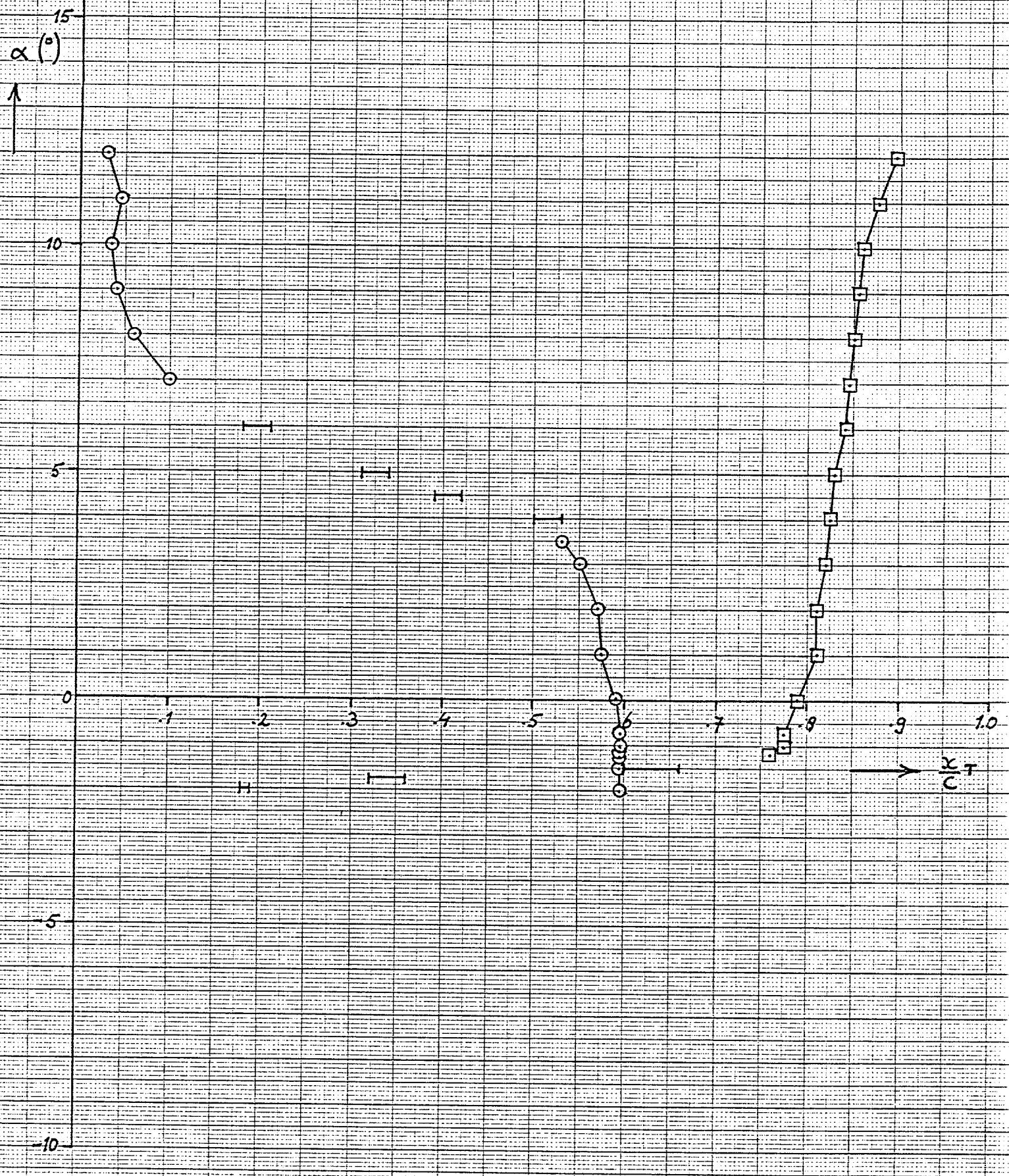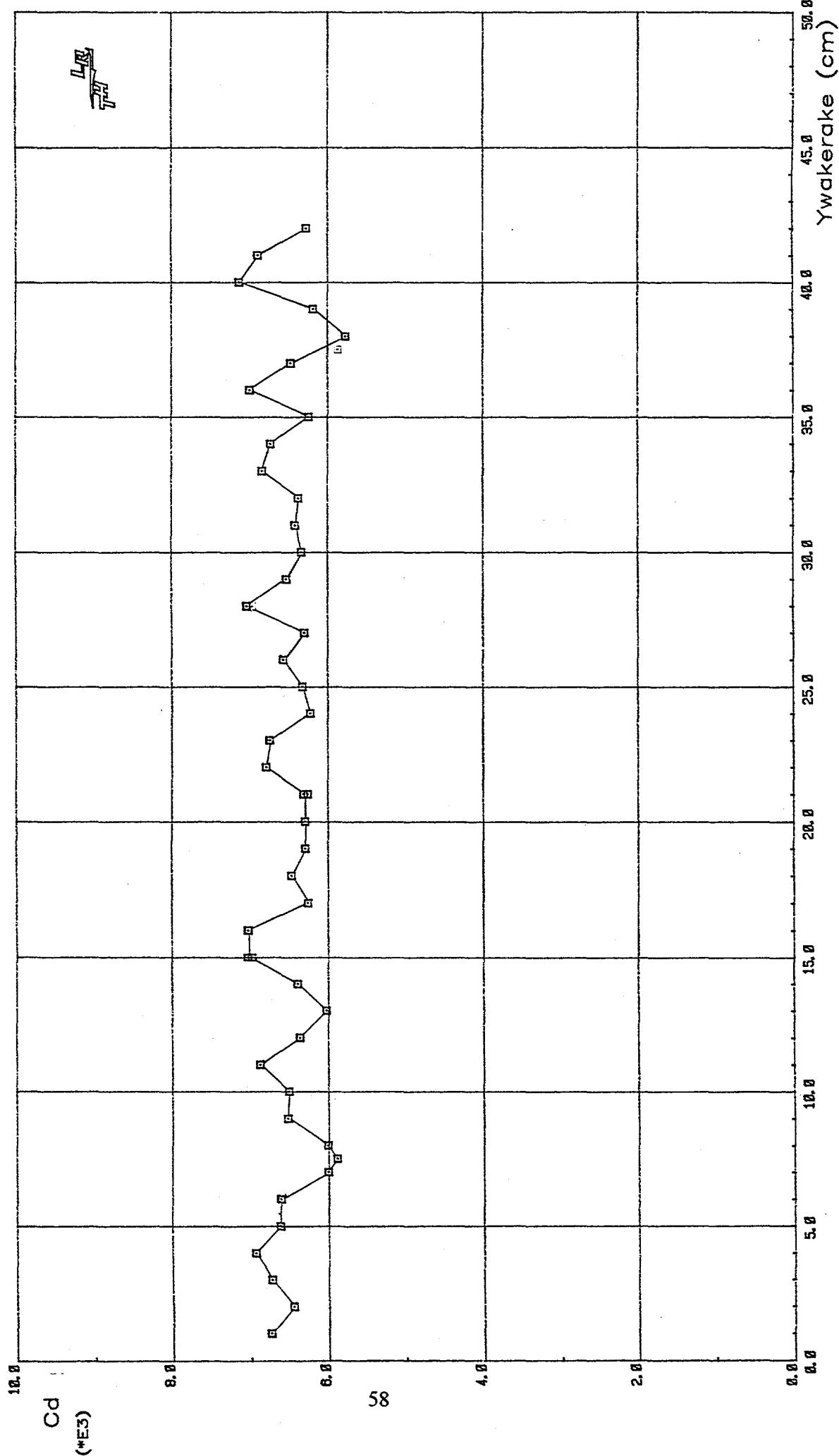
(a) ∝ = -1.5 degrees.

Figure 14.- Spanwise drag coefficients for R = 1,000,000.

58
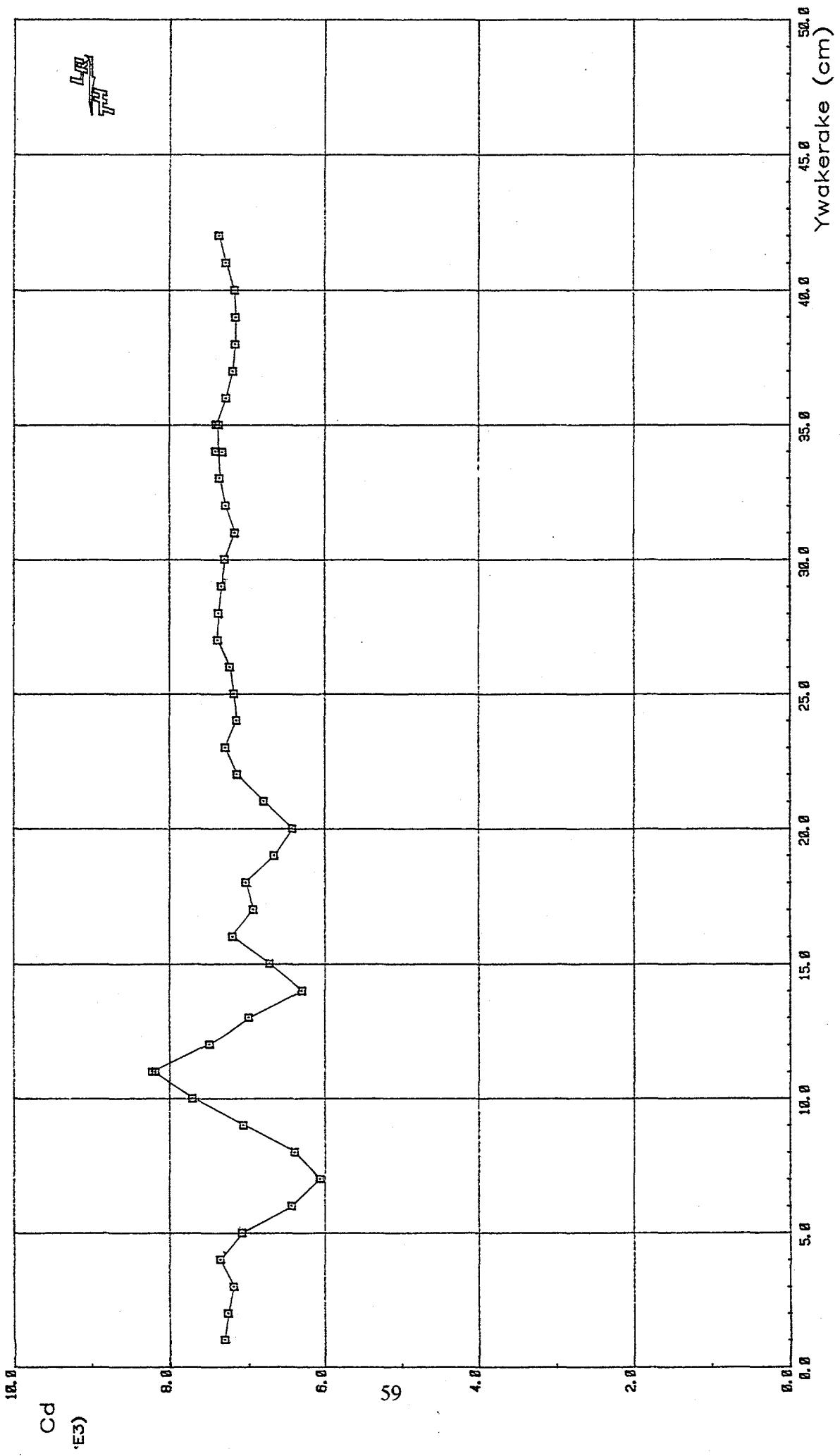
(b) α = 0.0 degrees.

Figure 14.- Continued.

59
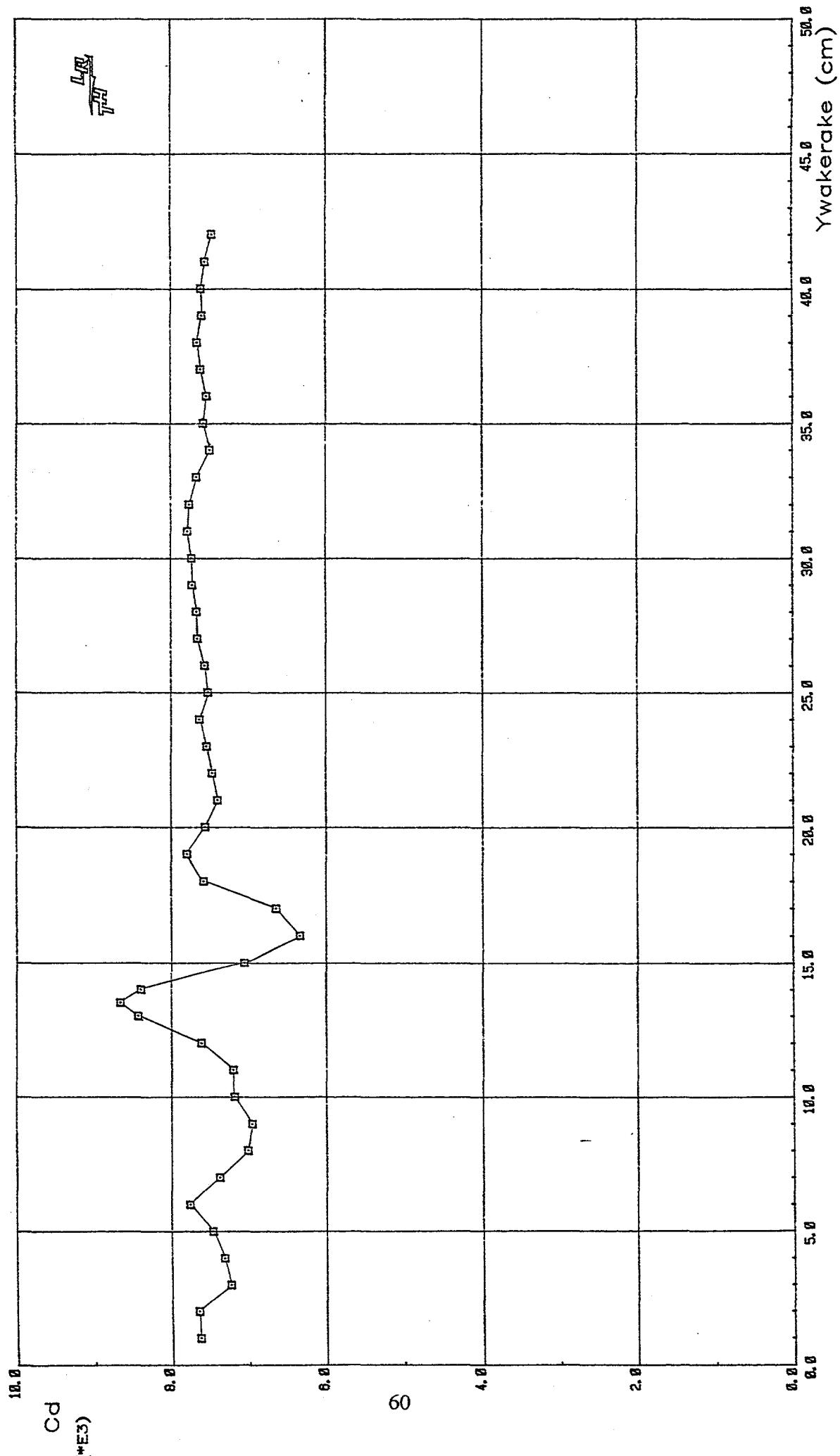
(c) α = 2.1 degrees.

Figure 14.- Continued.

60
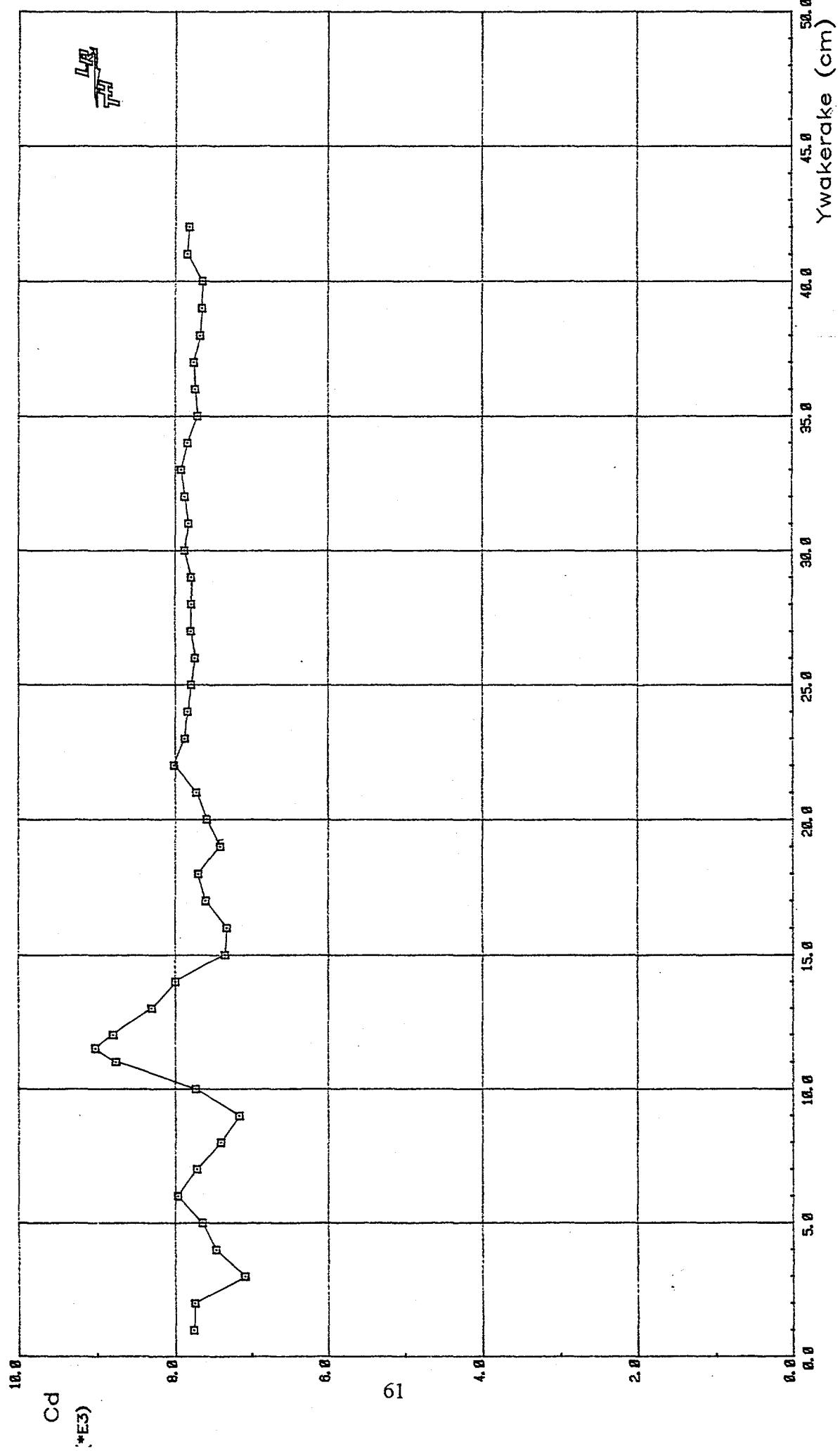
(d) $\alpha = 5.1$ degrees.

Figure 14.- Concluded.

61

Delft University of Technology
Low Speed Laboratory

C_m

α

C_l

C_d (*1000)
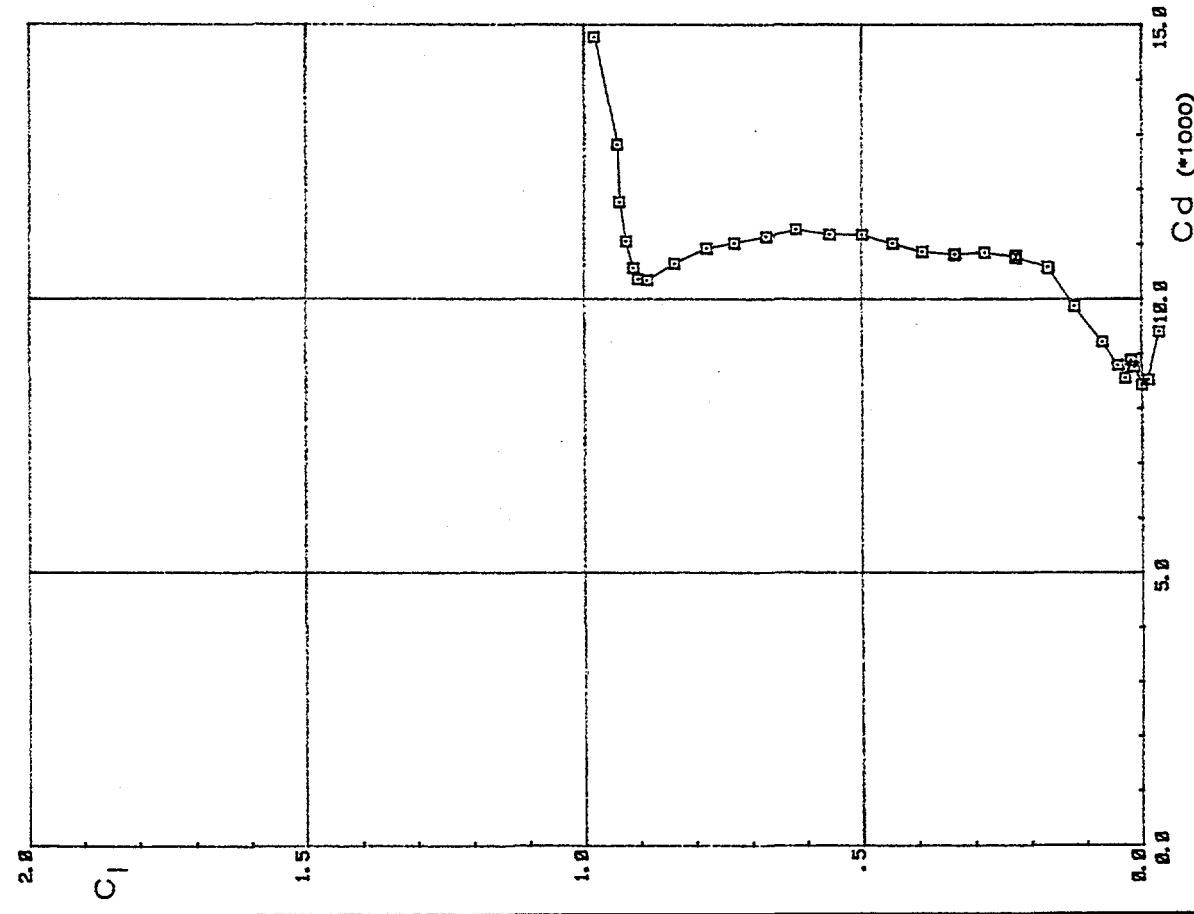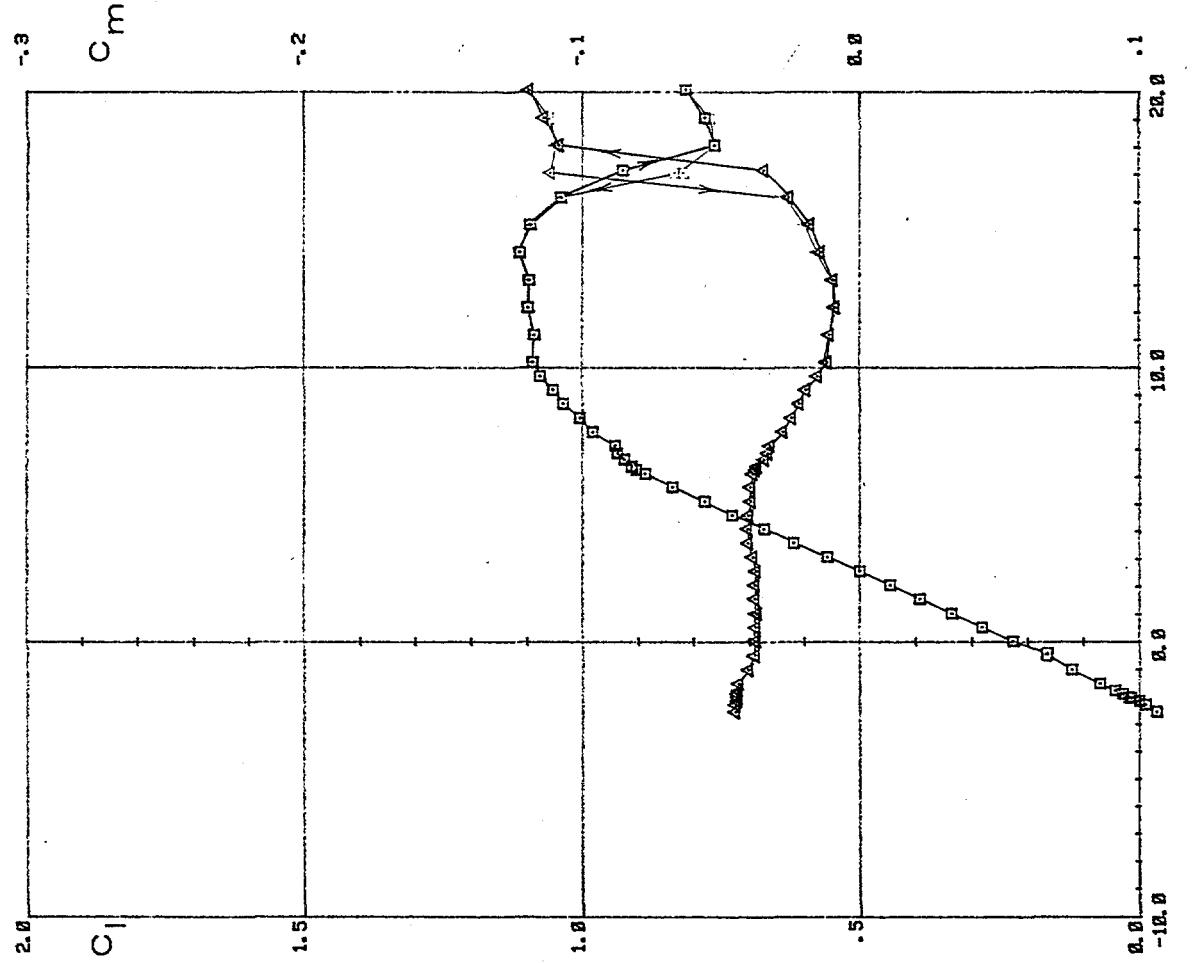
(a) R = 500,000.

Figure 15.- Section characteristics.

62

Delft University of Technology
Low Speed Laboratory

(b) R = 700,000.

Figure 15. - Continued.

63

Delft University of Technology $\frac{LR}{TU}$ Low Speed Laboratory

(c)   R = 1,000,000.

64

Delft University of Technology
Low Speed Laboratory

(d) R = 1,500,000.

Figure 15.- Continued.

65

Delft University of Technology
Low Speed Laboratory

(e) R = 2,000,000.

66

Delft University of Technology — Low Speed Laboratory
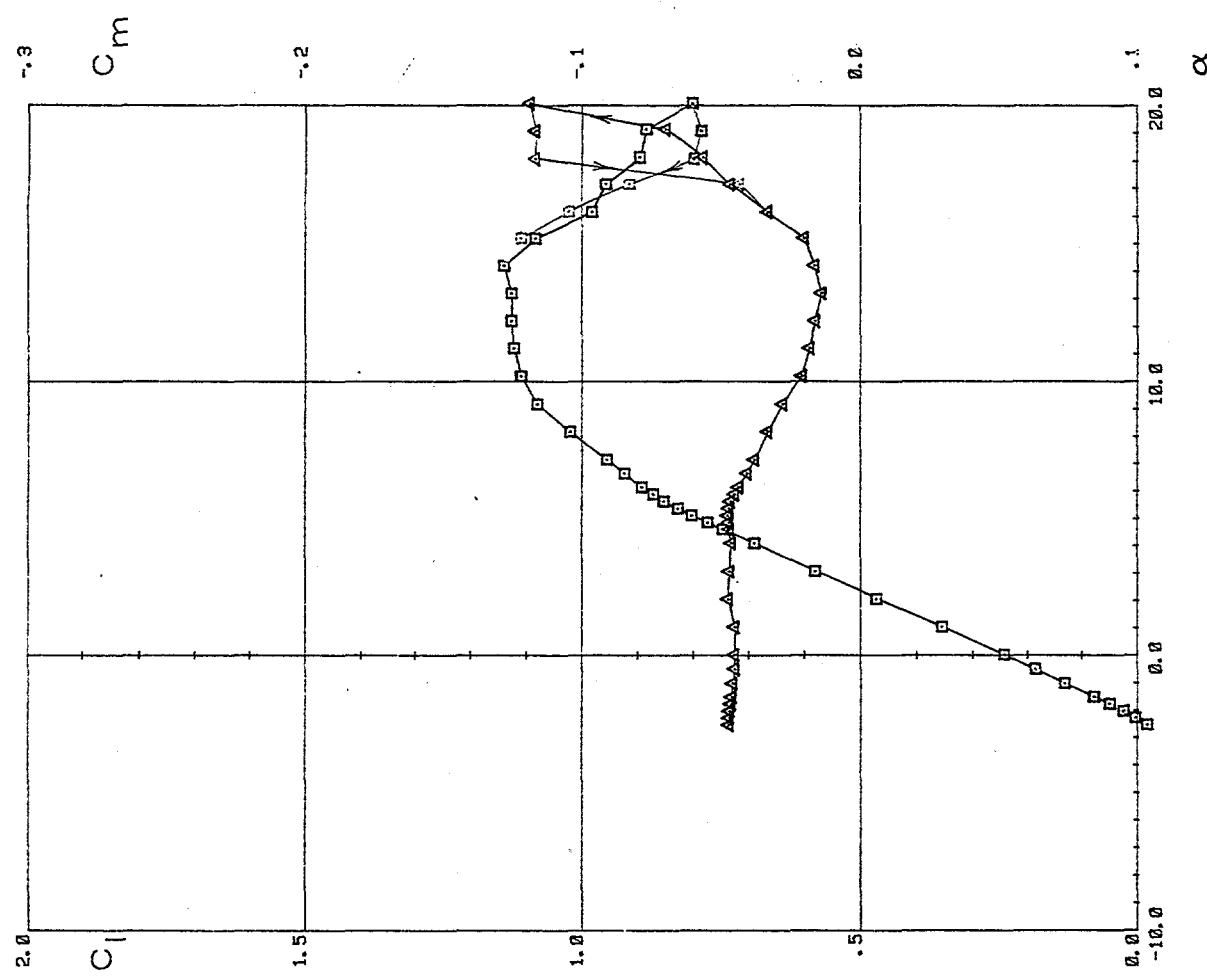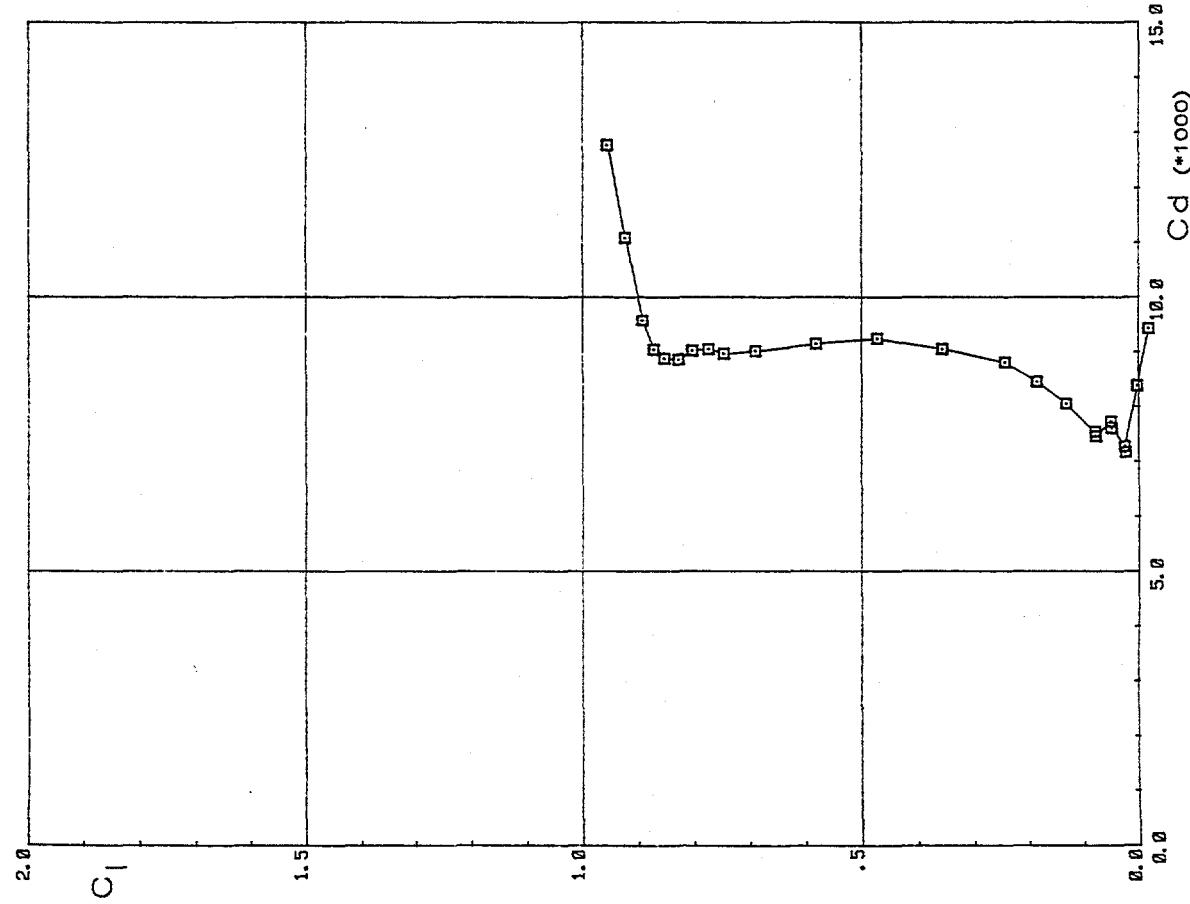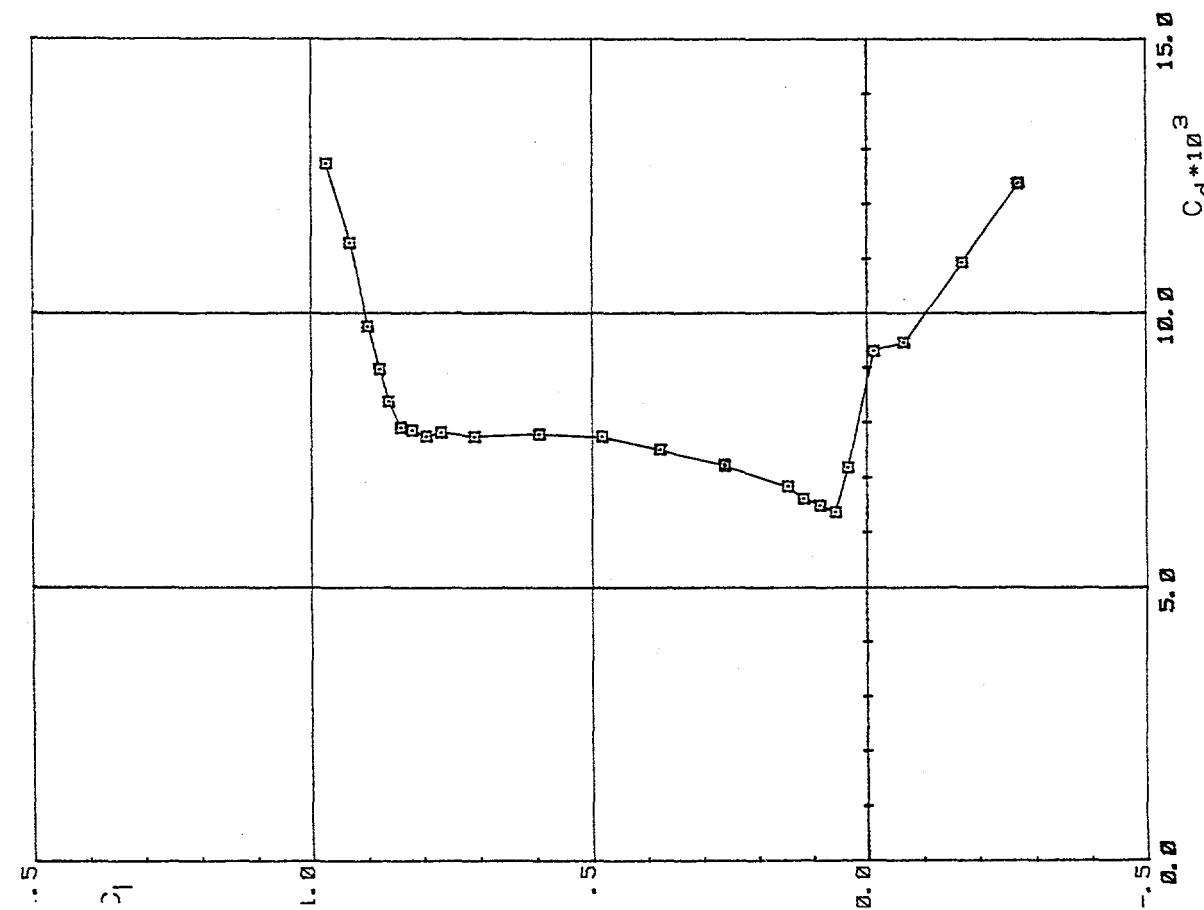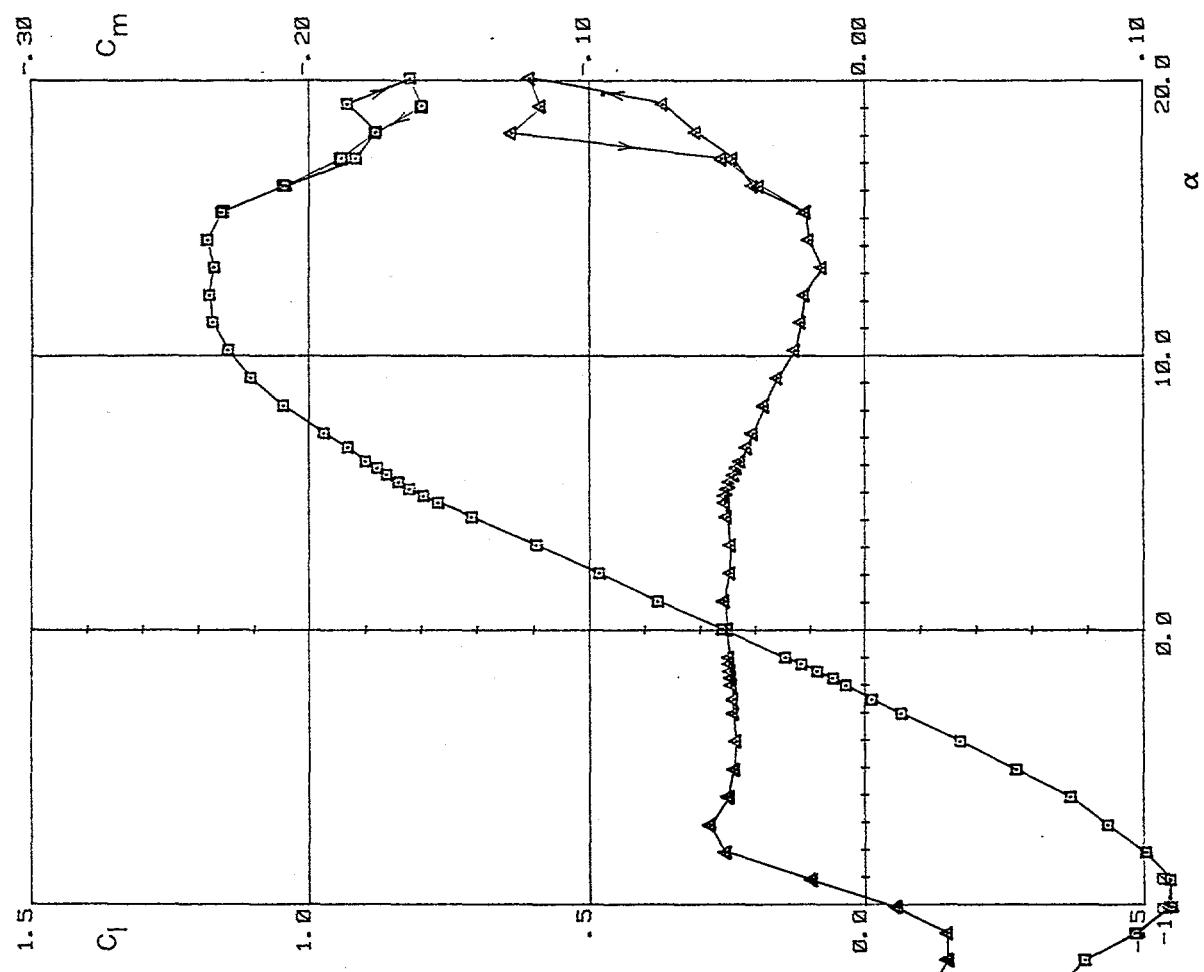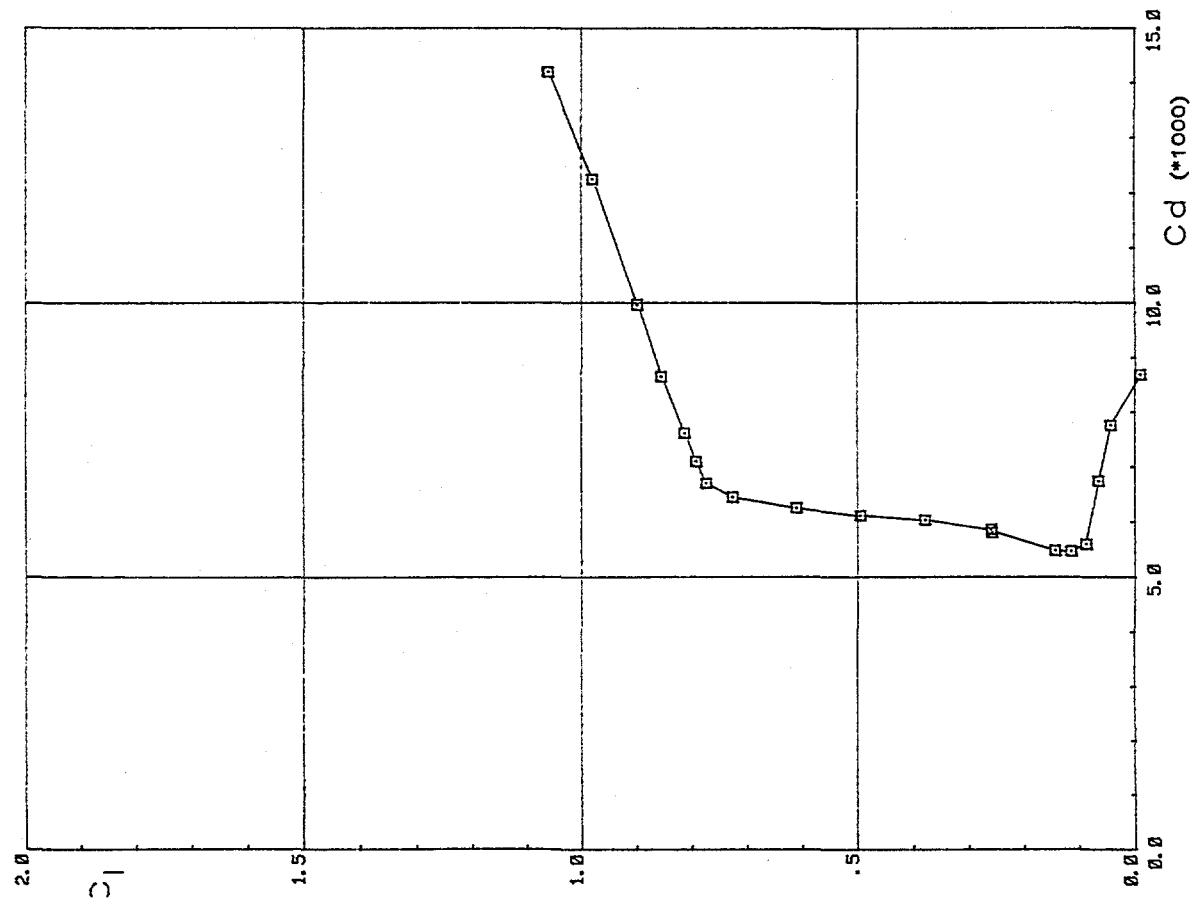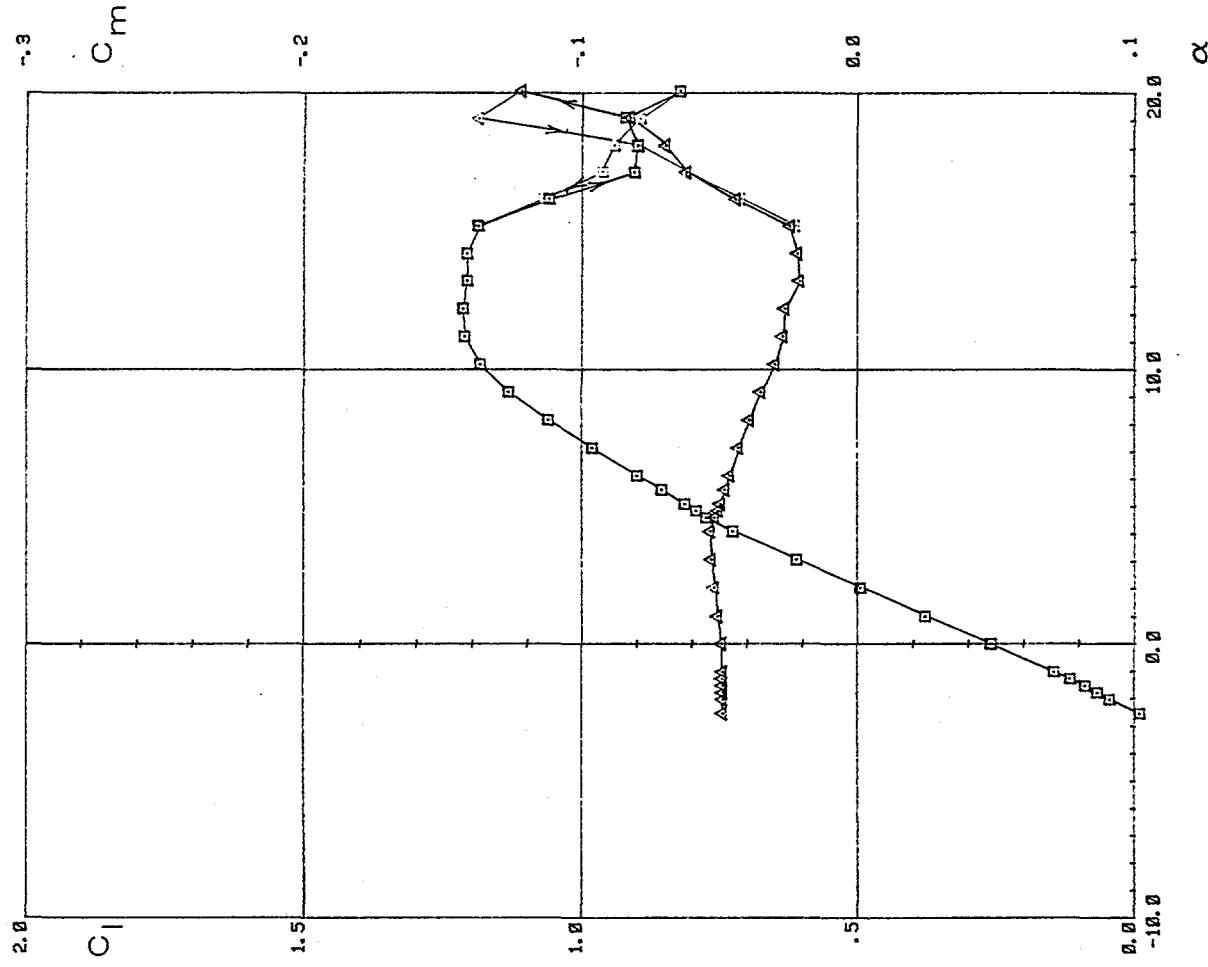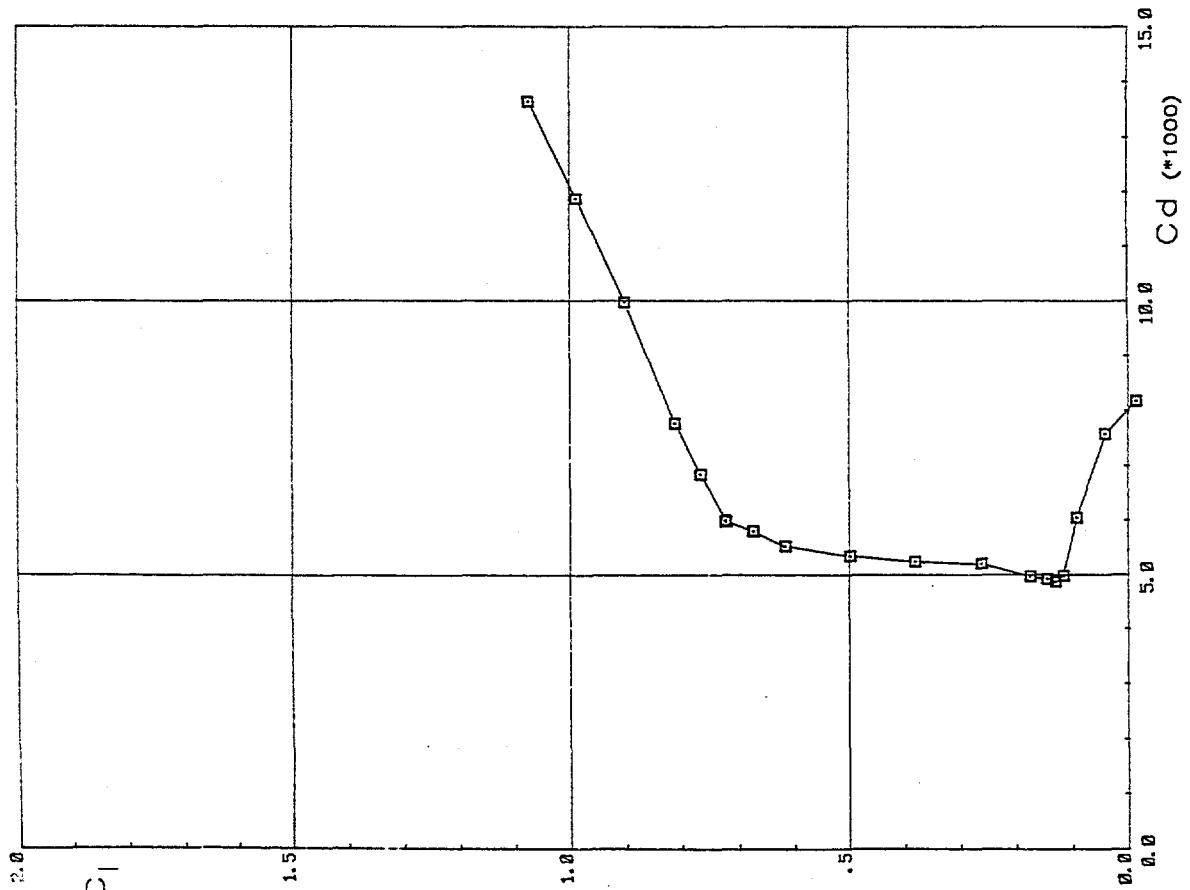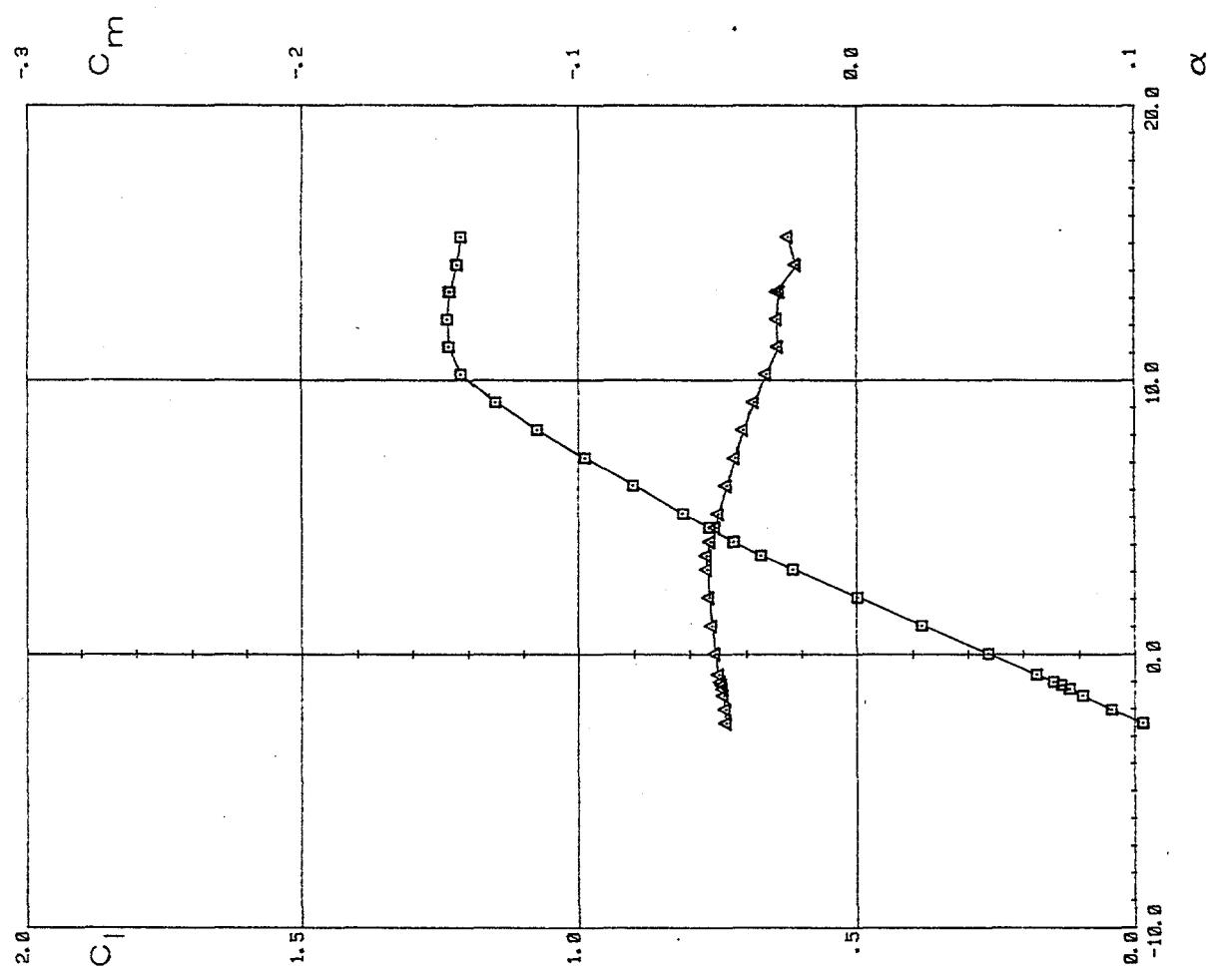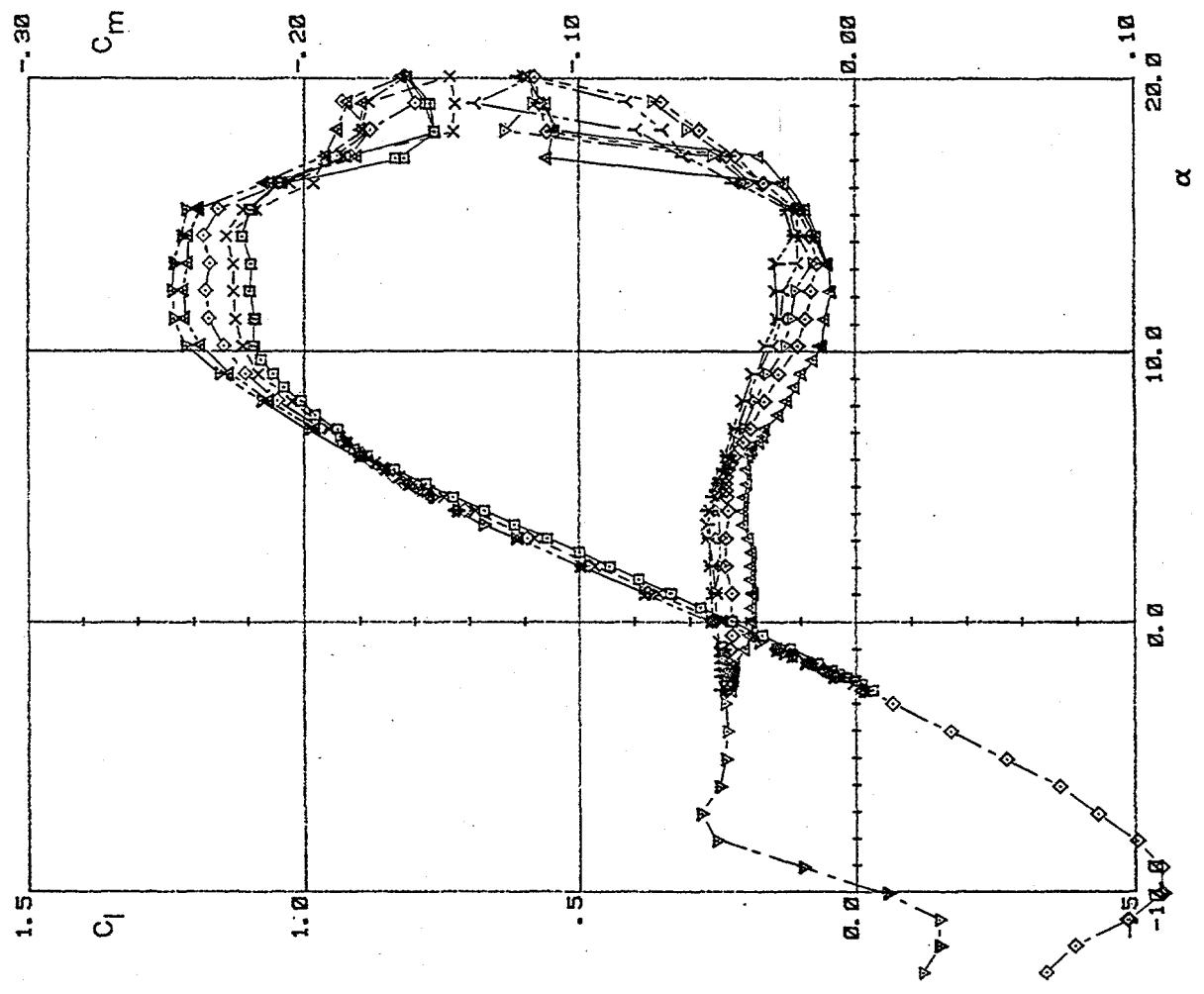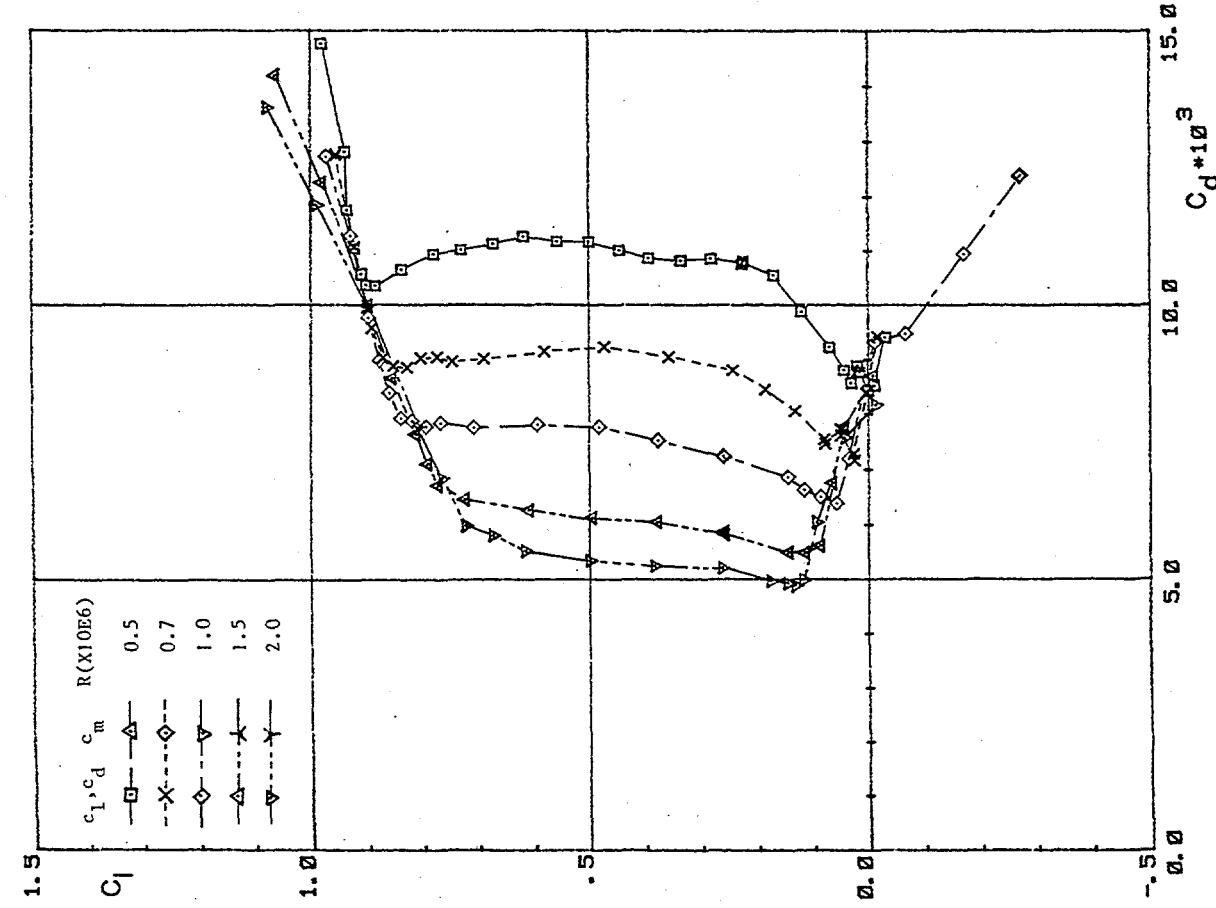
Figure 16.- Effects of Reynolds number on section characteristics.

LSL Delft University of Technology
Low Speed Laboratory

Transition
O   Free
□   Fixed
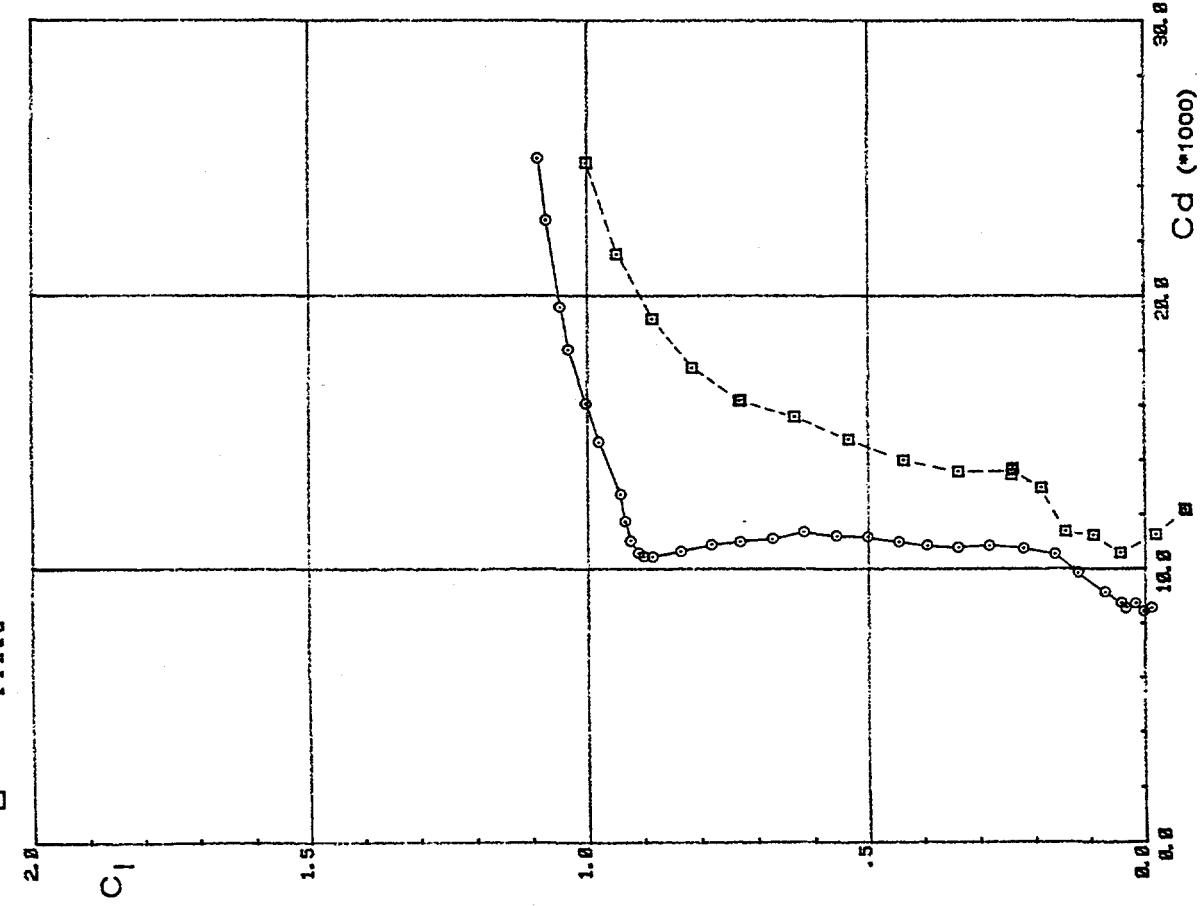
(a) R = 500,000.
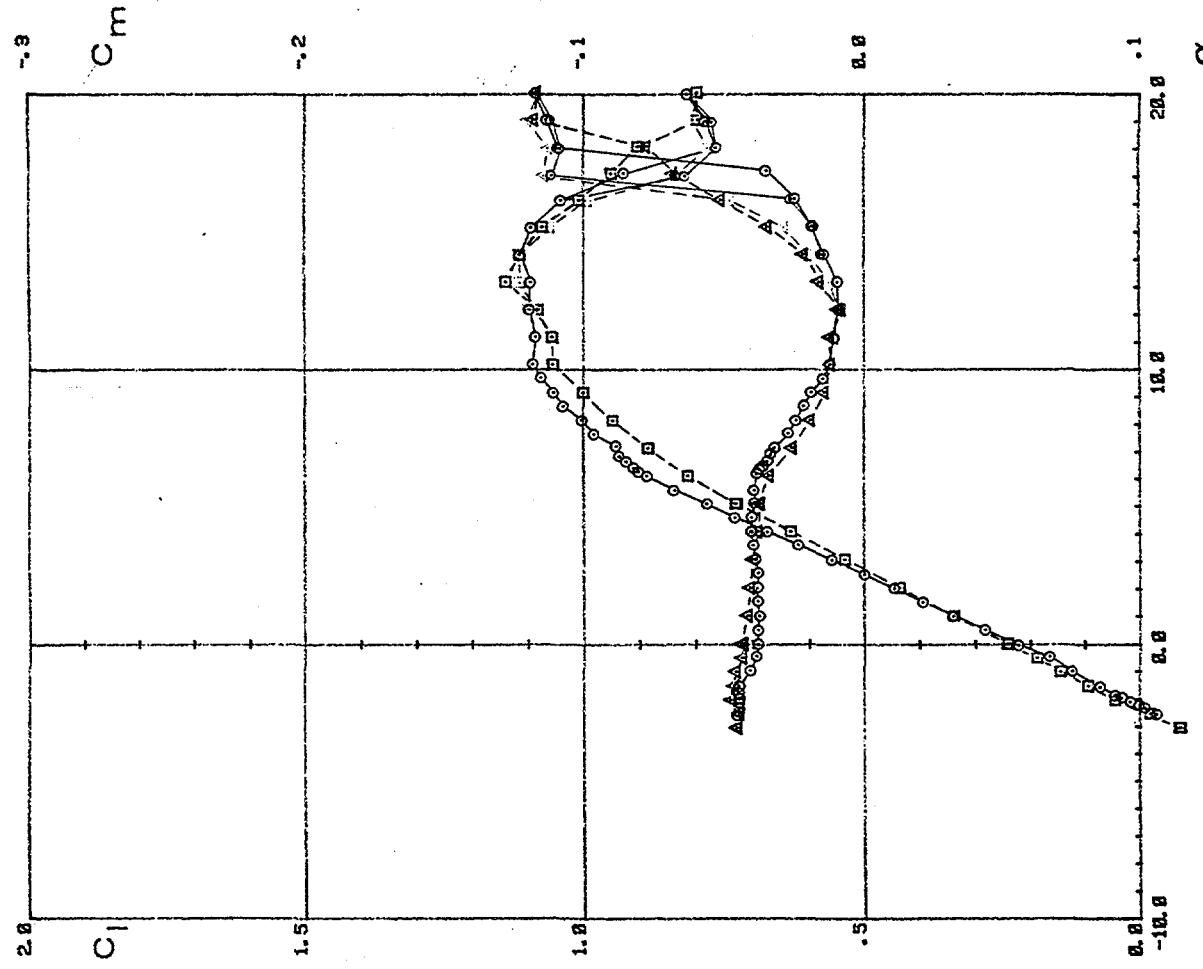
Figure 17.- Effect of roughness on section characteristics.

68
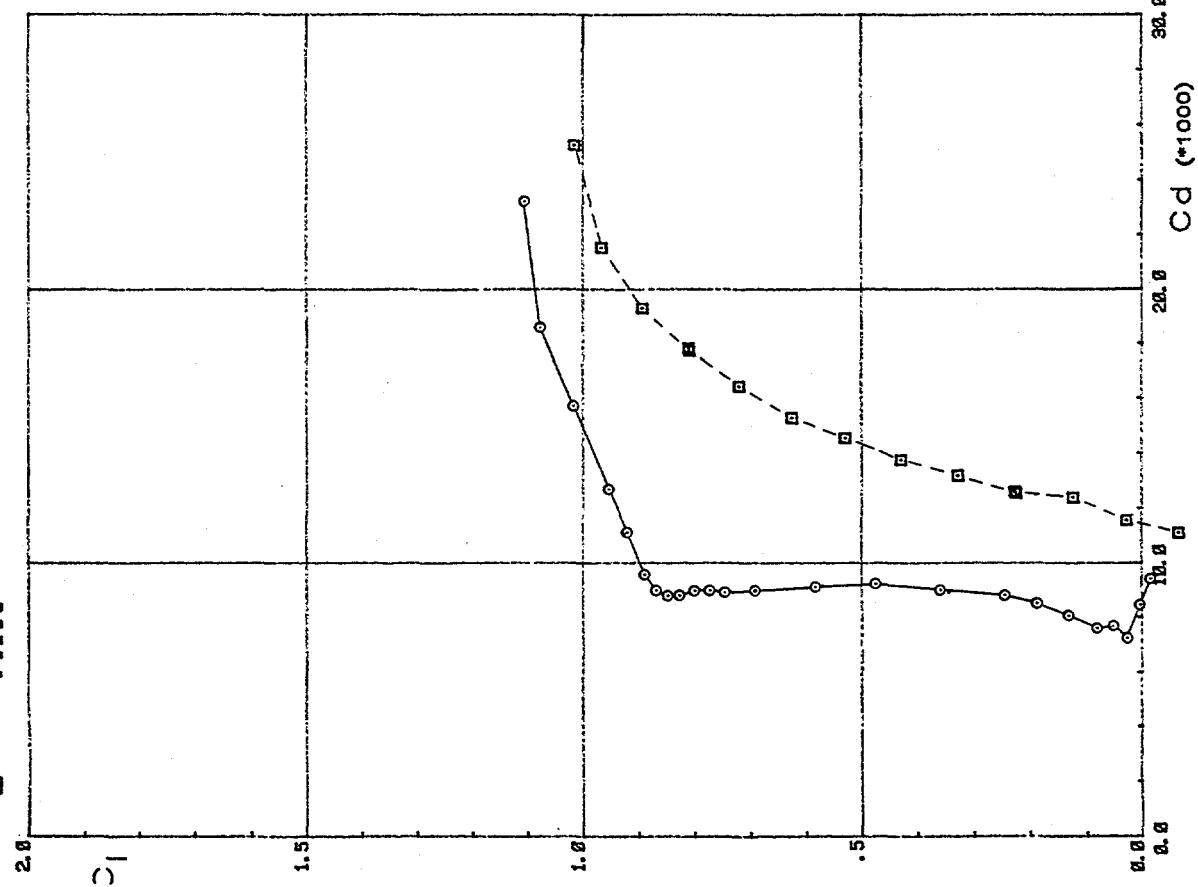
(b) R = 700,000.

Figure 17.- Continued.

69

Delft University of Technology
Low Speed Laboratory

Transition
O   Free
□   Fixed
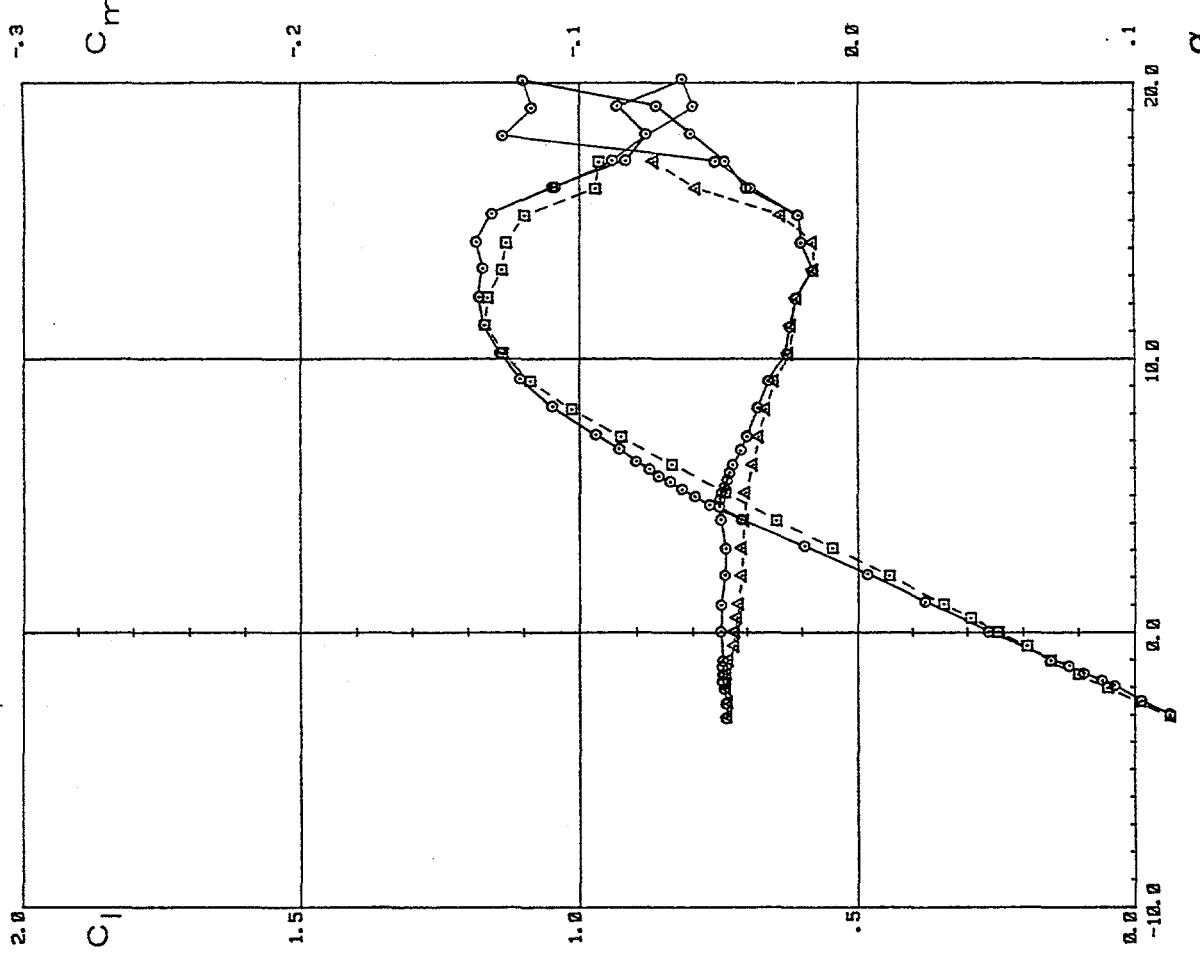
(c) R = 1,000,000.

Figure 17.- Continued.

70

Transition
○ Free
□ Fixed

(d) R = 1,500,000.

Figure 17.- Continued.

71

Delft University of Technology
Low Speed Laboratory
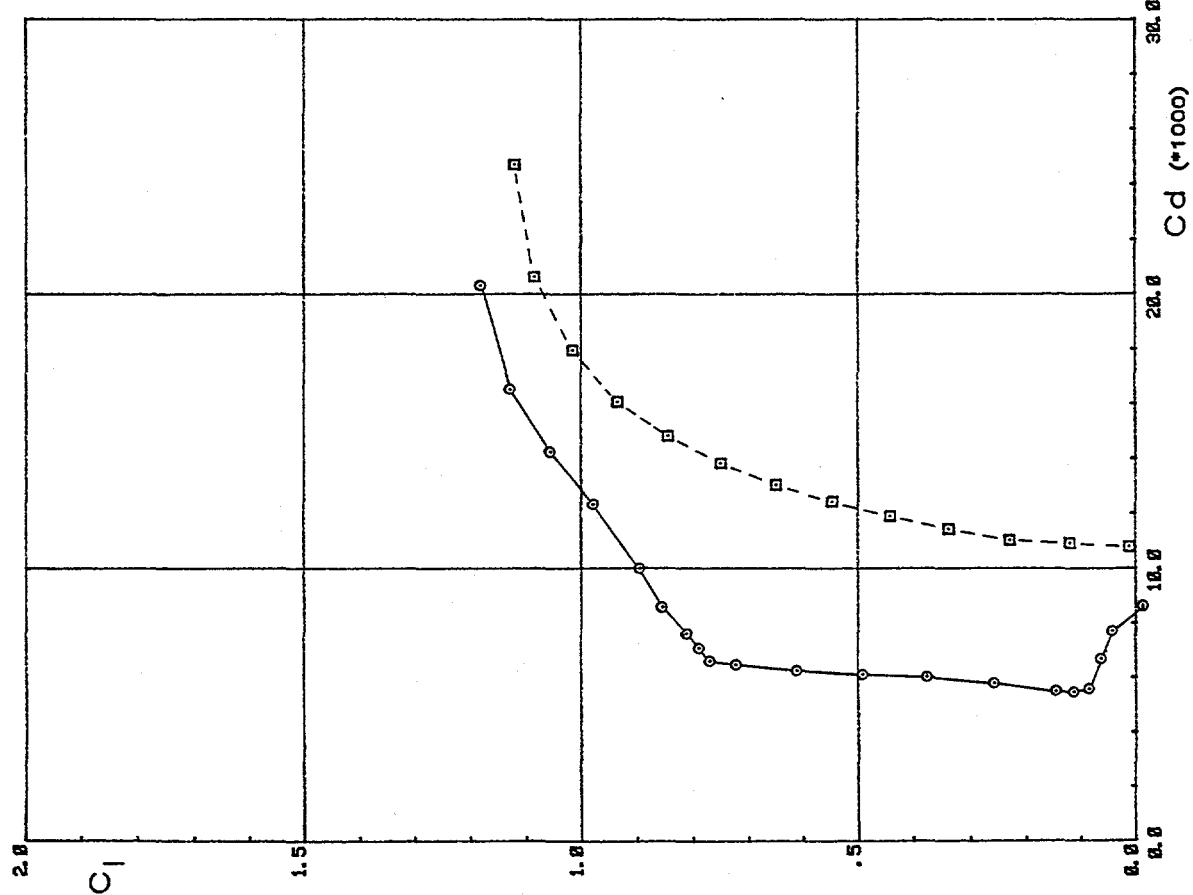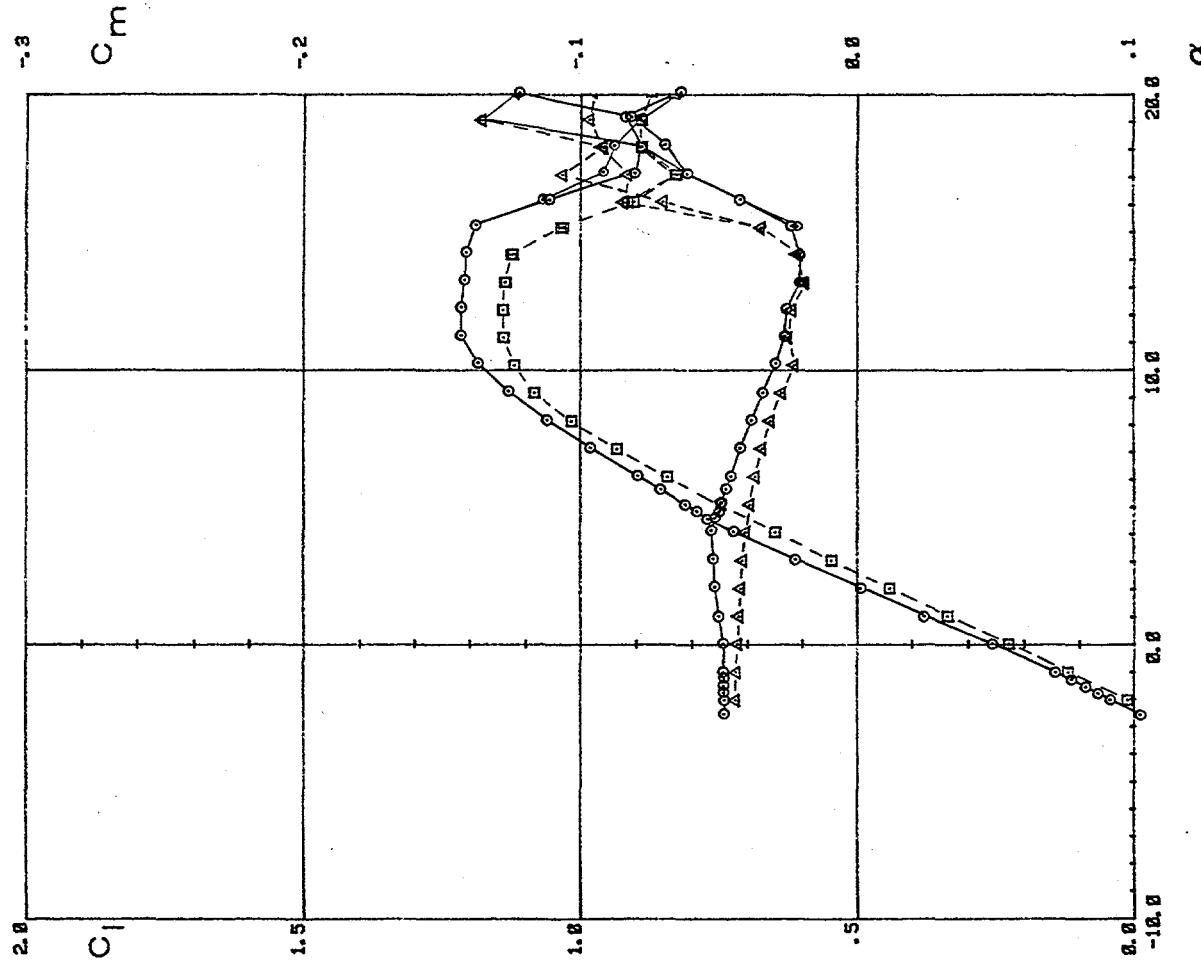
Transition
Free ○
Fixed □

(e) R = 2,000,000.

72

Figure 18.- Effect of turbulators on section characteristics for R = 1,000,000.

73

(a) $\alpha = 1.03$ degrees.
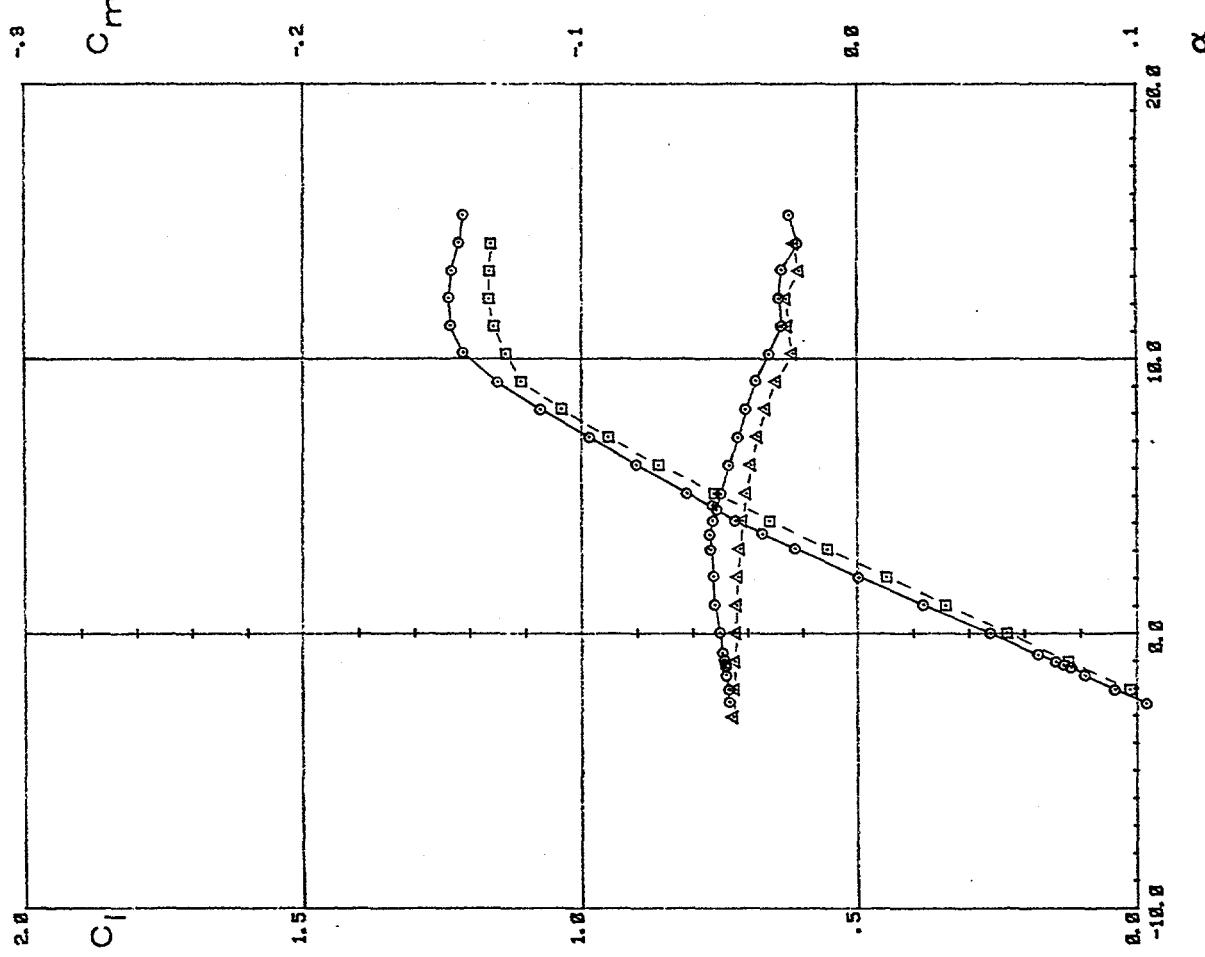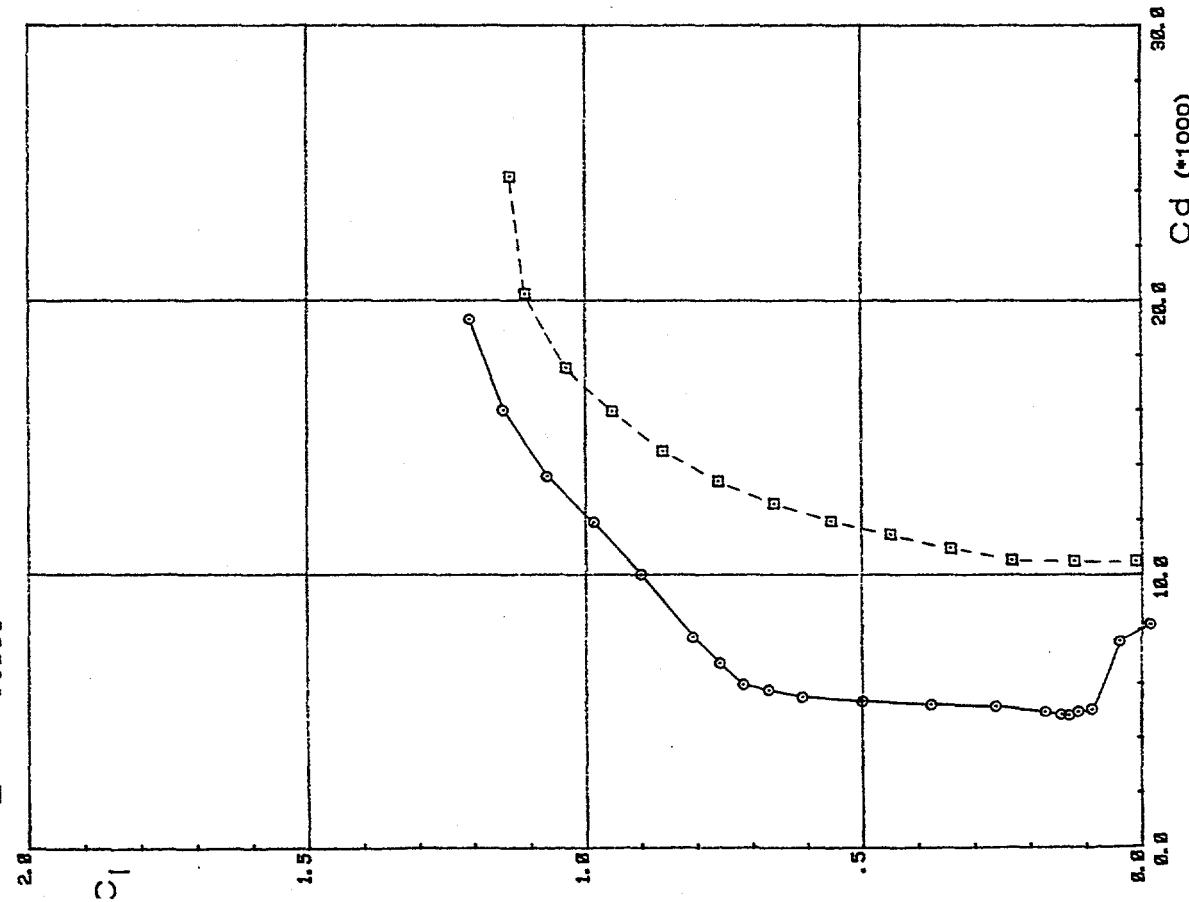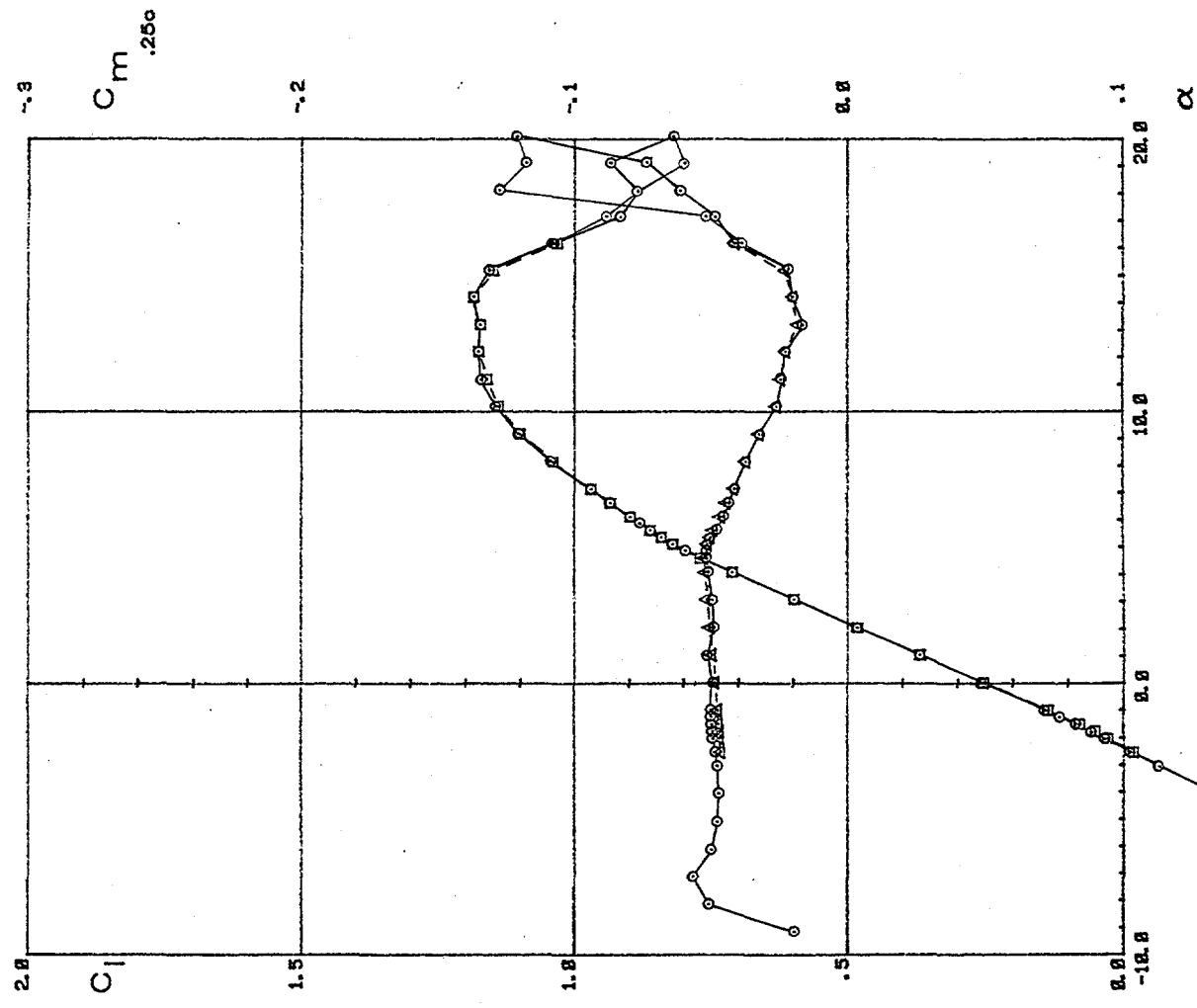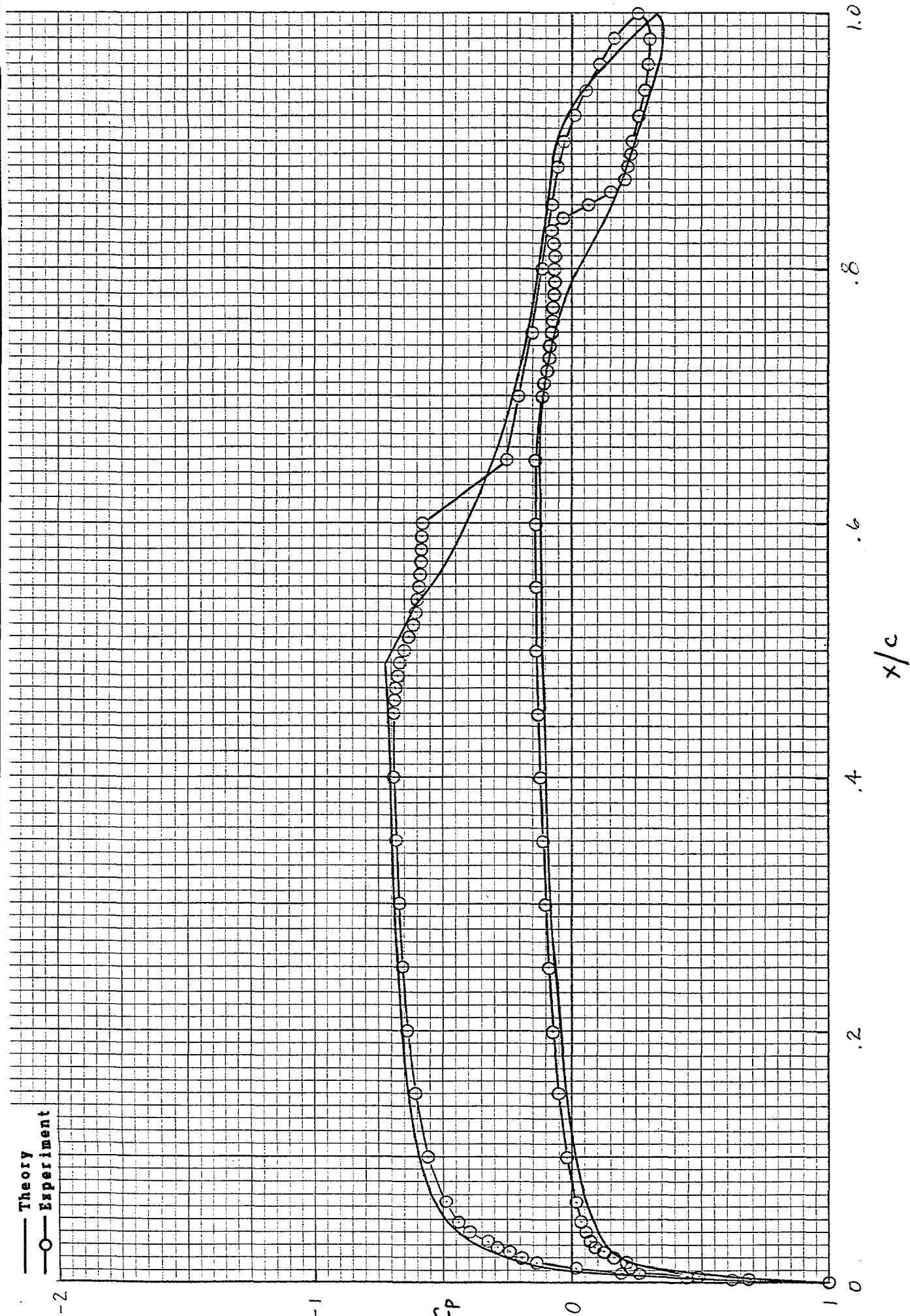
Figure 19.— Comparison of theoretical and experimental pressure distributions.

74

(b) α = 5.11 degrees.

Figure 19.- Continued.

75
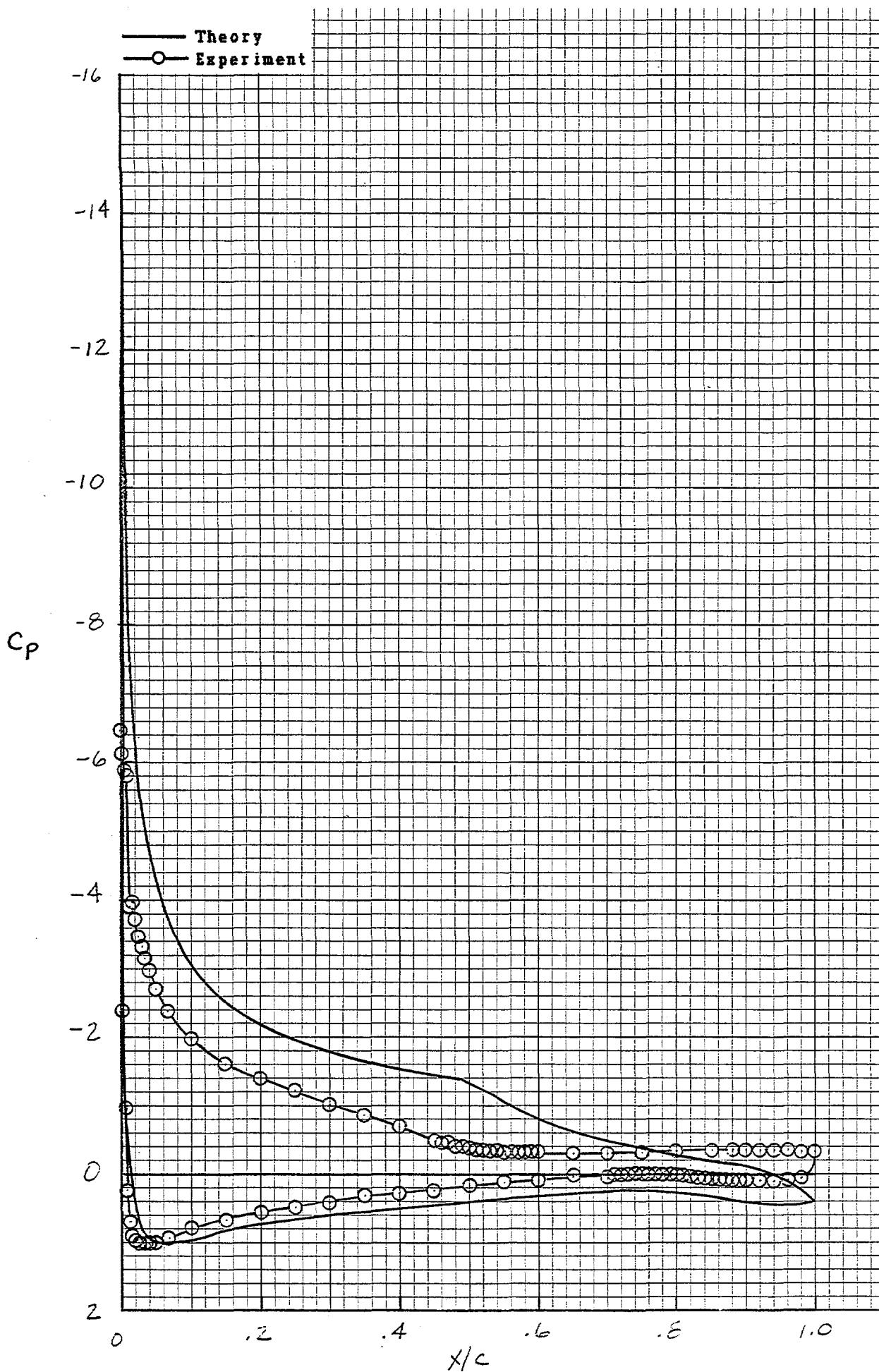
(c) α = 14.19 degrees.

Figure 19.- Concluded.

Delft University of Technology
Low Speed Laboratory

Laminar separation bubble
Upper surface
Lower surface

Theory
Experiment
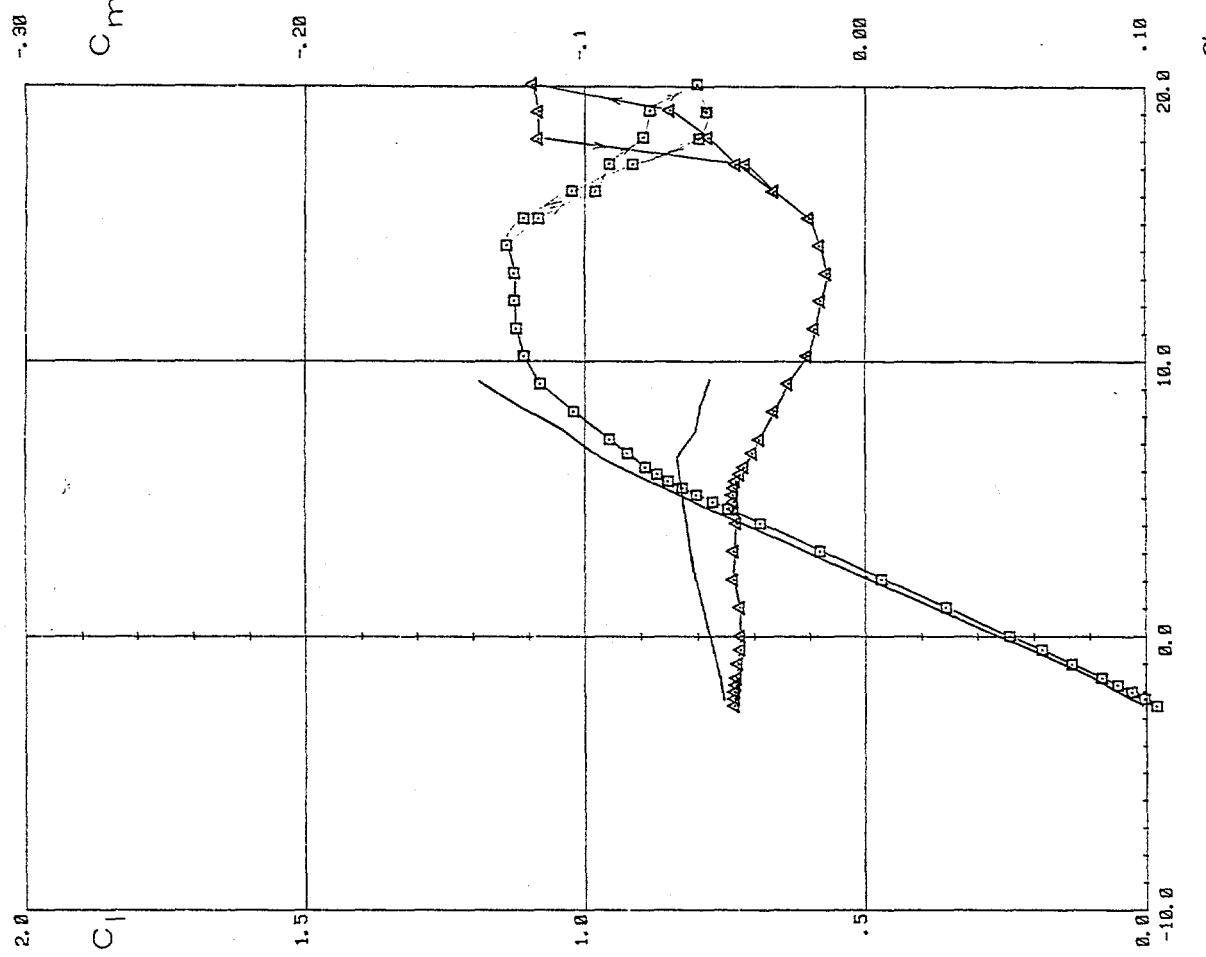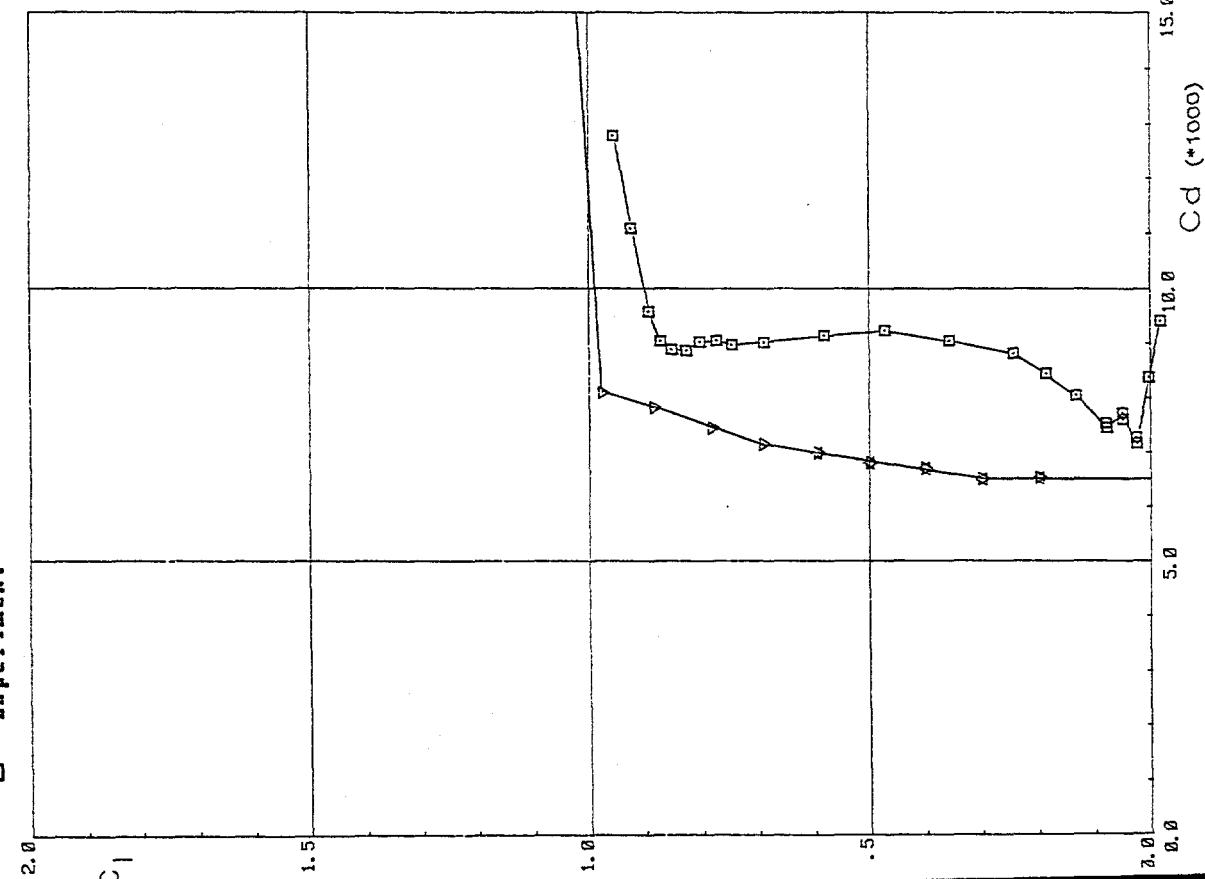
C_m
C_l
α
C_d (*1000)

(a) R = 500,000.

Figure 20.- Comparison of theoretical and experimental section characteristics with transition free.

77

(b) R = 700,000.

Figure 20.- Continued.

(c) R = 1,000,000.

Figure 20.- Continued.

79

(d) R = 1,500,000.

80

Delft University of Technology
Low Speed Laboratory

Theory
Experiment

C_m

C_l

α

C_d (*1000)

(e) R = 2,000,000.

Figure 20.- Concluded.

81

— Theory
—□— Experiment

(a) R = 500,000.

82

Delft University of Technology
Low Speed Laboratory
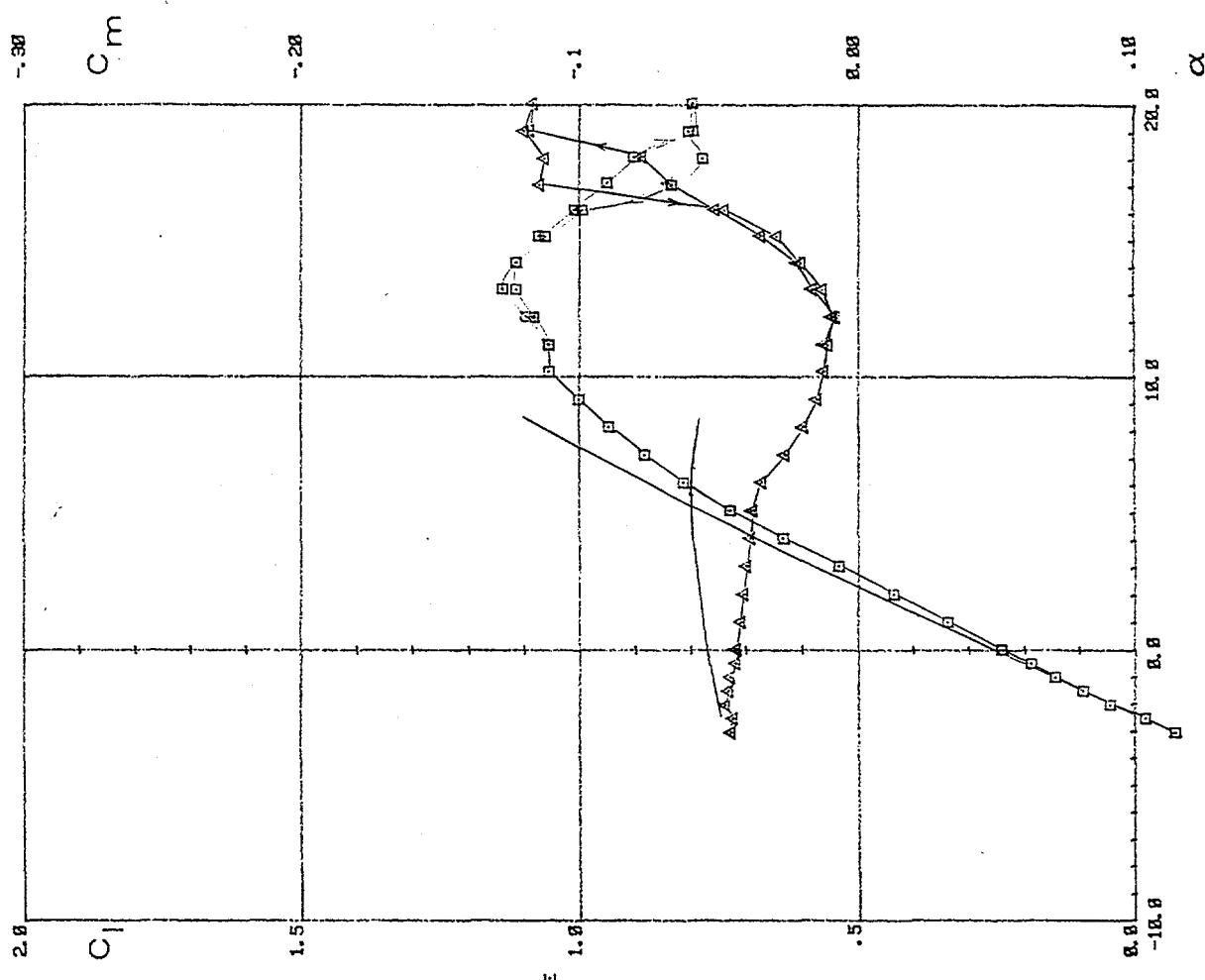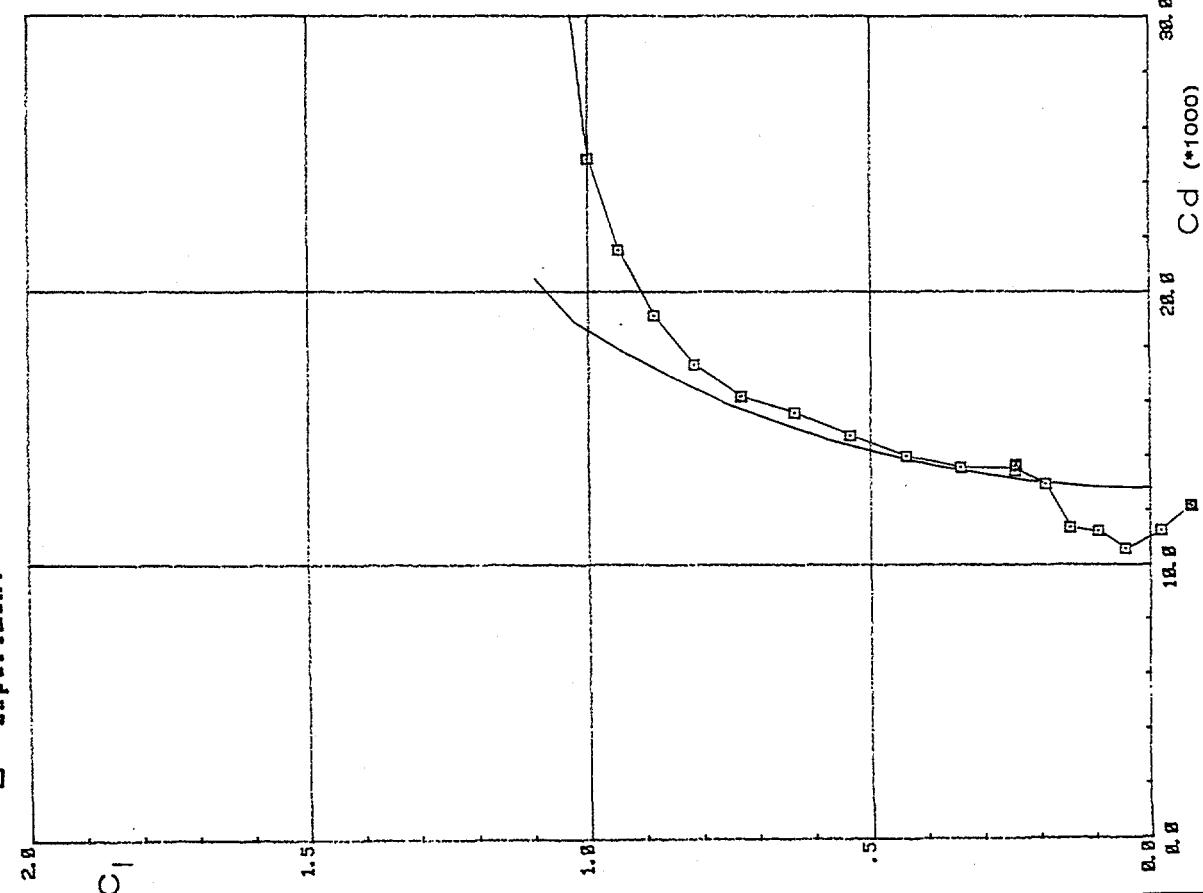
Theory
Experiment

(b) R = 700,000.
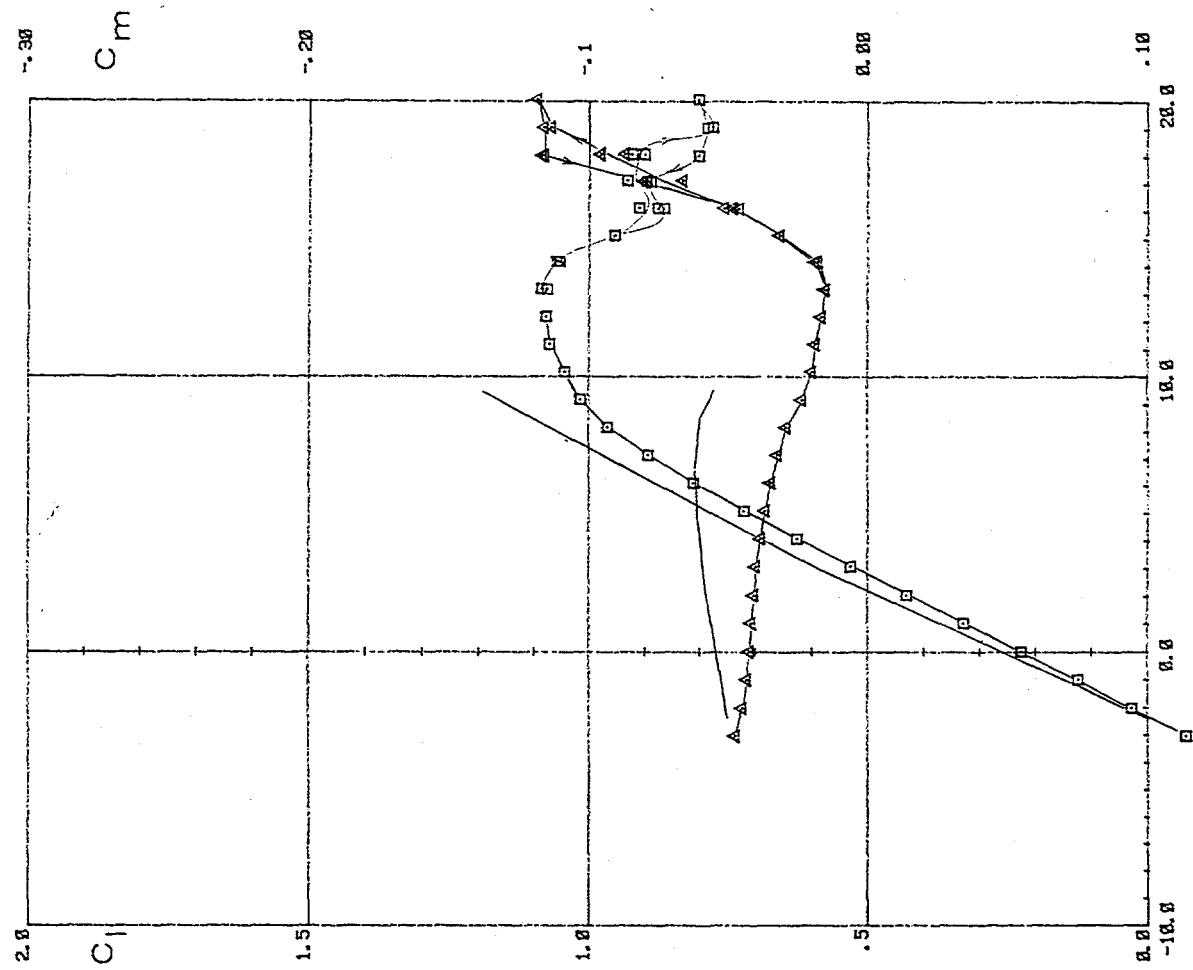
Figure 21.- Continued.

83

Delft University of Technology
Low Speed Laboratory

Theory
Experiment

(c) R = 1,000,000.

84

(d) R = 1,500,000.

Figure 21.- Continued.

85

Delft University of Technology
Low Speed Laboratory

Theory
Experiment

(e) R = 2,000,000.

86
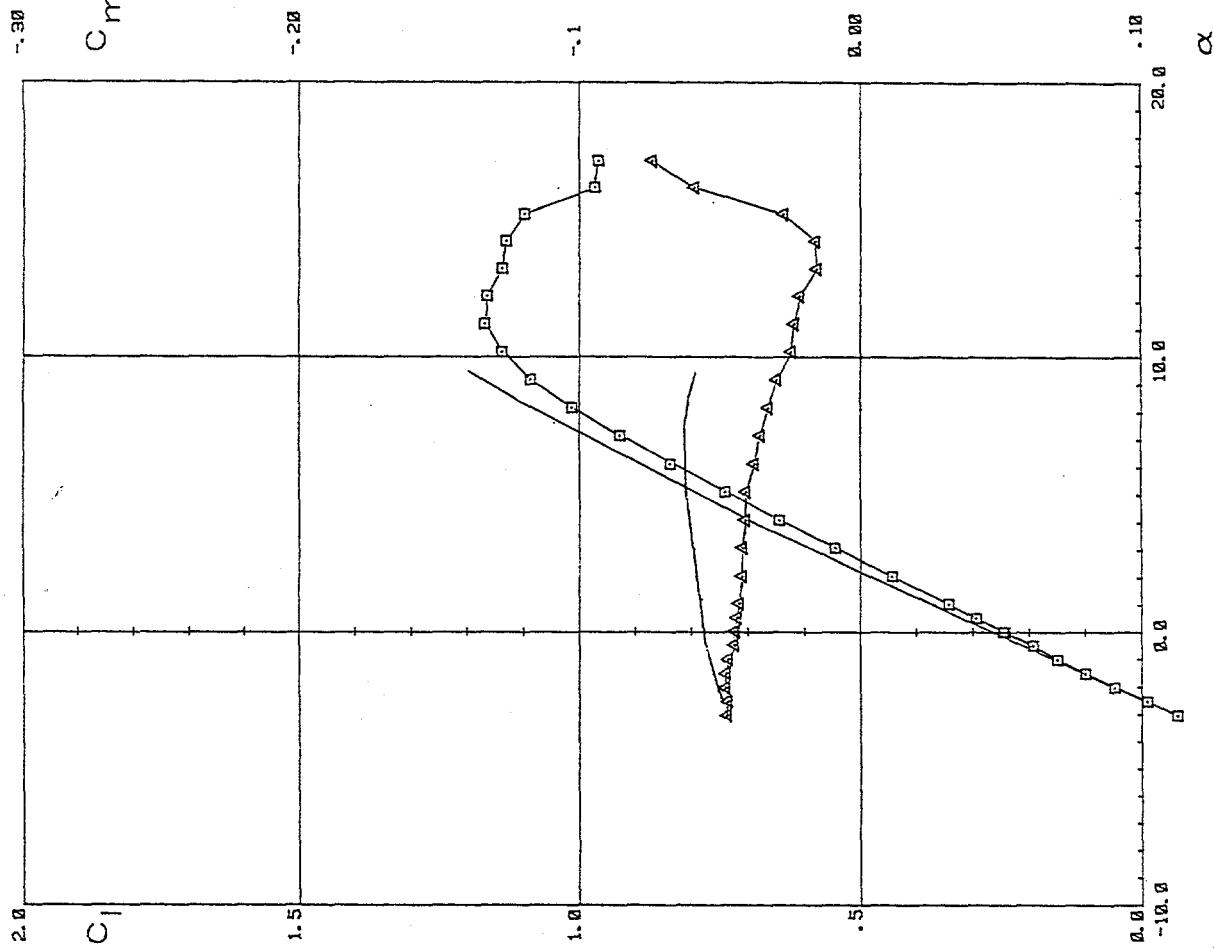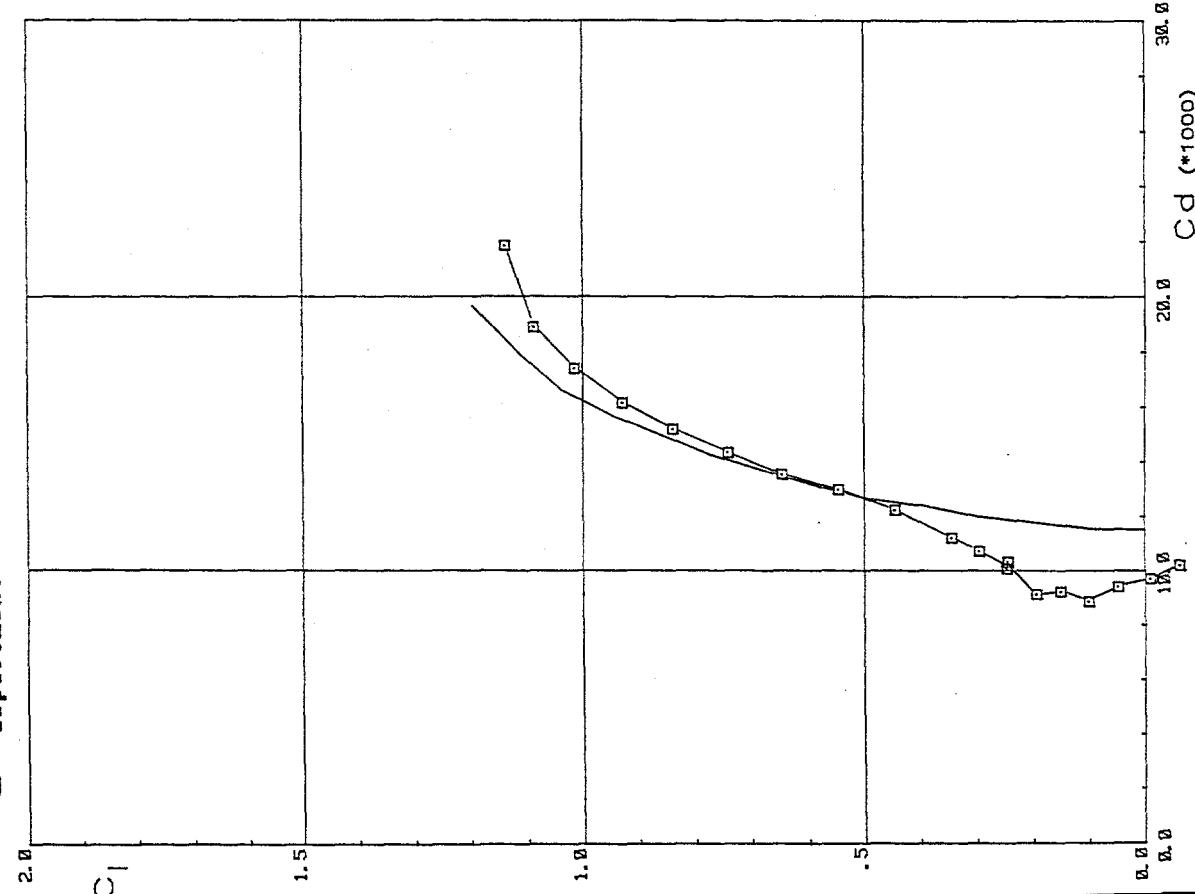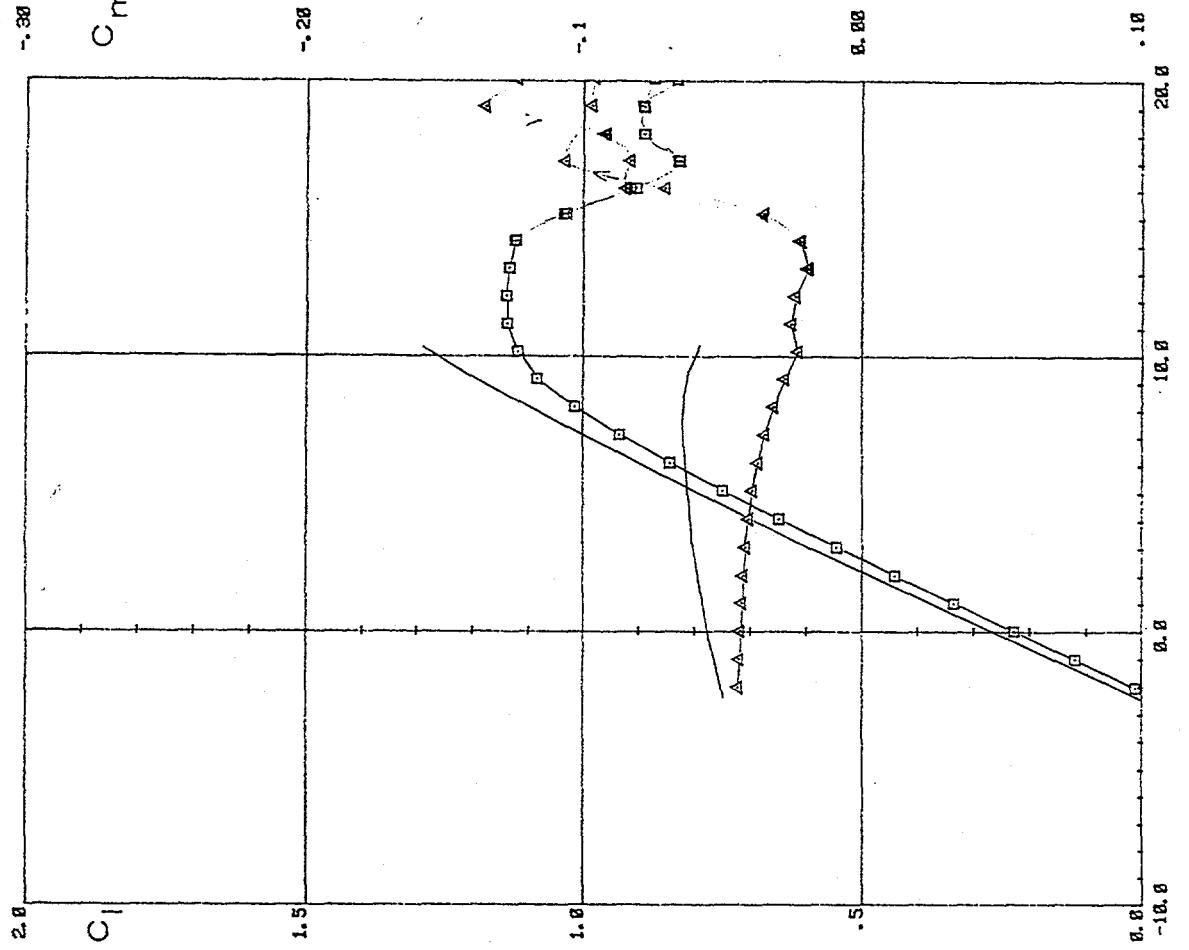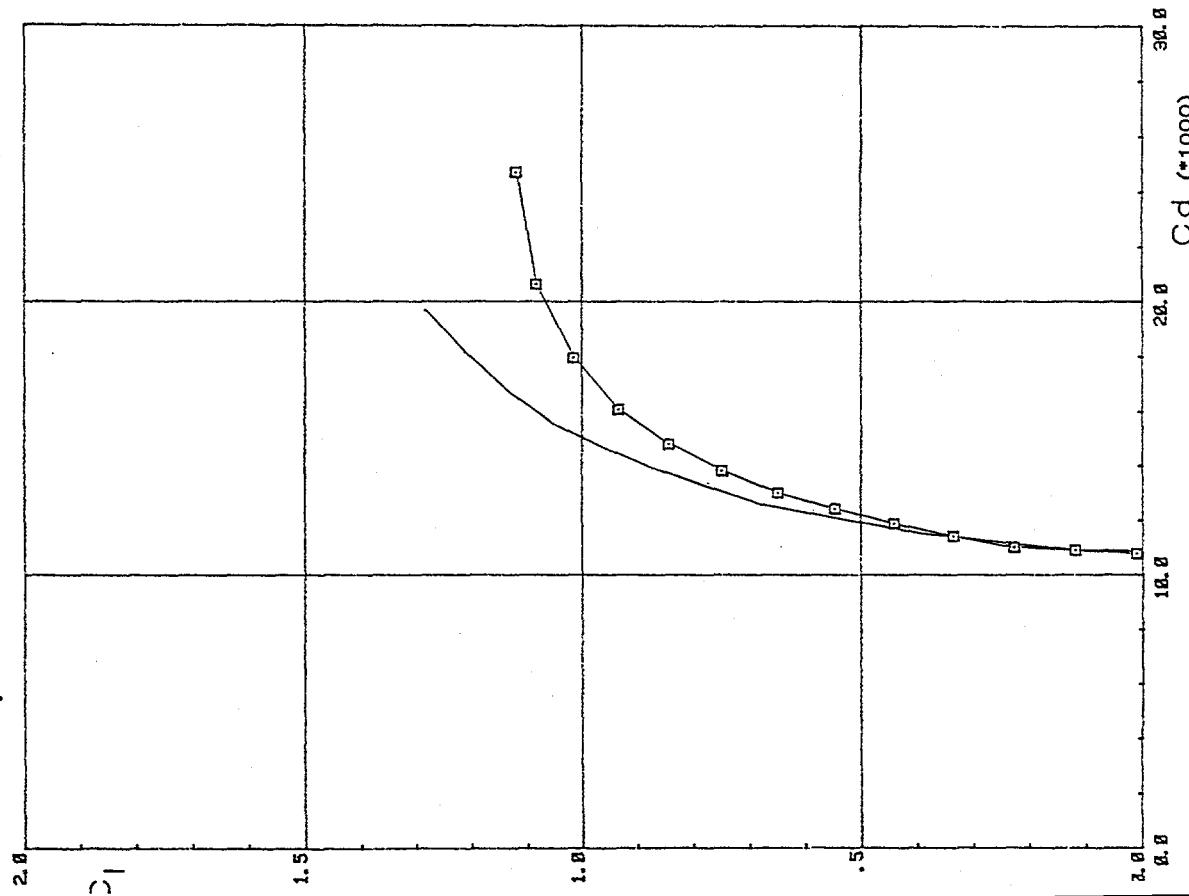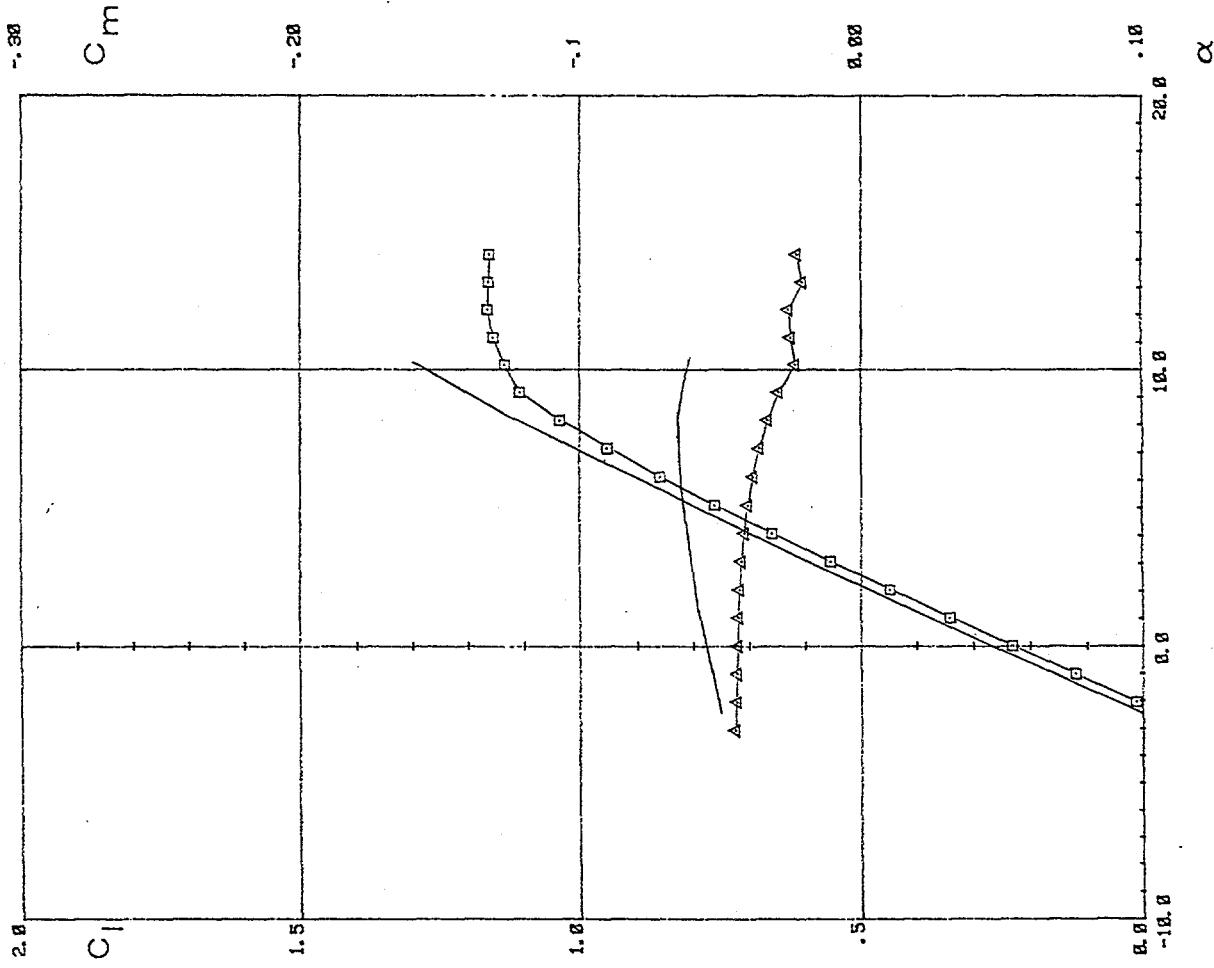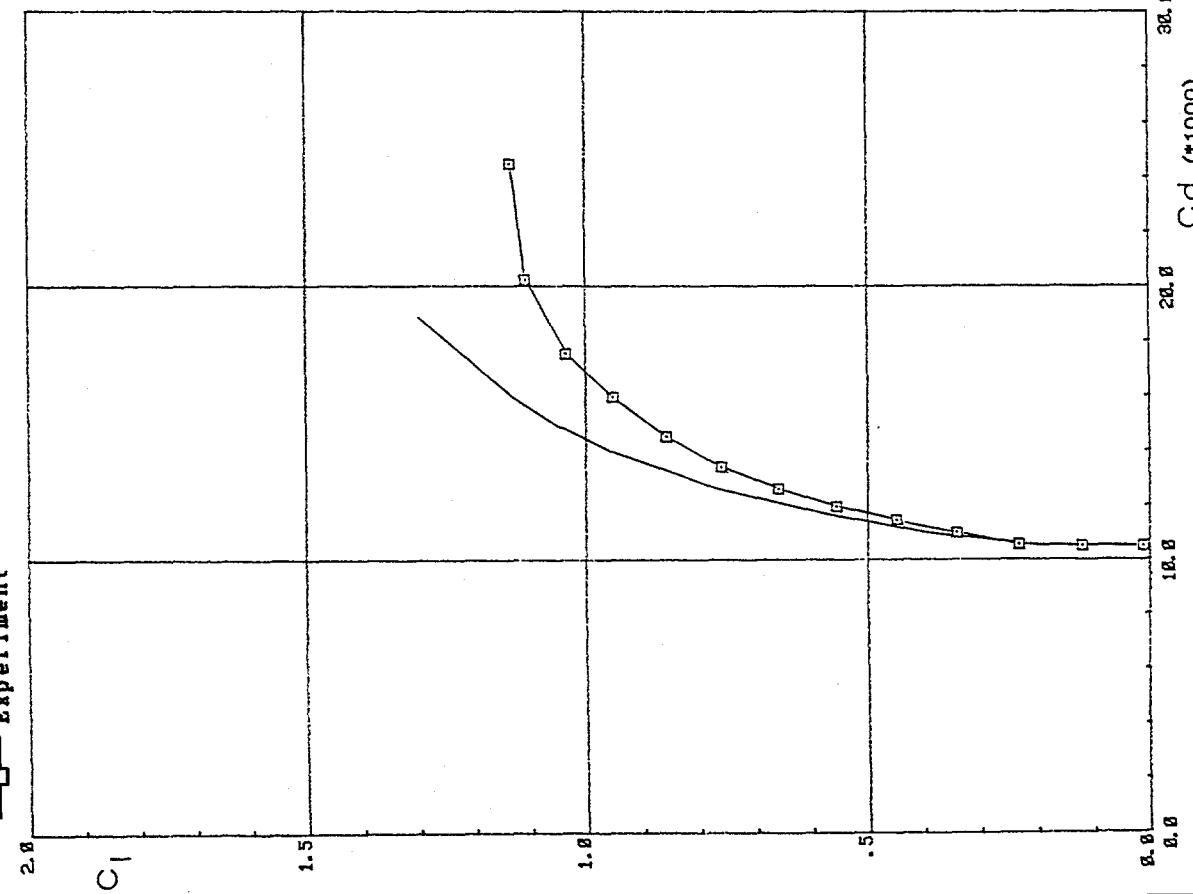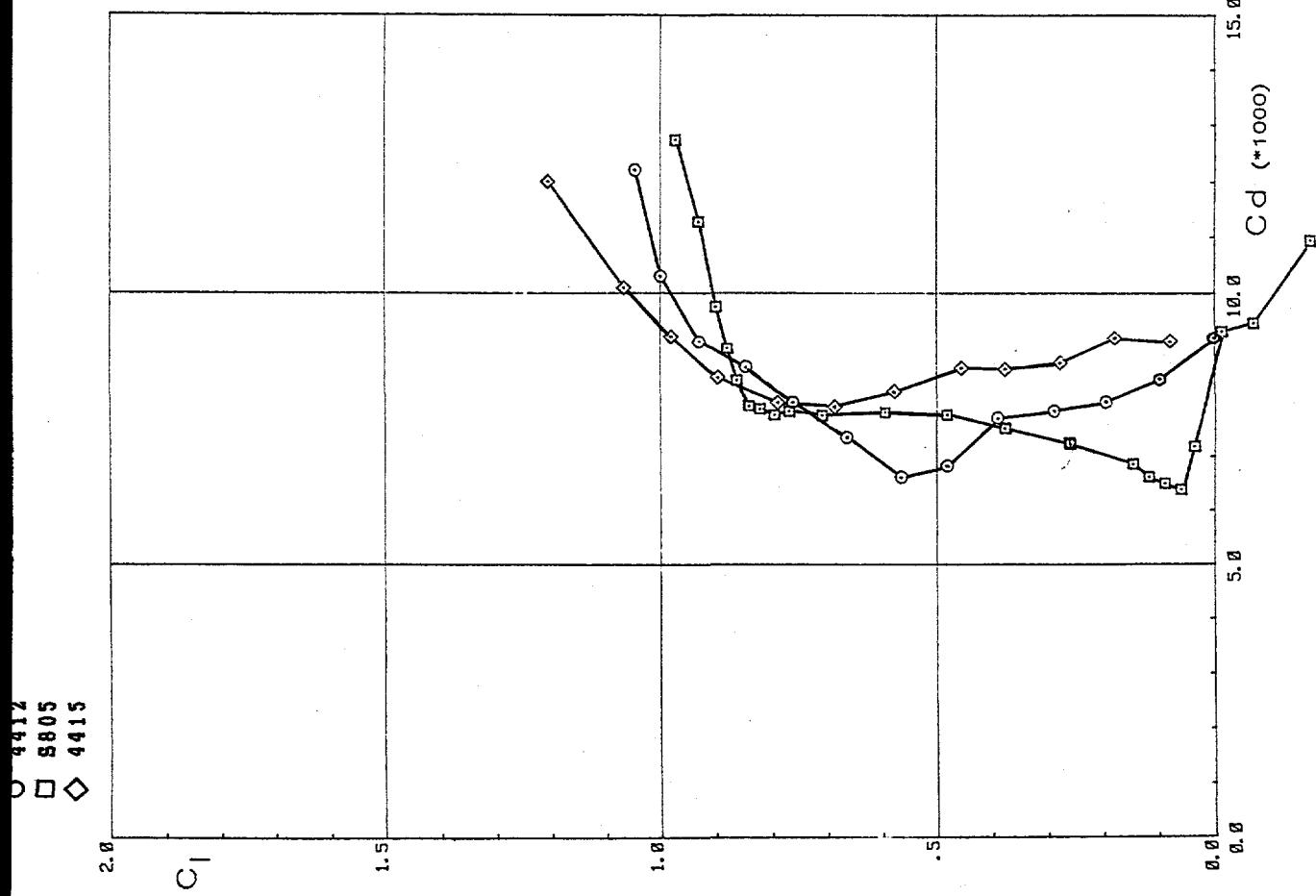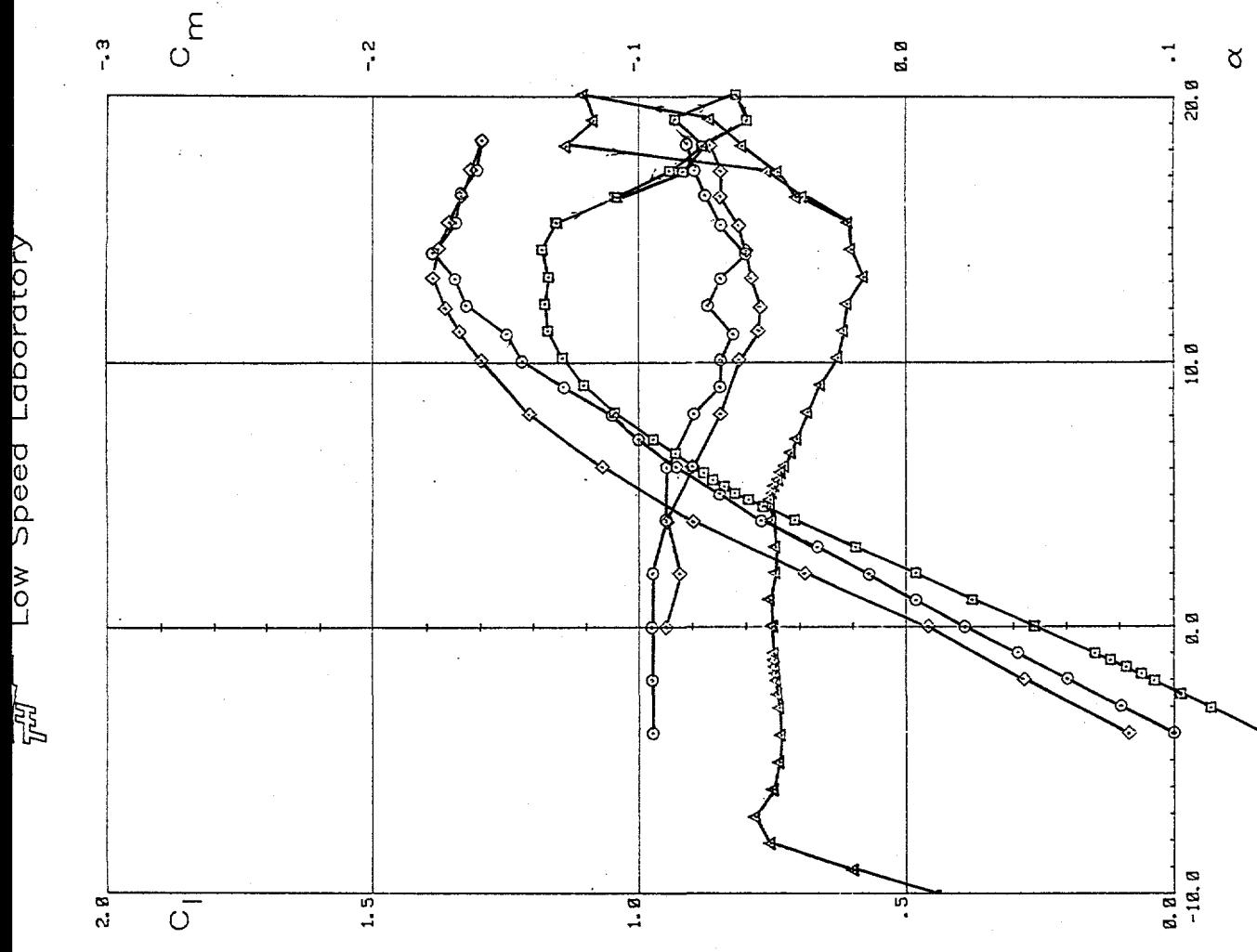
Figure 22.- Comparison of section characteristics of S805 and NACA 4412 and 4415 airfoils for R = 1,000,000.

87
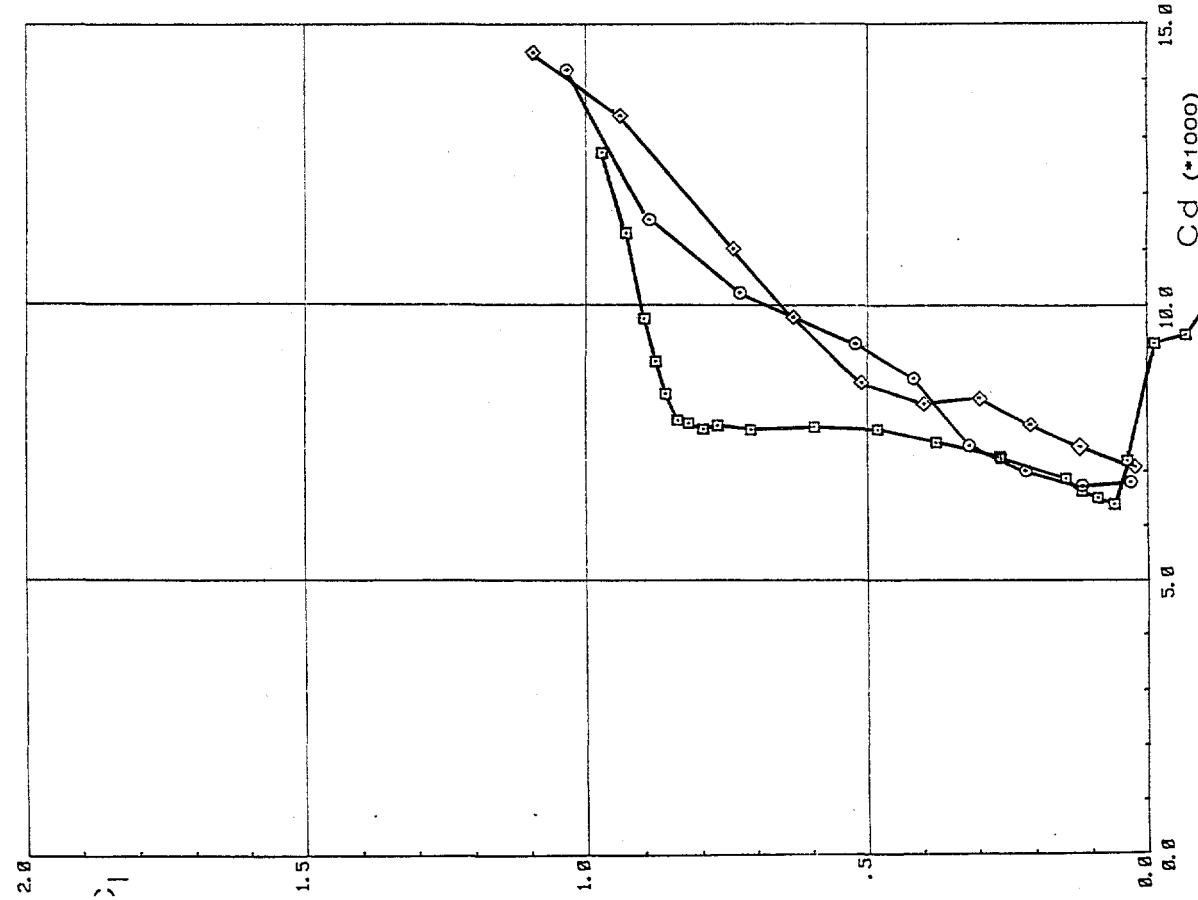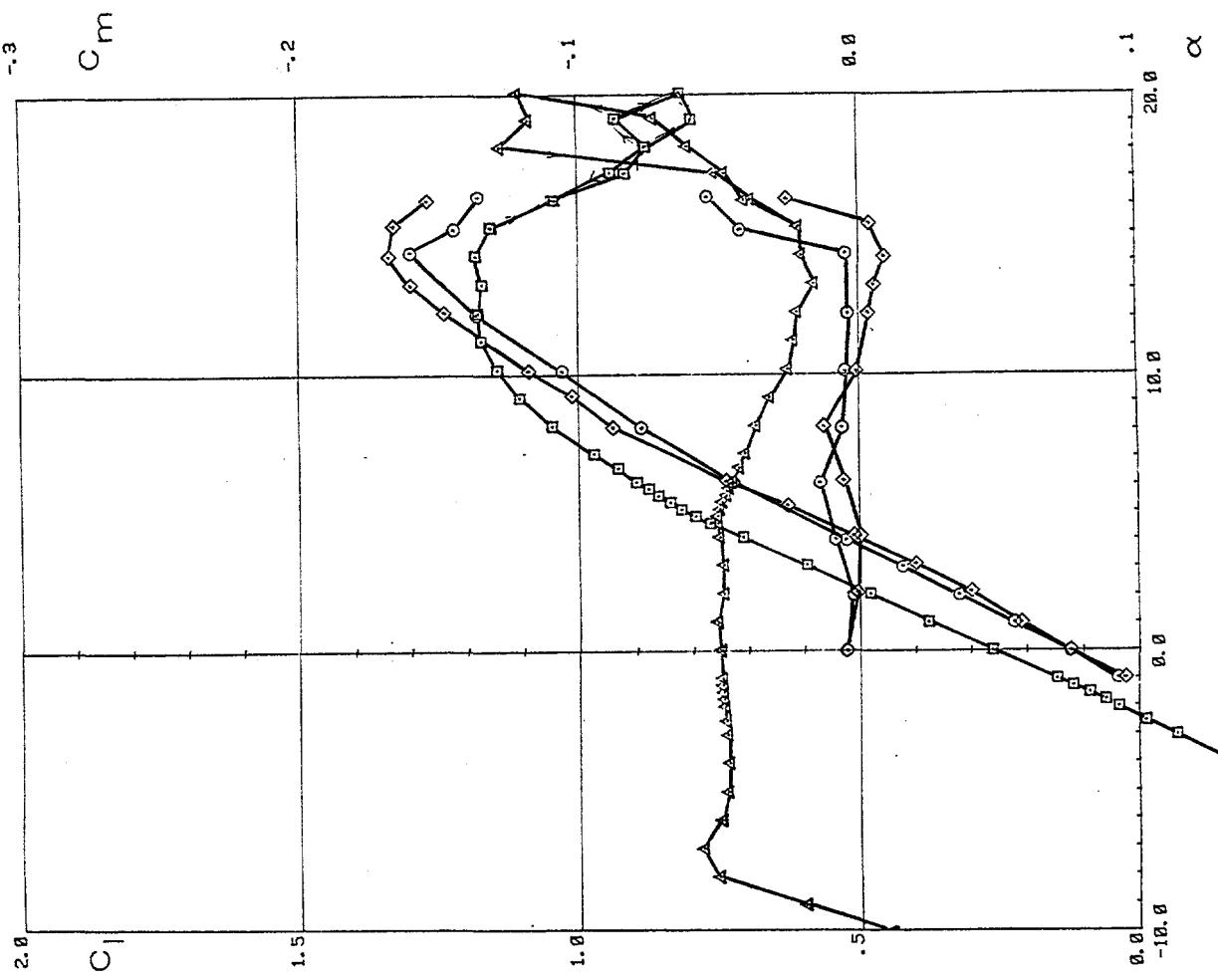
Figure 23. - Comparison of section characteristics of S805 and NACA 23012 and NACA 23015

Delft University of Technology
Low Speed Laboratory

○ 23012
□ S805
◇ 23015

88
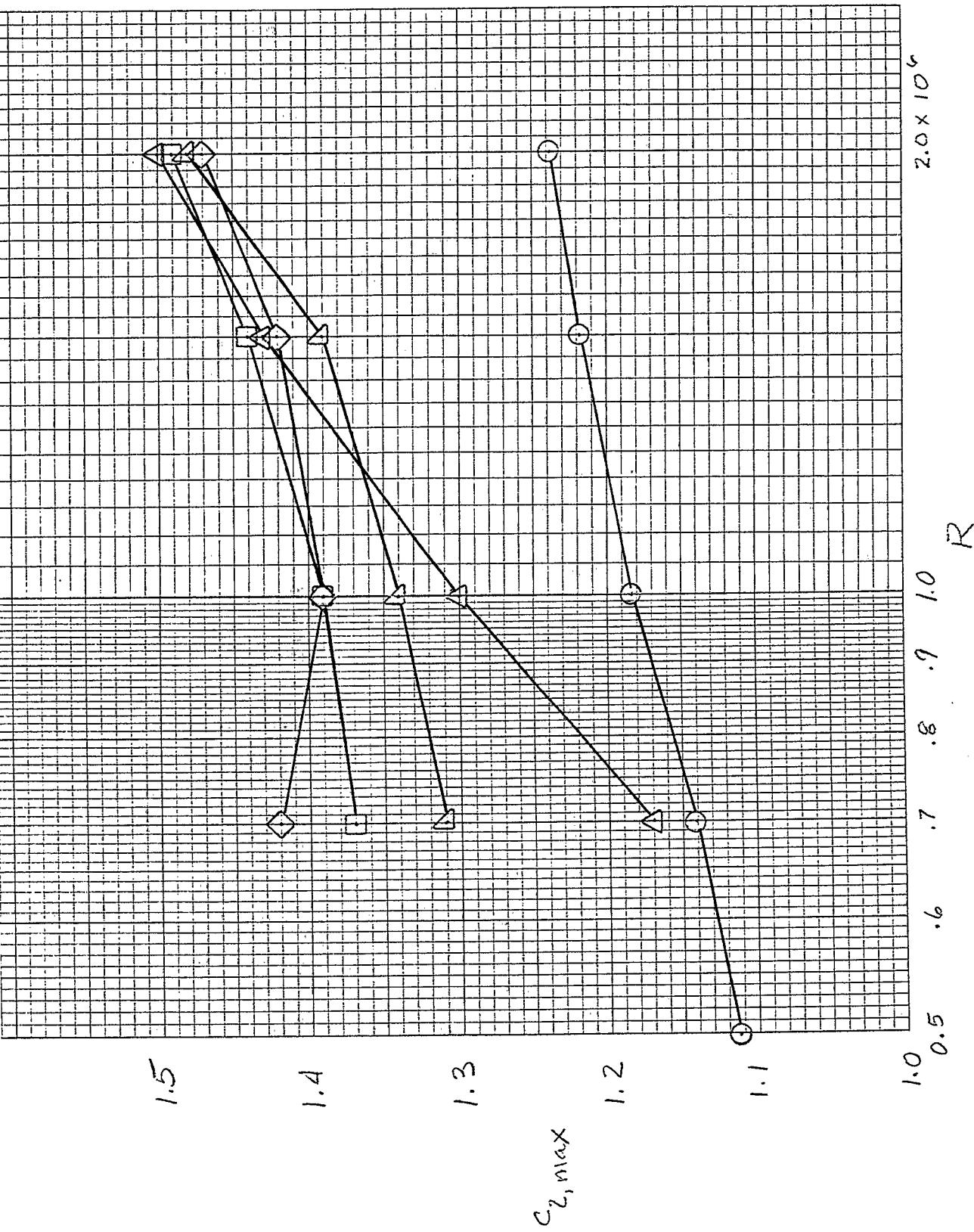
Figure 24.- Comparison of maximum lift coefficients of S805 and NACA 4412, 4415, 23012, and 23015 airfoils.

89
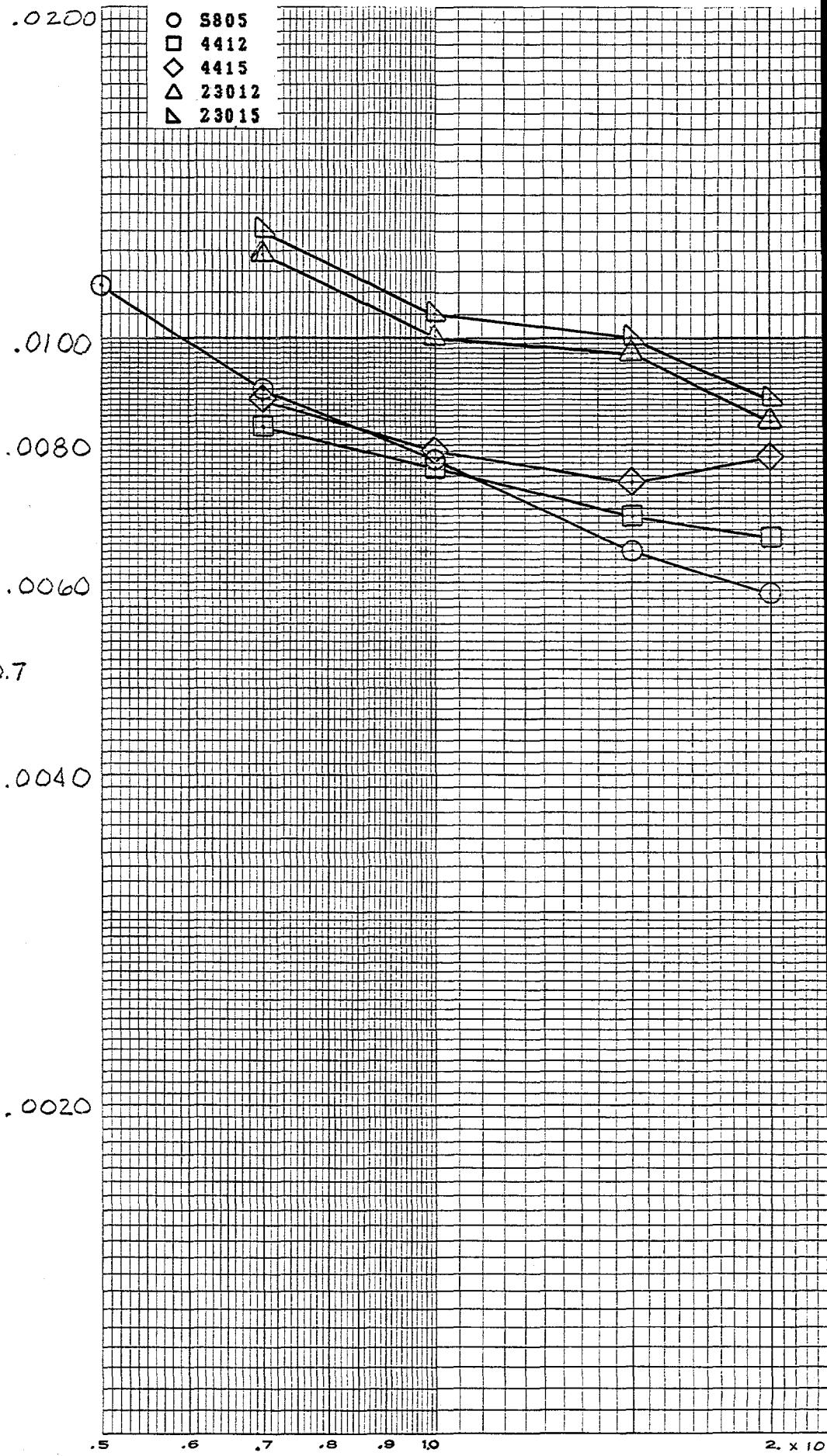
Figure 25.– Comparison of drag coefficients at lift coefficient of 0.7 of S8
and NACA 4412, 4415, 23012, and 23015 airfoils.

REPORT DOCUMENTATION PAGE

1.	2. REPORT DATE January 1997	3. REPORT TYPE AND DATES COVERED Subcontract Report

4. TITLE AND SUBTITLE

Design and Experimental Results for the S805 Airfoil

5. FUNDING NUMBERS

C: HK-4-04148-01

TA: WE711110

6. AUTHOR(S)

Dan M. Somers

7. PERFORMING ORGANIZATION NAME(S) AND ADDRESS(ES)

Airfoils, Incorporated
State College, Pennsylvania

8. PERFORMING ORGANIZATION REPORT NUMBER

9. SPONSORING/MONITORING AGENCY NAME(S) AND ADDRESS(ES)

National Renewable Energy Laboratory
1617 Cole Blvd.
Golden, CO 80401-3393

10. SPONSORING/MONITORING AGENCY REPORT NUMBER

SR-440-6917

DE97000105

11. SUPPLEMENTARY NOTES

NREL Technical Monitor: James Tangler

12a. DISTRIBUTION/AVAILABILITY STATEMENT
National Technical Information Service
U.S. Department of Commerce
5285 Port Royal Road
Springfield, VA 22161

12b. DISTRIBUTION CODE

UC-1213

13. ABSTRACT *(Maximum 200 words)*

An airfoil for horizontal-axis wind-turbine applications, the S805, has been designed and analyzed theoretically and verified experimentally in the low-turbulence wind tunnel of the Delft University of Technology Low Speed Laboratory, The Netherlands. The two primary objectives of restrained maximum lift, insensitive to roughness, and low profile drag have been achieved. The airfoil also exhibits a docile stall. Comparisons of the theoretical and experimental results show good agreement. Comparisons with other airfoils illustrate the restrained maximum lift coefficient as well as the lower profile-drag coefficients, thus confirming the achievement of the primary objectives.

14. SUBJECT TERMS

horizontal-axis wind-turbine airfoil

15. NUMBER OF PAGES

16. PRICE CODE

17. SECURITY CLASSIFICATION OF REPORT Unclassified	18. SECURITY CLASSIFICATION OF THIS PAGE Unclassified	19. SECURITY CLASSIFICATION OF ABSTRACT Unclassified	20. LIMITATION OF ABSTRACT UL